

UNIVERSITY OF CENTRAL OKLAHOMA

Electrokinetically Forced Turbulence in Microfluidic Flow

A Thesis

By

Willy Duffle

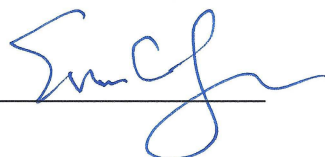
Department of Engineering and Physics

Submitted in partial fulfillment of the requirements
for the degree of

Master of Science, Engineering Physics - Mechanical Engineering

4-May-17

The undersigned have examined the thesis entitled '**Electrokinetically Forced Turbulence in Microfluidic Flow**' presented by **Willy Duffle**, a candidate for the degree of **Master of Science, Engineering Physics - Mechanical Engineering** and hereby certify that it is worthy of acceptance.

5/4/17 
Date

Dr. Evan Lemley

Advisors name

5/4/2017 
Date

Dr. Ronald Miller

committee member name

5/4/2017 
Date

Dr. Alaeddin Abu-Abed

committee member name

ABSTRACT

While laminar flow heat transfer and mixing in microfluidic geometries has been investigated experimentally, as has the effect of geometry-induced turbulence in microfluidic flow (it is well documented that turbulence increases convective heat transfer in *macrofluidic* flow), little literature exists investigating the effect of electrokinetically-induced turbulence on heat transfer at the micro scale. Successful research in this area could be invaluable in creating more efficient heat exchangers for emerging microscale electronics as well as to fields requiring greater control of mixing in microfluidic devices.

Using recently observed experimental data, this thesis employs computational fluid dynamics coupled with electromagnetic simulations to determine if electrokinetically-forced, low-Reynolds number turbulence can be observed in a micromixer modeled with a rectangular microchannel using Newtonian fluids. Analysis of the results was done by comparison to the experimental criteria defined for turbulent flow.

This thesis shows that, although the simulation setup is simplified, computational fluid dynamics (CFD) software can produce results comparable to experimental observations of low-Reynolds turbulence in microchannels using Newtonian fluids. In addition to comparing simulated velocities and turbulent energies to experimental data this thesis also presents initial data on the effects of electrokinetic forcing on microfluidic flow based on entropy generation rates.

ACKNOWLEDGMENTS

I would like to first thank my wife and family for all the time with them I sacrificed in pursuit of this thesis. I would also like to thank my thesis committee members Dr. Ronald Miller and Dr. Alaeddin Abu-Abed for their support and my thesis advisor Dr. Evan Lemley for his guidance and for sharing his wealth of knowledge in fluids research, both recently and through the years. I appreciate the support from the University of Central Oklahoma's Department of Engineering & Physics and for the use of the Buddy Supercomputer Cluster.

This work was partially sponsored by the National Science Foundation grant ACI-1429702 (funding for the Buddy Supercomputer Cluster), which served as the platform for much of the analyses conducted for this thesis and without which this thesis would not have been possible.

A special thank you goes to Dr. Guiren Wang of the Department of Mechanical Engineering at the University of South Carolina, Columbia who provided valuable insight into his team's experimental work and whose paper inspired this thesis.

TABLE OF CONTENTS

Chapter	Page
ABSTRACT.....	iii
ACKNOWLEDGMENTS	iv
TABLE OF CONTENTS.....	v
LIST OF TABLES.....	vii
LIST OF FIGURES	viii
NOMENCLATURE	xi
CHAPTER I: Introduction	1
CHAPTER II: Background and Literature Review	3
Fluid Dynamics.....	3
Laminar Flow	8
Turbulent Flow.....	9
Turbulence in Microfluidics	12
Mixing.....	12
Heat Exchangers	13
Heat Transfer	15
Optimization	17
Driving Forces	18
Electroosmosis	20
DC Electroosmosis.....	23
AC Electroosmosis.....	24
Electrophoresis.....	26

Dielectrophoresis (DEP)	26
CHAPTER III: METHODOLOGY	29
Wang et al. (2014).....	29
COMSOL Multiphysics	33
Solvers.....	34
Discretization	35
Defining Geometry and Materials	38
Physics Coupling	40
Entropy.....	51
Mesh Study	53
CHAPTER IV: RESULTS.....	59
Points of Interest	59
Features of Turbulence	65
Fast Diffusion.....	65
High Dissipation	69
Irregularity	73
3-D Flow	74
Entropy.....	77
CHAPTER V: CONCLUSIONS	81
REFERENCES	85
APPENDIX A.....	95
APPENDIX B	105

LIST OF TABLES

Table	Page
Table 1: Reynolds and Pressure Drop.....	8
Table 2: Microfluidic Flow Manipulation, Forces and Fields	19
Table 3: Inlet & Outlet Conditions	32
Table 4: Flow Values of Interest.....	32
Table 5: Coordinate conversion	38
Table 6: Initial & Boundary Conditions (20V _{pp} shown).....	45
Table 7: Na and Cl Diameters and Particle Drag Force.....	48
Table 8: Flowrate	63
Table 9: T_e vs. Ra_e Result Comparison.....	73
Table 10: Mean u_s value comparisons	74
Table 11: Entropy components (at $t = 0.25s$).....	77

LIST OF FIGURES

Figure	Page
Figure 1: Electrical Double Layer (EDL)	21
Figure 2: Electroosmotic Flow Profile.....	22
Figure 3: AC Electroosmotic Flow	24
Figure 4: Transverse Electroosmosis	25
Figure 5: Problem Simplification.....	30
Figure 6: Microchannel Drawing.....	31
Figure 7: Simulation Design Process	37
Figure 8: Fluid Domains	39
Figure 9: Electrode Placement.....	39
Figure 10: Transport Coupling.....	40
Figure 11: Physics Relations & Coupling.....	42
Figure 12: Simplified Physics Relations.....	43
Figure 13: Conflicting Boundary Conditions	44
Figure 14: Step Function.....	44
Figure 15: Effective Diameter	48
Figure 16: Particle Force Balance.....	49
Figure 17: Manual Physics Coupling.....	50
Figure 18(a): Comparison of total Te values for different mesh resolutions	55
Figure 19: Comparison of total Entropy values for different mesh resolutions	55
Figure 20: Coarse Mesh	56
Figure 21: Coarse Mesh (in channel).....	57

Figure 22: Point at (100, 0, 0) μm	59
Figure 23: Transverse line at $x = 0\mu\text{m}$	60
Figure 24: Transverse line at $x = 100\mu\text{m}$	60
Figure 25: Transverse line at $x = 100\mu\text{m}$, $y = 0\mu\text{m}$	61
Figure 26: Transverse line at $x = 100\mu\text{m}$, $y = (-100)\mu\text{m}$	61
Figure 27: Volume from trailing edge to $x = 0.5\text{mm}$	62
Figure 28: Flow rate through surface $x = 100\mu\text{m}$	62
Figure 29: Body Force (N/m^3).....	64
Figure 30: Space Charge Density (C/m^3).....	64
Figure 31: Streamlines - 0V_{pp} (unforced).....	65
Figure 32: Streamlines - 8V_{pp}	66
Figure 33: Streamlines - 20V_{pp}	66
Figure 34: NaCl Concentration Slices (mol/m^3) - 0V_{pp} (unforced).....	67
Figure 35: NaCl Concentration Slices (mol/m^3) - 8V_{pp}	67
Figure 36: NaCl Concentration Slices (mol/m^3) - 20V_{pp}	68
Figure 37: Downstream NaCl concentration (mol/m^3) - 20V_{pp}	68
Figure 38: T_e vs Ra_e	71
Figure 39: T_e vs Ra_e	71
Figure 40: T_e vs Ra_e	72
Figure 41: T_e vs Ra_e (Wang et al. experimental data).....	72
Figure 42: u_s vs time.....	74
Figure 43: Transverse view of 3D velocity streamlines.....	75
Figure 44: Zoom of Figure 43.....	75

Figure 45: Te vs z (inhomogeneity of flow in transverse plane).....	76
Figure 46: Te vs z (Wang et al. experimental data)	76
Figure 47: Entropy generated by flow	78
Figure 48: Entropy generated by species transport.....	78
Figure 49: Total Entropy generated	79
Figure 50: Streamlines $0V_{pp}$	105
Figure 51: Streamlines $0V_{pp}$	106
Figure 52: Streamlines $8V_{pp}$	107
Figure 53: Streamlines $8V_{pp}$	108
Figure 54: Streamlines $20V_{pp}$	109
Figure 55: Streamlines $20V_{pp}$	110
Figure 56: Streamlines $20V_{pp}$	111
Figure 57: Coarser Mesh Statistics Figure 58: Coarse Mesh Statistics.....	116
Figure 59: Normal Mesh Statistics Figure 60: Fine Mesh Statistics.....	117
Figure 61: Coarser Mesh.....	118
Figure 62: Coarser Mesh (in channel)	119
Figure 63: Normal Mesh.....	120
Figure 64: Normal Mesh (in channel).....	121
Figure 65: Fine Mesh	122
Figure 66: Fine Mesh (in channel).....	123

NOMENCLATURE

A	cross sectional area of channel, m^2
C, c	concentration, mol/m^3
C_D	drag coefficient
D_{eff}	effective diameter, m
D_h	hydraulic diameter of channel, μm
\vec{E}	electric field, V/m
f	Fanning friction factor
f_f	100 kHz, forcing frequency
\vec{F}_d	drag force, N
\vec{F}_e	electrokinetic body force, N
h	heat transfer coefficient, $W/m^2 \cdot K$
I	the ionic strength of NaCl solution, mol/m^3
k	thermal conductivity, $W/m \cdot K$
k	turbulent kinetic energy (Chapter V - Conclusions)
k_b	Boltzmann's constant, $1.38 \times 10^{-23} \text{ kg} \cdot m^2 / K \cdot s$
N_A	Avogadro's number, $6.022140857 \times 10^{23}$
P, p	pressure, Pa
P_o	Poiseuille number
P_w	wetted perimeter of cross sectional area of channel, m

q_i	heat transfer into a control volume i
Q	volumetric flow rate, m^3/s
Q_{in}	inlet flow rate, m^3/s
Q_{out}	outlet flow rate, m^3/s
R	Rydberg gas constant, $8.314 \text{ J/K}\cdot\text{mol}$
Re	Reynolds number
Ra_e	electric Rayleigh number
Ra_{ec}	critical electric Rayleigh number
S_{gen}	entropy generation rate, $\text{W}/\text{m}^3\cdot\text{K}$
S'''_{gen}	entropy generation rate in finite volume, $\text{W}/\text{m}^3\cdot\text{K}$
T	temperature, K
T_o	absolute temperature of ambient temperature reservoir (constant), K
T_e	turbulent kinetic energy, m^2/s^2
T_i	temperature of boundary crossed by q_i , K
u_s	mean velocity in channel, m/s
\vec{v}	velocity field (u, v, w), m/s
v_{ep}	electrophoretic velocity, m/s
V_0	voltage applied to each electrode, V
V_{pp}	maximum peak-to-peak voltage (difference between positive and negative electrodes), V
W_{lost}	energy lost due to irreversibilities, W/m^3

Greek

Δp	pressure drop, Pa
ε	absolute permittivity
ε	vacuum permittivity, 8.854×10^{-12} F/m
ε_r	relative permittivity
ε_w	relative permittivity of water
φ	voltage potential, V
ρ	fluid density, kg/m ³
ρ_v	charge density, C/m ²
ρ_f	free charge density, C/m ²
σ_i	i^{th} component of normal stress, Pa
τ_{ij}	tangential stress, Pa
μ	dynamic viscosity, kg/m·s
μ_{ep}	electrophoretic mobility, m ² /V·s
ν	kinematic viscosity, m ² /s
ω	angular frequency, rad/s
$\vec{\omega}$	vorticity, rad/s
ζ	zeta potential, V

PAGE LEFT INTENTIONALLY BLANK

CHAPTER I: Introduction

Fluid flow in microscale devices (microfluidics) has become an important area to study for applications in recent years. With an expanding set of techniques to create microchannels of increasingly complex geometries and recent biomedical and security applications, the interest in microfluidics continues to increase. Two important applications are micro-mixing and micro heat exchangers. The difficulty in mixing and heating fluids at the microscale is that the fluid flow is almost always laminar. The chaotic nature of turbulent flow at the macroscale is useful for both mixing and heating, but is an unusual phenomenon at the microscale. Many efforts have been made to create chaotic advection in microscale applications [55], which in some sense can mimic turbulence.

Although turbulence in the laminar flow of Newtonian fluids at the micro-scale is an unusual occurrence, some recent experimental reports have claimed turbulent behavior at Reynolds numbers far below typical accepted values [26].

Computational fluid dynamics (CFD) simulations can provide a benefit to researchers as a tool to either design experiments or improve validation of experiments. Simulations require benchmarks to validate their results and these benchmarks may be numerical or experimental in nature.

Previous efforts to validate laminar microscale flow with CFD have been successful. *Passive mixing* is the attempt to use the geometry of microchannels to increase mixing efficiency; CFD simulations have been successful in validating these applications. *Active mixing* uses external forcing such as acoustically driven vibration [44] or external electric and magnetic fields [45][37] to force mixing, see Table 2 for a more complete list. Attempts to model active mixing applications are ongoing, but researchers often choose to perform experiments instead because of

the complexities involved in the modeling of these microscale phenomena. Another layer of complexity to add to the modeling of these active mixers would be the existence of low Reynolds number, electrokinetically-induced turbulence, or μ EKT [27].

This thesis is focused on CFD modeling of microscale mixing of conductive fluids driven by an externally applied electric field in order to complement recent experimental studies reported in the literature. The specific objectives of this thesis are:

- To determine the feasibility of observing turbulence in an electrokinetically-forced microfluidic mixer using CFD.
- To quantify the effects of electrokinetic forcing in microfluidic mixing using CFD.
- To quantify the entropy generation in an electrokinetically-forced microfluidic mixer using CFD.

CHAPTER II: Background and Literature Review

This Chapter presents a basic understanding of the governing principles involved in microfluidic flow and the relationships between geometry and fluid properties. While microfluidic devices involve much smaller scales than traditional fluid flow, the underlying equations hold true.

Fluid Dynamics

The concept of conservation is important in all fields of science and engineering, be it energy, mass, or forces. Fluid mass conservation, or the *continuity equation*, for an integral control volume (CV) states

$$\frac{\partial}{\partial t} M_{cv} = \sum_{in} \dot{m} - \sum_{out} \dot{m} \quad (1)$$

The differential form of equation (1), or continuity applied to a differential element, $d\vec{v}$, is

$$\frac{D\rho}{Dt} + \rho \nabla \cdot \vec{v} = 0 \quad (2)$$

where \vec{v} is the flow's velocity field with components (u, v, w). The material, or substantial derivative, operator is given by

$$\frac{D}{Dt} = \frac{\partial}{\partial t} + u \frac{\partial}{\partial x} + v \frac{\partial}{\partial y} + w \frac{\partial}{\partial z} \quad (3)$$

Assuming that the density variations, in both time and space, are negligible, equation (2) reduces to

$$\frac{\partial u}{\partial x} + \frac{\partial v}{\partial y} + \frac{\partial w}{\partial z} = 0 \quad (4)$$

and in vector notation

$$\nabla \cdot \vec{v} = 0 \quad (5)$$

The force balance for a control volume (where v_i and F_i are the i^{th} components of velocity and force, respectively) is

$$\frac{\partial}{\partial t} (Mv_i)_{cv} = \sum F_i + \sum_{in} (\dot{m}v_i) - \sum_{out} (\dot{m}v_i) \quad (6)$$

Equation (6) can be written in terms of the normal stress (σ_x), the tangential stress (τ_{xy}) and an external body force (\vec{F}) for a two-dimensional flow as

$$\rho \frac{Du}{Dt} = -\frac{\partial \sigma_x}{\partial x} + \frac{\partial \tau_{xy}}{\partial y} + F_x \quad (7)$$

with the stress components defined as

$$\sigma_x = p - 2\mu \frac{\partial u}{\partial x} + \frac{2}{3}\mu \left(\frac{\partial u}{\partial x} + \frac{\partial v}{\partial y} \right) \quad (8)$$

$$\tau_{xy} = \mu \left(\frac{\partial u}{\partial y} + \frac{\partial v}{\partial x} \right) \quad (9)$$

Combining equations (7) - (9) the x-component of the Navier-Stokes (NS) equation becomes

$$\rho \frac{Du}{Dt} = -\frac{\partial p}{\partial x} + \frac{\partial}{\partial x} \left[2\mu \frac{\partial u}{\partial x} - \frac{2}{3}\mu \left(\frac{\partial u}{\partial x} + \frac{\partial v}{\partial y} \right) \right] + \frac{\partial}{\partial y} \left[\mu \left(\frac{\partial u}{\partial y} + \frac{\partial v}{\partial x} \right) \right] + X \quad (10)$$

For a constant viscosity fluid, equation (10) becomes

$$\rho \left(\frac{\partial u}{\partial t} + u \frac{\partial u}{\partial x} + v \frac{\partial u}{\partial y} + w \frac{\partial u}{\partial z} \right) = -\frac{\partial p}{\partial x} + \mu \left(\frac{\partial^2 u}{\partial x^2} + \frac{\partial^2 u}{\partial y^2} + \frac{\partial^2 w}{\partial z^2} \right) + X \quad (11)$$

In vector notation Navier-Stokes is

$$\rho \frac{D\vec{v}}{Dt} = -\nabla P + \mu \nabla^2 \vec{v} + \vec{F}_e \quad (12)$$

A complete derivation can be found in Bejan [3].

The right-hand side of NS is made up of a pressure term, a non-linear inertial term and an externally applied force to the bulk fluid flow. In the formulation of Navier-Stokes shown in equation (12), \vec{F}_e is an *electrical* body force (also volume force [69]) due to an electric field acting on the conductive fluid. See Table 2 for a list of additional forces that could be added as body forces. While this term is typically treated as zero unless considering gravity effects, it will be discussed in depth in this thesis as it is the basis for the electrokinetic forcing effect under investigation. In the context of this thesis, this force is defined by Wang et al. as

$$\vec{F}_e = \rho_f \vec{E} - \frac{1}{2} (\vec{E} \cdot \vec{E}) \nabla \varepsilon + \frac{1}{2} \left[\rho \vec{E} \cdot \vec{E} \left(\frac{\partial \varepsilon}{\partial \rho} \right) \right]_T \quad (13)$$

where ε is the fluid permittivity, and ρ is the fluid density [25] [27] and ρ_f represents the free charge density

$$\rho_f = - \frac{\varepsilon \vec{E} \cdot \vec{\nabla} \sigma}{\sigma} \quad (14)$$

From this it can be seen that the larger the conductivity gradient, the larger the electrokinetic force. The RHS terms in equation (13) represent the contributions due to the Coulomb force, the dielectric force and the force due to thermal expansion, respectively.

Fluid flows are deemed either laminar or turbulent based on the value of the Reynolds number (Re), which is defined in terms of measurable flow characteristics

$$Re = \frac{\rho v D_H}{\mu} = \frac{\rho Q D_H}{\mu A} = \frac{v D_H}{\nu} \quad (15)$$

where ρ is the fluid density, v is the flow velocity, μ is the dynamic viscosity ($\nu = \mu^{-1}$), Q is the flow rate, A is the cross sectional area, and P_w is the wetted perimeter of the channel. The hydraulic diameter is the equivalent diameter of a cross sectional shape other than circular given by

$$D_H = 4 \frac{A}{P_w} = \frac{2ab}{a+b} \quad (16)$$

Reynolds number is a ratio of nonlinearity to viscous dissipation, as seen in the third form of equation (15). In low-Reynolds microfluidic flow, it is widely accepted in science and engineering that the flow is always laminar for Newtonian fluids, [27]. The critical Reynolds number for a flow is the value at which laminar flow begins to transition to turbulent. A flow's Reynolds number for a fixed geometry is relatively easy to manipulate by choice of fluid, or by simply changing the velocity, see equation (17).

Table 1 shows example flow calculations of Reynolds, flow rate and pressure drop for three geometries using equations (15)-(21). One rectangular microchannel and two macroscale channels of similar hydraulic diameters, one rectangular channel (in red) and one pipe flow (in blue), are shown using water as a fluid over a channel length, l of $\sim 300\mu\text{m}$.

The volumetric flow rate Q is obtained using

$$Q = vA \quad (17)$$

and the pressure drop across the length l is

$$\Delta p = 2f \frac{l}{D_h} \rho v^2 = 2f \frac{l}{D_h} \rho \left(\frac{Q}{A}\right)^2 \quad (18)$$

The fanning friction factor f is constant for fully-developed, laminar flow. It can be derived from the shear stress in the flow at the wall, τ_w which leads to the Poiseuille number-dependent form

$$f = \frac{Po}{Re} \quad (19)$$

The Fanning friction factor for circular channels has an accepted value of

$$f = \frac{16}{Re} \quad (20)$$

From Kandlikar, in rectangular channels with aspect ratio (defined opposite of typical) $\alpha_c = a/b$, where $a < b$ [12]

$$Po = 24(1 - 1.3553\alpha_c + 1.9467\alpha_c^2 - 1.7012\alpha_c^3 + 0.9564\alpha_c^4 - 0.2537\alpha_c^5) \quad (21)$$

Table 1 illustrates the large increase in pressure loss by moving from the macro- to microscale; for the same turbulent-range Reynolds number the pressure loss is 6 orders of magnitude higher in the microchannel while the flow rate required is 2 orders of magnitude larger. Highlighted cells confirm that, at the macroscale, geometry (round vs. rectangular) has a much smaller effect on the pressure and flow rates than channel scale.

Fluids

Before discussing laminar vs. turbulent flow, it should be pointed out that this thesis limits its scope to the flow of incompressible, Newtonian fluids. There are multiple examples in the

literature demonstrating enhanced mixing, heat transfer and/or flow instability in microfluidics using non-Newtonian fluids, viscoelastic, or nanofluids [1] [2] [4] [5].

Table 1: Reynolds and Pressure Drop

Rectangular Tube (micro)										
a	b	A (m ²)	Q (m ³ /s)	u (m/s)	ρ (kg/m ³)	D _h (m)	μ (Pa-s)	Re _{le}	f (= Po/Re)	Δp (Pa)
1.56E-04	2.40E-04	3.75E-08	1.50E-10	0.004	1000	1.89E-04	0.001	0.757	19.515	0.99
			1.50E-09	0.04				7.57	1.952	9.90
α	α_c		1.50E-08	0.4				75.70	0.195	99
1.536	0.651		1.50E-07	4				757.0	1.95E-02	990
			1.50E-06	40				7570	1.95E-03	9900
Channel Length (l)			1.50E-05	400				75695	1.95E-04	9.90E+04
3.00E-04			1.50E-04	4000				756951	1.95E-05	9.90E+05
Rectangular Tube (macro)										
a	b	A (m ²)	Q (m ³ /s)	u (m/s)	ρ (kg/m ³)	D _h (m)	μ (Pa-s)	Re _{le}	f (= Po/Re)	Δp (Pa)
1.56E-02	2.40E-02	3.75E-04	1.50E-06	0.004		1.89E-02		75.71	0.195	9.90E-05
			1.50E-05	0.04				757.1	0.020	9.90E-04
α	α_c		1.50E-04	0.4				7571	1.95E-03	0.010
1.536	0.651		1.50E-03	4				7.57E+04	1.95E-04	0.10
			1.50E-02	40				7.57E+05	1.95E-05	0.99
Channel Length (l)			0.15	400				7.57E+06	1.95E-06	9.90
3.00E-04			1.50	4000				7.57E+07	1.95E-07	98.97
Circular Tube (macro)										
		A (m ²)	Q (m ³ /s)	u (m/s)	ρ (kg/m ³)	D _h (m)	μ (Pa-s)	Re	f (=16/Re)	Δp (Pa)
		4.91E-04	1.96E-06	0.004		2.50E-02		100	0.16	6.14E-05
			1.96E-05	0.04				1000	0.016	6.14E-04
			1.96E-04	0.4				10000	1.60E-03	0.006
Channel Length (l)			1.96E-03	4				1.00E+05	1.60E-04	0.06
3.00E-04			1.96E-02	40				1.00E+06	1.60E-05	0.61
			0.196	400				1.00E+07	1.60E-06	6.14
			1.963	4000				1.00E+08	1.60E-07	61.44

Laminar Flow

Laminar flow is traditionally defined as flow that has a low Reynolds number, with “low” being a relative term. In macroscale pipe flow, the laminar transition begins at approximately Reynolds number less than 2100 with fully developed turbulence greater than 4000 [19] while one study of rectangular microchannels claims turbulence at a critical Reynolds number of 200 and fully developed turbulence at 400 using water as the working fluid [18], the results of which are

examined by Mehendale who looked at the results of multiple studies of heat exchange in micro- and meso- scale geometry [17].

The accepted position that low Reynolds number micro flows are inherently laminar for Newtonian fluids is due to the fact that the pressure term in Navier-Stokes cannot overcome the viscous forces (non-linear term) to create a large enough inertial term to create turbulence [26] [27] [29]. Additionally, it is commonly believed that only laminar or forced chaotic flow can exist in microfluidic devices due to the low Reynolds numbers, even if forced instability has been applied [27].

This is supported by the fact that, in high Re number flow without any external forces (i.e. the R.H.S. of equation (12) has only a pressure and inertial term), the strong non-linear inertial effects dominate and lead to turbulence suggesting that it is a nonlinear phenomenon [5]. Logically, if the term responsible for turbulence is small in low Reynolds flow, then turbulence would need another source to manifest. The Wang et al. experiments, if validated as true turbulence instead of chaotic advection, would have far reaching effect on the field of microfluidics.

Turbulent Flow

It seems appropriate to begin this section with the still-true words with which Sir Horace Lamb began his 1932 discussion on turbulence, “It remains to call attention to the chief outstanding difficulty in our subject.” [57]. The fact that turbulence is still troublesome to researchers 85 years later is a testament to the nature of the subject. Turbulence, by its truly random nature, is difficult to define although its irregularity is such that it can be described by the laws of probability [10]. Because of this there is no commonly accepted definition of turbulent flow and

so researchers are left to identify it by its features [5] which Wang, Yang & Zhao specify in their papers [26] [29] [30]. The motion in spatial and temporal scales implies many degrees of freedom being excited [5], lending to increased computation expense for solving computer models.

In typical undergraduate fluids courses a student becomes well acquainted with the Navier-Stokes equation, as shown in equation (12), as well as Re number, and their relation to laminar flow. As these courses usually focus on macro-flow, any foray into the world of turbulence is usually limited to introductory exercises using well-established theory and equations. For example, in pipe flow starting from a velocity and Reynolds number of zero (rest) and slowly increasing to a steady-state (amid various assumptions), the flow is laminar for a range of $0 < Re < 2100$ [11]. Most papers on the topic of microfluidic flow agree that this roughly holds into the micro geometry range under normal circumstances [26] [27]. Stated indicators of turbulence are: fast diffusion, random motion, high dissipation rate, continuous flow, multi-scale eddies, 3-D flow and high Re [26] [27] [29] [30].

One research group (Wang, Yang and Zhao) has presented evidence of pressure driven, electrokinetically forced flow displaying low Reynolds number (on the order of 1), Newtonian turbulence by adding an electrokinetic body force [26] [27] [29] [30], which theoretically implies more efficient mixing and heat transfer, in microchannels.

But first, the basics; what is turbulence? The Webster's New Collegiate Dictionary defines turbulence as "departure in a fluid from a smooth flow" and is characterized by the presence of irregular eddying motions where the vorticity [48] is

$$\vec{\omega} \equiv \vec{\nabla} \times \vec{u} \neq 0 \quad (22)$$

In the 1959 text *Turbulence: An Introduction to Its Mechanism and Theory*, Hinze offered his preferred definition of turbulence as “an irregular flow in which the various quantities show a random variation with time and space coordinates, so that statistically distinct average values can be discerned” [10].

According to Wang, Yang and Zhao, “it is commonly believed that the flow in microfluidics, where typical Reynolds number is on the order of 1 or lower and the fluids are often approximately seen as Newtonian, can only be laminar and cannot be turbulent.” Their experiment was based on a pressure-driven, electrokinetically forced flow in microchannels with a Re on the order of 1 [26]-[32]. They cite other research done [55] using the same concept as theirs that didn’t create turbulence but rather chaotic advection. The analysis of their experimental results begins with Navier-Stokes Eq. (12) and the investigation of the effect of an applied AC electric field to the flow. While the differences between chaotic flow and turbulent flow are outside the scope of this thesis, the reader can investigate this topic further using sources from the literature [4] [28].

The group also describe the apparatus they developed [26] [29] [30] [32] to visualize the flow in the microchannel flow, the LIFPA system, which would demand more study if physical experiments were to be developed to accompany the computer simulations of this thesis project. Of note is the “sufficiently high” AC or DC voltage difference they used was around $36 V_{pp}$ at its highest value, which would be quite feasible in the lab using a power supply or even batteries. Their conclusions discussed their evidence supporting the claim that they had indeed created true turbulence and went into detail on the observed hallmarks of turbulence; fast diffusion, high dissipation, irregularity, multi-scale eddies, continuity and 3-D flow.

Turbulence in Microfluidics

Two of the major foci in microfluidics research are increasing mixing and heat transfer performance. The literature includes numerous examples of each of these as well as their importance to scientific research, [13] [35] with mixing having the greatest breadth of existing research due to the extensive applications for it in the fields of biology [40] [43] [42] [51], and lab-on-a-chip (LOC) design [29] [30] [50]. While “increasing the contact area between the species to be mixed is one of the most efficient means of enhancing the diffusive mixing effect” [13], it is also the best way to increase heat exchanger performance. Turbulence can accomplish this by randomly updating the species concentration in a control volume of fluid so that local species saturation does not occur and, in the case of heat transfer, it constantly moves fluid away from a liquid/ heat source interface and replaces it with cooler fluid from the bulk flow area (typically the center of pipe flow).

Mixing

Ahmed et al. point out that mixing is important to microfluidic research because “the promise of microfluidic systems lies in their capability to utilize minute quantities of reagents to carry out reactions and analysis with high resolution in a time and cost-efficient manner” [44]. These microfluidic systems often require components that can rapidly and effectively mix different solutions in microscale however, in microfluidic flow, it is difficult to achieve the rapid and homogenous mixing of two fluids due to the low Reynolds number [44]. According to Lee et al. the goal of microfluidic mixing is to “achieve a thorough and rapid mixing of multiple samples in microscale devices” [13]. This is done by minimizing the mixing length of a micro fluid flow either *actively* or *passively*. As stated previously, passive mixing is accomplished through geometry manipulation as in [36] whereas active mixing is done via applied external forces such

as the Wang et al. experiments [26]-[32] or the forces listed in Table 2. Both processes achieve results by speeding up the natural diffusion process.

Active mixers benefit from electrokinetic effects due to the application of DC or AC electric fields, AC being the more recently explored. DC fields require a higher voltage potential to disturb the flow from the naturally laminar state (termed electrokinetic instability or EKI) using charge accumulation due to conductivity gradients in the bulk flow [29]. AC fields are capable of creating more chaotic flow at a lower voltage than DC fields as the force due to the field is constantly changing with respect to time. AC electrokinetic mixers introduce irregular flow fields by applying a pulsed electrokinetic force (through sine or square signals of frequency 0.1-5 Hz) to the fluid which perturbs the fluid as it is forcing the flow to move along the channel [13].

Heat Exchangers

Heat exchangers are used anywhere that heat needs to be removed from a fluid or a solid. As mechanical and electrical devices get smaller, the traditional heat exchanger must evolve to meet the new set of restrictions presented. These requirements are not only due to physical size restrictions but also the laws governing fluid dynamics and heat transfer. The issue is that, traditionally, the larger the exchanger the more heat transfer that could be accomplished and in the past this wasn't a problem because the devices were relatively large.

However, as modern device sizes shrink, the heat transfer requirements are increasing or, at the least, not decreasing. Eq. (23) shows that as the hydraulic diameter of the channel decreases, the convection heat transfer coefficient increases proportionally [12],

$$h = Nu \frac{k}{D_h} \quad (23)$$

where h is the heat transfer coefficient for laminar flow, k is the thermal conductivity of the fluid, D_h is the hydraulic diameter of the channel shown in equation (16) [11]. Experiments have shown that fully turbulent convective heat transfer has been reached in a Reynolds range between 400 and 1500 with a transition range that decreased as the microchannel dimension decreased [18]. The same experiments also found that the maximum laminar heat transfer occurred when the aspect ratio was 0.75 and the maximum turbulent heat transfer at 0.5-0.75, illustrating that heat transfer is affected by geometry [18]. To take advantage of this phenomenon, researchers looking for methods of shrinking a heat exchanger look to the field of micro heat exchanger (MHE) research.

Microchannel heat exchangers were first conceived of by Tuckerman and Pease in 1981 [17] [31] and have been in development ever since. But what is a MHE? The simple answer is that an MHE is a heat exchanger that is really small, but to put it more technically "...heat exchangers in which (at least one) fluid flows in lateral confinements with typical dimensions below 1 mm. The most typical such confinements are microchannels, which are channels with a hydraulic diameter below 1 mm." [23]

To provide a better definition of a MHE, it must first be determined what makes a heat exchanger in general. For a two-fluid heat exchanger, Incropera et al. defines a heat exchanger as a device that facilitates "the process of heat exchange between two fluids that are at different temperatures and separated by a solid wall..." [11]. There are 3 major types of heat exchangers: Concentric Tube, Cross-flow and Shell & Tube. The Cross-flow has the further classification of being finned or un-finned and the Concentric and Shell & Tube having either parallel or counter-flow arrangement. It is noted that a counter-flow exchanger can achieve an equal heat transfer rate to that of a parallel flow with a smaller surface area between the fluids [11]. This is

evidenced at the micro-scale by MHE experiments done in the mid 80's and early 90's using channels with similar aspect ratios where a parallel flow exchanger and a counter-flow exchanger had overall heat transfer coefficients of $4.0 \text{ kW/m}^2\text{K}$ vs $22.8 \text{ kW/m}^2\text{K}$, respectively [53].

MHEs are a specific type of heat exchanger that have a variety of uses including cooling of high heat flux electronic components, fuel cells and HVAC [31] applications. Literature shows a multitude of other applications for micro heat exchangers including a chemical resistant, ceramic counter-flow exchanger [52], Micro-Electro-Mechanical Systems (MEMS) based technology and thermal control of film deposition [53], even completely miniaturized cooling systems [17]. Because the uses are so varied, the designs for MHEs are as well which leads to a broad area of possible research: the optimization of heat transfer using microfluidics.

This thesis will explore a subset of this broad topic which is the generation of turbulent flow in microchannels, via electrokinetic forcing, to enhance heat transfer. The mechanism we will look at to gauge the impact on heat transfer will be the entropy generation in the fluid calculated from FEA data using COMSOL Multiphysics software.

Heat Transfer

Micro heat exchangers have been developed for single-phase liquid cooling since the early 1980's and since then most of the research has been on straight, constant cross-section microchannels [36][54]. Despite the performance advantages suggested by geometry manipulation, little research had been done in this area until Yang, Yeh, Liu and Yang. Their paper used three different designs (with channel diameter range of 0.1-1.0mm), compared to a

standard straight channel, to evaluate the effectiveness of applying conventional heat transfer enhancement techniques to microchannel design including:

- “1. Increase in surface area through pin fins of circular, rectangular, or other streamlined cross-sections.*
- 2. Increase in surface area and heat transfer coefficient through interrupted and staggered strip-fin design, or any other advanced design similar to the compact heat exchanger surfaces.*
- 3. Increase in local heat transfer coefficient by breaking the boundary layer through periodic flow constrictions.*
- 4. Incorporation of grooves and ridges at specified angles to the flow direction to achieve a heat transfer enhancement similar to microfin tubes.*
- 5. Incorporation of mixing features to improve the mixing between the bulk of the flow and the fluid flowing adjacent to the channel walls.”*

[36]

Most of the approaches researched by Yang, et al. restrict the flow with physical barriers that, while having some positive effect on the exchanger's thermal resistance, typically increases the pressure drop across the flow which adversely affects the frictional losses. One of the design parameters they investigated was whether or not the pressure drop across the tiny connectors used on the heat exchangers was a large source of frictional loss. This loss was subtracted from the overall pressure drop to compare the exchangers themselves. They determined that their chevron heat exchanger design had the greatest loss (five times greater than the other two, due to the connectors) contributing to it having the greatest pumping cost while also having the lowest

thermal resistance [36]. This illustrates why the concept of finding a balance between frictional losses and heat transfer efficiency is the goal of design optimization and the analysis of a system's entropy generation [6] [15].

Optimization

There are many studies in the literature concerning microfluidic flow in microchannels but when the additional parameters of heat exchange *and* low Reynolds number-turbulence are included, this number drops dramatically, at least when dealing with Newtonian fluids. However, the approach of heat exchanger research is the same whether it is for a HVAC system in a skyscraper or the cooling of a CPU in a laptop, optimization.

The goal of optimization in heat exchangers (or mixing devices) is to maximize performance and this requires the minimization of the system's entropy generation (or losses) also known as the "irreversible conversion of available energy into internal energy" [21]. These irreversibilities have thermal and frictional components which have typically been looked at separately. The frictional entropy is due to the increasing pressure drop across a microchannel as the scale diminishes (even as the heat transfer increases) which limits how small a system can be before the cost due to frictional losses outweigh the heat transfer rate increases.

"What are the practical limits of such a miniaturization of heat exchangers?" This is the question asked by Martin in his text on the topic of optimal heat exchanger dimensions [16]. He discusses a shell and tube exchanger design and how the optimal flow cross-section can reduce the pumping power required in a laminar flow scheme by choosing an appropriately large value to reduce the pressure drop from inlet to outlet (i.e. the larger the diameter, the smaller the pumping power). Martin points out that miniaturization is also limited by fouling which is compensated

for by closed systems running highly purified fluids [16] which increases cost. Frictional entropy can also be increased by use of flow restricting topographical elements such as fins or surface roughness [36].

Driving Forces

In Navier-Stokes, equation (12), the body force, \vec{F}_e , is also called a driving force. This force does not have to be due to an electric field; it can be the result of many different types of applied forces (see Table 2) including gravity (the buoyancy force). The reason for applying this force can be to introduce instabilities to the flow or to dampen them though here we are interested in creating instabilities to augment the flow's ability to transfer heat or mix fluids. While this can be done by introducing physical characteristics to the channel such as fins or ridges or even roughness (which has a much greater effect at smaller scales), it is preferred to minimize the pressure drop through the system.

As the scale shrinks it becomes more and more cost prohibitive to create microfluidic devices with built-in physical elements and so other flow manipulation methods need to be researched. Stone et al. discusses areas of research relating to the manipulation of microfluidic flow. Table 2 (citations included for reference) shows a list of forces and fields that can be used to manipulate flow in microfluidics [22].

Table 2: Microfluidic Flow Manipulation, Forces and Fields

Driving Force	Sub-categorization	Remarks; Representative References
Pressure gradient ∇p		Familiar case as in pipe flow
Capillary effects	Surface tension, γ Thermal Electrical (electrocapillarity) Surface tension gradients, $\nabla\gamma$ Chemical Thermal Electrical Optical	Capillary pressure difference (e.g., Sammarco & Burns 1999) (e.g., Pollack et al. 2000; Prins et al. 2001) Typically involve thin films (e.g., Gallardo et al. 1999) (e.g., Kataoka & Troian 1999) Photoresponsive materials
Electric fields \mathbf{E}	DC electroosmosis AC electroosmosis Dielectrophoresis	Uniform velocity field Rectified flows Response $\propto \nabla E^2$
Magnetic field/ Lorentz forces	Magnetohydrodynamic stirring	(e.g., Bau et al. 2001)
Rotation	Centrifugal forces	(e.g., R.D. Johnson et al. 2001)
Sound	Acoustic streaming	

A non-forced microfluidic flow is typically driven by a pressure gradient which, from equation (18), it can be seen that as the hydraulic diameter decreases, the pressure drop increases proportionately. As discussed previously, the Navier-Stokes equation pressure term is incapable of creating or sustaining turbulence in microfluidic flow [27] without some external force. From the perspective of heat transfer, when one looks at equation (18) together with equation (23) it can be seen how they are related

$$\Delta p \propto \frac{1}{h} \quad (24)$$

The forces listed in Table 2 have historically been used for different types of flow manipulation such driving a flow through a channel with a net pressure drop across the device of zero, as in the case of DC electroosmotic pumping, or for enhancing mixing in micro devices as in

Magnetohydrodynamic stirring or AC electroosmosis. This thesis looked at the most likely of these phenomena as possible mechanisms of turbulence induction, electroosmosis and electrophoresis.

Electroosmosis

Electroosmosis has been known to scientists for over 200 years. First discovered in 1809 by Reuss, interpreted by von Helmholtz in 1879 using an electrical double layer (EDL) model, and refined in 1917 by Smoluchowski, it serves as a basis for the electroosmotic pump (EOP) used in microfluidics today [59].

EOPs can be run by an AC or DC potential and are perfect for microfluidic devices due to the fact that the pumps have no moving parts to wear out and are non-invasive to the flow which minimizes frictional losses. They can also make use of existing microscale manufacturing such as micromachining and PDMS molding. Because it is a liquid-solid interfacial phenomena, a suitable material must be used but, luckily, many substances used in microfluidics develop the necessary spontaneous charge when in contact with an aqueous solution such as silica glass [47] [59] or acrylic [27]. Electroosmotic pumps also have a wide range of applications in the medical field as they can be used with Newtonian or non-Newtonian fluids (blood being a compatible biological fluid), fluids with high or low conductivity, with drug delivery systems, and in small volume sample analysis [47].

Before talking about the types of electroosmosis, the concept of the electrical double layer (EDL) must be introduced as it is the foundation for the electroosmotic phenomena. The nonlinear Poisson-Boltzmann theory describes the EDL in the colloidal regime and there is extensive research on the topic for symmetric electrolytes [56].

An EDL is created when a charged surface attracts counter ions (oppositely charged) and repels anions (identically charged).

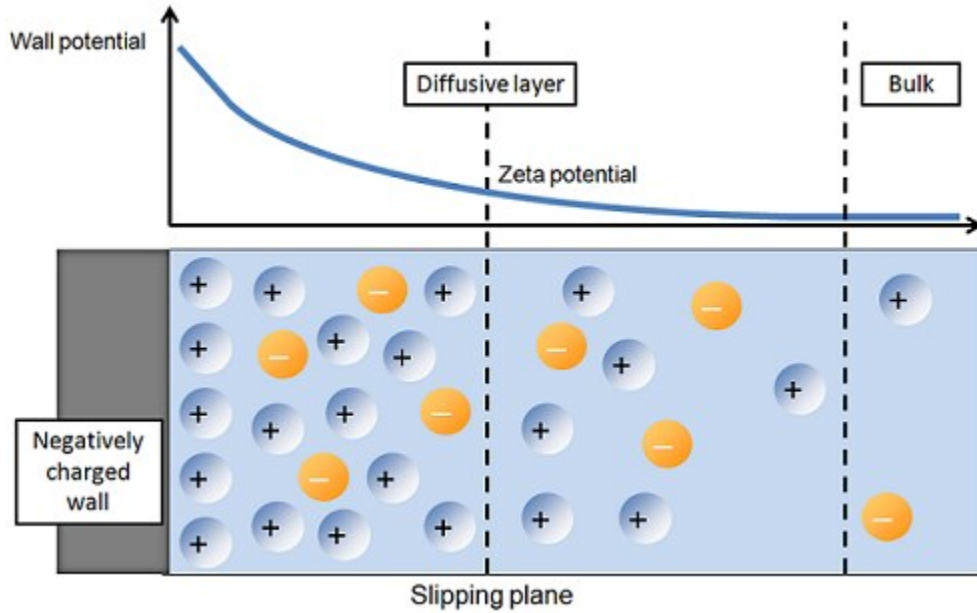


Figure 1: Electrical Double Layer (EDL)
(Used with permission from COMSOL, see [APPENDIX A](#))

Schlegel describes the electrical double layer ([Figure 1](#)):

“The EDL structure is summarized in the figure above, showing the distribution of ions as a function of the distance to the glass wall, as well as the potential (blue line on top) in the EDL versus a point in the electroneutral bulk. If we take a closer look at the diffusive layer, we notice that it can be further split into two parts that are separated by a slipping plane. This plane separates the immobile fluid on the left (attached to the surface), from the fluid that is free to move under the influence of tangential stress. An

electric field can then be used to induce the motion of the net charge in the EDL due to the Coulomb force. Further away from the wall is the third layer, the electroneutral bulk.” [49]

Electroosmosis works by taking advantage of the non-homogenous distribution of charges in the EDL as shown in cross-section in Figure 1. When the electric field is applied parallel to the negatively charged sides of the channel as in Figure 2 a bulk flow is induced along the walls in the EDL by the positive electrode repelling the abundant positively charged ions while the negative electrode attracts them. The mobile ions in this region work to drag the fluid along in the direction of the electric field. As the bulk fluid in the center of the channel (which constitutes a much larger volume than that in the EDL) is unaffected by the electric field, a slip condition develops between the bulk layer and the EDL (slipping plane in Figure 1) with resulting viscous shear stresses causing the bulk layer to be “drag along”. Caught between the channel wall and the bulk layer interface, a familiar internal flow profile develops in the EDL.

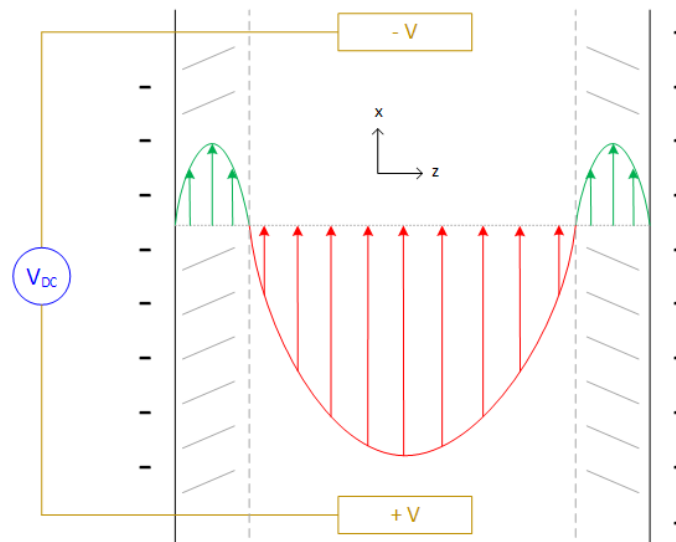


Figure 2: Electroosmotic Flow Profile

The thickness of the EDL is determined by the Debye Length

$$\kappa^{-1} = \left(\frac{\epsilon_r \epsilon_0 k_b T}{2 N_A e^2 I} \right)^{1/2} \quad (25)$$

where N_A is Avogadro's number, I is the ionic strength of the electrolyte (concentration in mol/m³), k_b is Boltzmann's constant and ϵ_r is the permittivity of the solvent.

DC Electroosmosis

DCEOPs can create pulse-free electroosmotic flows whose magnitude and direction can be modified simply by adjusting the voltage [59]. DC electroosmosis is typically used for EOPs because it gives a steady, constant flow pattern as the voltage potential is constant. Because DCEOPs can be run by batteries, they make an excellent candidate for portable point-of-care (POC) systems [59], chemical and biological detectors and small-sample analysis packages as well as drug delivery systems [47].

DCEOPs typically only use a single fluid as their primary application is creating electroosmotic flow. In the case study done by Wang et al. [26] the instability desired required the use of the more recently popular AC Electroosmosis; the point of the experiment was not to create a pumping action but rather to perturb the flow so as to create turbulent behavior. Another drawback to using DCEOPs in the search for low Re turbulence in a lab-on-chip design is that, at low frequencies, electrolysis causes the formation of bubbles on the electrodes [59]. This would be detrimental to most micro-lab functions [26], which is one of the primary applications envisioned for the low Re turbulence. Wang et al. specifically chose a high forcing frequency, $f_f = 100 \text{ kHz}$, in their paper to avoid electrolysis though they could have used a lower frequency to achieve greater instability [26].

AC Electroosmosis

AC Electroosmosis has not been used for pumps historically as the time varying electric field would create no net flow in the EDL in the direction of the electric field. However, it has been demonstrated in recent work that ACEOPs *can* produce steady flow but at a lower pumping power than DCEOPs though real-world applications have not been presented at this time [59]. Instead research into ACEOPs has been focused on enhanced mixing in micro devices. The design of ACEOPs in the literature are NOT of similar design to the topic of this thesis, they are typically designed with panels of alternating panels on each side of a channel to induce instabilities and secondary flows along the walls of a microchannel [12], see Figure 3.

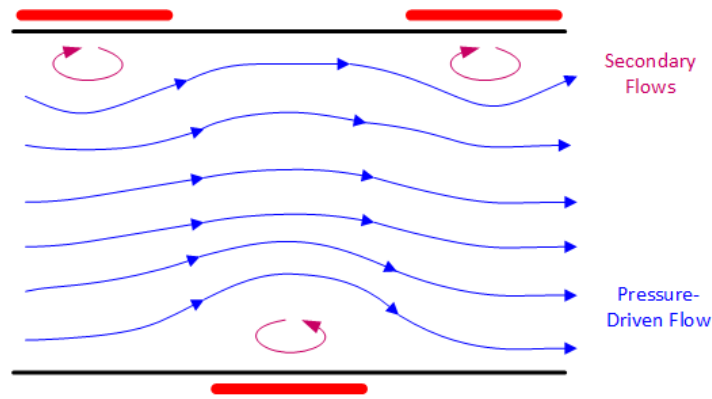


Figure 3: AC Electroosmotic Flow

Early research indicated AC Electroosmosis to be a good candidate for, at least some, of the observed phenomena seen in Wang et al. [26]. After many computational hours on BUDDY, models with the wall boundary condition set to the built in *electroosmotic velocity* condition did produce what initially looked like turbulent flow behavior. However, it required boundary conditions set such that the zeta potential was set equal to the potential on the electrodes

$$\zeta = V_0 \approx 20V \quad (26)$$

Unfortunately, this is not a realistic zeta potential value as the potential drops moving away from the charged wall, [Figure 1](#). It is assumed that electroosmosis is occurring in the transverse direction, and although it does theoretically contribute to the instability, it is minimal in relation to the body force [\[27\]](#). This is verified by the existence of turbulent behavior in the simulations without an electroosmotic boundary condition being applied, see [CHAPTER IV: RESULTS](#).

Because the electric field is AC in the Wang et al. experiment (depicted as a cross sectional area of the flow channel looking upstream in [Figure 4](#)) any electroosmotic flow along the acrylic top and bottom of the channel parallel to the electric field would create a high frequency oscillating of the fluid in the EDL, shown by red arrows. Since the electrodes in the experiment are offset instead of parallel, a slight downstream motion is also created. [Figure 4](#) depicts.

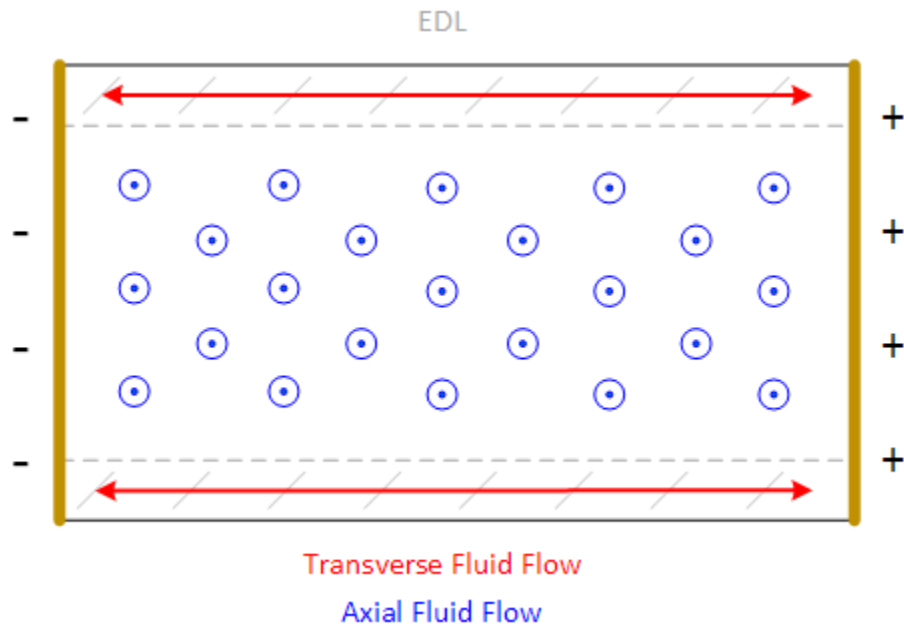


Figure 4: Transverse Electroosmosis

Electrophoresis

Electrophoresis is the drift motion of charged species [46] in a fluid under the influence of a DC electric field. Research in this field is well established due to the multitude of applications in the biological and medical fields [71].

The Debye length from equation (25) is an important parameter in species transport when calculating the electrophoretic mobility and the drag force on the fluid by the particle as it moves under the influence of an electric field.

The EDL can be approximated [72] as a slip flow boundary condition with the electrophoretic velocity

$$v_{ep} = \mu_{ep} \nabla \varphi = \left(\frac{\varepsilon_w \zeta}{\mu} \right) \nabla \varphi \quad (27)$$

Dielectrophoresis (DEP)

Dielectrophoresis is considered one of the most widely used methods of separating cells of different types and sizes [36] [37] including breast cancer cells [42] [43].

“Unlike electrophoresis, in which motion is determined by the net intrinsic electrical charge carried by a particle, dielectrophoretic motion is determined by the magnitude and polarity of the charges induced in a particle by the applied field. Furthermore, these induced charges impart the properties of an electric dipole to the particle. There is also an important experimental difference, in that electrophoresis involves the application of direct current (DC) or low frequency electric fields that are usually homogeneous,

whereas for dielectrophoresis, alternating current (AC) fields of a wide range of frequencies are used and the fields must be inhomogeneous.” [38]

Pethig states that established theory provides the dielectric force on a particle of radius r in a fluid of absolute dielectric permittivity is

$$F_{DEP} = 2\pi r^3 \epsilon \alpha \nabla E^2 \quad (28)$$

where α is the effective polarizability and ∇E^2 is proportional to the gradient and strength of the electric field [38]. This process was rejected as a possible major source for instability in this experiment as dielectrophoresis is a method of controlled manipulation of charged species, cells, bacteria and viruses [38]-[41].

PAGE LEFT INTENTIONALLY BLANK

CHAPTER III: METHODOLOGY

The simulation model was built using SolidWorks® 3D design software for the modeling of the physical geometry and COMSOL Multiphysics® for the computational modeling. The bulk of the CFD runs utilized UCO's BUDDY supercomputer cluster. BUDDY is a 38-node Linux cluster with one control node, 31 compute nodes (20 CPUs with 64GB total memory), 4 high memory compute nodes (20 CPUs with 128GB total memory) and 2 GPU nodes.

To model a physical experiment one must first determine the applicable boundary conditions, material properties and relevant physical processes involved. While this may sound simple enough, it can be quite difficult if the available information is limited or underlying physics is not fully understood. When working with the results presented in a paper, the underlying question of “why did *that* happen?” can be hidden or not understood at all which is why doing an experiment is sometimes much easier than building a computational model. A physical experiment will give results but not necessarily understanding, whereas a computational model first requires understanding to give results.

Wang et al. (2014)

One of the goals of this thesis was to determine the feasibility of observing turbulence in a low Reynolds electrokinetically-forced microfluidic flow using CFD for the purpose of studying the effect of turbulence on microchannel diffusion and heat transfer. This was to be accomplished by recreating an experimental research study [26] published by a research group at the Univ. of South Carolina that suggests the early onset of turbulence at low Reynolds number (on the order of 1) in Newtonian microfluidic flow; a previously un-reported phenomena. While researching

this thesis, additional material by the authors became available supplementing the original paper's theory and discussion [27] [28].

The first step to build a computational simulation of the paper presented by Wang et al. [26] was to recreate the geometry as a solid model, the details of the geometry can be found in the literature [26][27] and as a drawing in Figure 7. In addition to the original paper, follow-up papers [27][28] and doctoral dissertations [29][30] by contributing members were also consulted. Dr. Wang himself was consulted on topics related to the construction of the model as well as discussion of the governing physics underlying the results of their research [25]. The model was created using SolidWorks and exported as a .STEP file which was then imported to COMSOL using the *CAD Import Module* [67]. The *Live Link For SOLIDWORKS Module* was also utilized though it is available only when running the Windows version of COMSOL [68].

To simplify the boundary conditions and initial flow values, the following simplification was done with the geometry

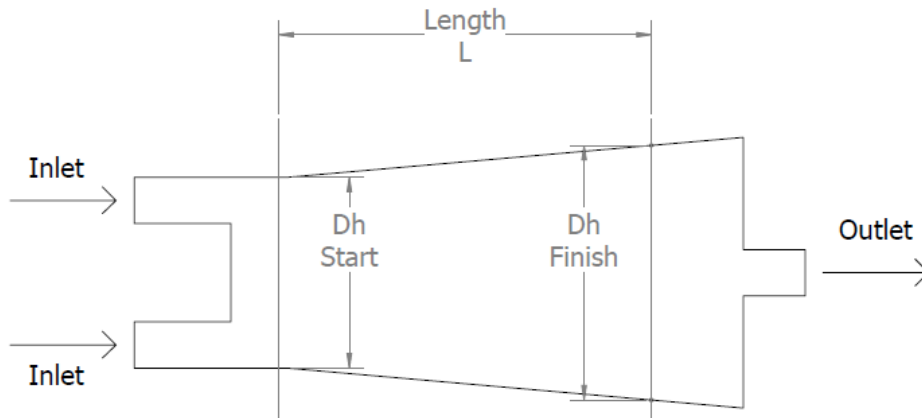


Figure 5: Problem Simplification

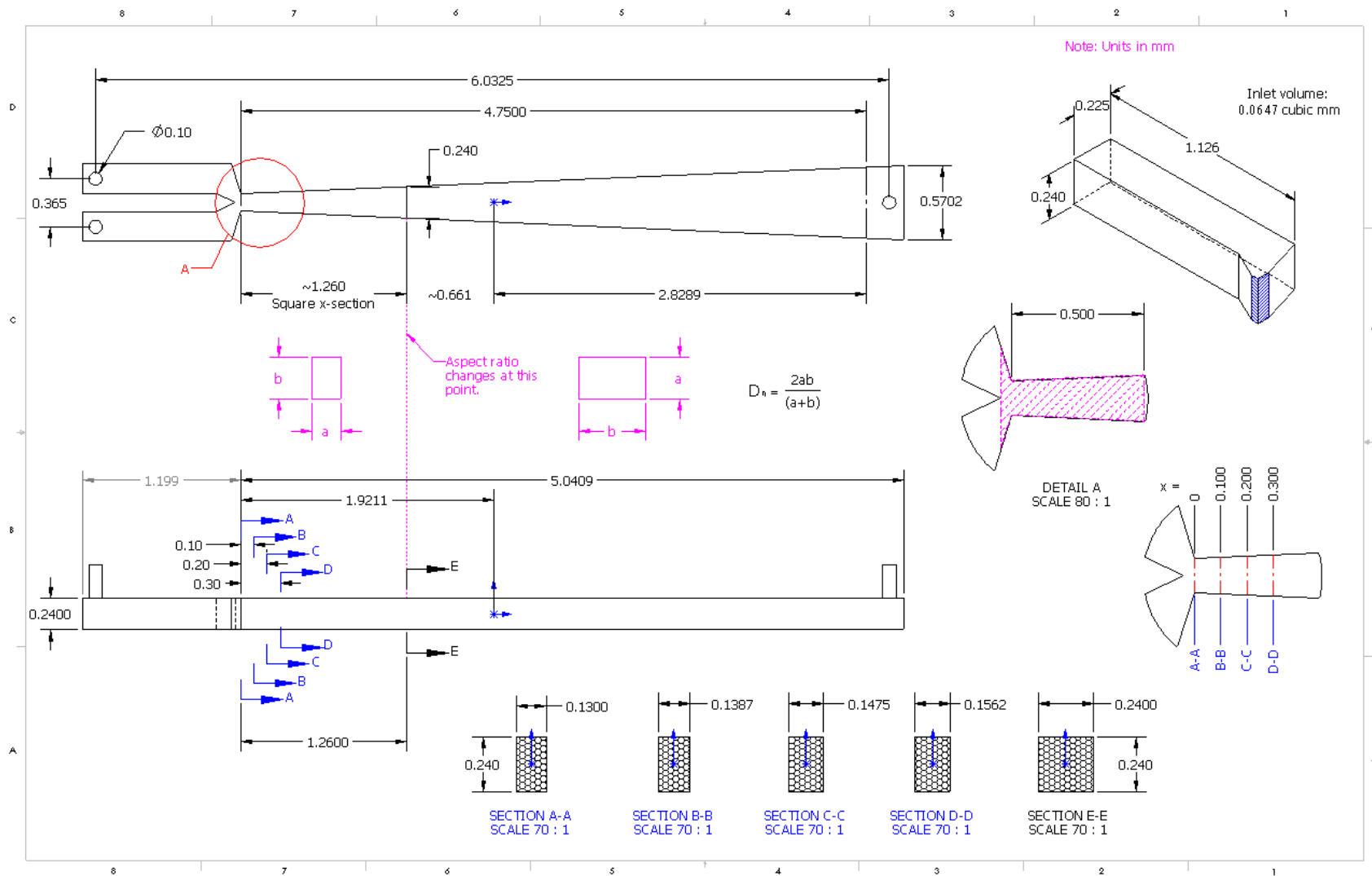


Figure 6: Microchannel Drawing

This simplification allowed for excel spreadsheets to be used for validation of laminar flow simulations to ensure boundary conditions were adequate. Using a flow rate of $2\mu\text{l}/\text{min}$ [27] ($6.66\text{e-}11\text{ m}^3/\text{s}$) at the outlet, the initial flow rates and velocities were calculated for the inlet boundary conditions. Only the first row was simulated, the others are left for future work.

Table 3: Inlet & Outlet Conditions

Inlet			Outlet		
Re_i	Q_i (m^3/s)	v_i (m/s)	Re_o	Q_o (m^3/s)	v_o (m/s)
0.424	3.33E-11	0.0042	0.848	6.66E-11	0.0085
0.848	6.66E-11	0.0085	1.70	1.33E-10	0.0170
1.70	1.33E-10	0.0170	3.39	2.66E-10	0.0339
3.39	2.66E-10	0.0339	6.78	5.33E-10	0.0678
6.78	5.33E-10	0.0678	13.57	1.07E-09	0.136
13.6	1.07E-09	0.136	27.14	2.13E-09	0.271
27.1	2.13E-09	0.271	54.27	4.26E-09	0.543
54.3	4.26E-09	0.543	108.5	8.52E-09	1.09
108.5	8.52E-09	1.085	217.1	1.70E-08	2.17
217.1	1.70E-08	2.171	434.2	3.41E-08	4.34
434.2	3.41E-08	4.342	868.3	6.82E-08	8.68

Table 4: Flow Values of Interest

Start			Finish		
Re_s	Q_s (m^3/s)	v_s (m/s)	Re_f	Q_f (m^3/s)	v_f (m/s)
0.360	6.66E-11	0.0021	0.336	6.66E-11	0.0018
0.720	1.33E-10	0.0043	0.672	1.33E-10	0.0036
1.440	2.66E-10	0.0085	1.34	2.66E-10	0.0071
2.880	5.33E-10	0.0171	2.69	5.33E-10	0.0142
5.760	1.07E-09	0.0342	5.38	1.07E-09	0.0284
11.52	2.13E-09	0.0683	10.76	2.13E-09	0.0569
23.04	4.26E-09	0.137	21.52	4.26E-09	0.1137
46.08	8.52E-09	0.273	43.03	8.52E-09	0.2274
92.16	1.70E-08	0.546	86.07	1.70E-08	0.4548
184.3	3.41E-08	1.093	172.1	3.41E-08	0.9096
368.6	6.82E-08	2.186	344.3	6.82E-08	1.8192

To help validate the simulations, the values in [Table 4](#) represent the theoretical values of the flow at the start and finish planes, separated by a length of 300 μm , which exists inside the main area of interest for turbulence generation in the flow [\[27\]](#). It can be seen that Reynolds at the start plane is approximately 0.4 which corresponds to the value given by Wang et al. [\[27\]](#).

COMSOL Multiphysics

COMSOL Multiphysics is a software package designed to enable building computational models of complex systems involving inter-dependent physics. It does this by providing the user with a modern GUI and utilizes “Physics Interfaces” which are modules prepopulated with applicable equations to apply the governing mechanisms to a model, for example the *Laminar Flow* interface utilizes the Navier-Stokes equation [\(12\)](#), and *Transport of Diluted Species* (TDS) uses the Nernst-Planck equation [\(32\)](#). This interface allows one to apply boundary conditions and assumptions, such as Stokes flow, by simply checking a box without the need to modify equations manually.

While a tutorial on working with COMSOL is outside the scope of this thesis, there are thousands of pages of documentation available. References are included that relate specifically to this project [\[66\]-\[72\]](#) as well as a link to the COMSOL Discussion Forum [\[60\]](#) and Knowledge Base [\[61\]](#) and support from application engineers available online. COMSOL also provides working models and step-by step guides available for download. In addition to these resources, three scripts were written for this thesis to walk a user through running a simulation from the command line once the COMSOL project file has been created; these scripts are available in [APPENDIX A](#).

Due to the learning curve associated with unfamiliar software, some trial and error was necessary to discover the correct way to model the interaction of the electric field and the fluid flow as it can be difficult to reconcile one's assumptions about a problem with the built-in assumptions the software is making. Another issue is that when modeling coupled physics problems computationally, the software tends to be complex with relational nuances such that a setting that doesn't work with one set of inputs may work with another making it tedious to keep track of options, not to mention menu options that are only visible when certain other options are enabled. This makes it challenging to dismiss simulation design strategies based on the fact that they have not worked in the past making the development process highly iterative, see [Figure 7](#).

Solvers

COMSOL allows the user to modify the automatically chosen default solver. The choice of direct or iterative solver is dependent on many factors, most notably the computer resources available. The *Direct Solver* requires no initial conditions and requires the greatest amount of memory and CPU resources whereas the iterative solvers do require the user to make a best "first guess" but the resources required are typically much lower, as well as having a shorter run time.

The stationary study steps in the final simulation runs were done using an iterative, segregated solver. The time dependent solver for the *Laminar Flow* step was done using a fully-coupled, iterative solver and the solver for the *Transport of Diluted Species* was a fully-coupled, direct solver (MUMPS). The iterative method uses the Newton-Raphson method and the difference between segregated and fully-coupled approaches is how the equations for the different physics interfaces are related.

For instance, while the *Fully Coupled* approach assumes all the inter-physics dependencies must be solved simultaneously, the *Segregated* approach solves the individual physics equations sequentially (issues with convergence can sometimes be solved by changing the order of the segregated steps). Each equation solution is then applied as the initial values to the next equation and an iterative process is completed between the different physics. The different types of coupling can be seen later in this thesis in the [Physics Coupling](#) section.

Because COMSOL automatically detects which type of solver is needed to compute a solution, based on geometry and computer hardware architecture, the choice to solve in the GUI or as a batch job was mostly personal preference, the main exception being when more than 64GB of memory was needed which required a batch job run on a high-memory node on Buddy (high-memory nodes have 128 GB of RAM). A GUI job can be stopped mid-way through and restarted later and it produces convergence plots (with an iterative solver) but must be saved manually after completion before Buddy's cluster management system (SLURM) terminates, else the solution will be lost. In contrast, a batch file saves itself *then* shuts down after a solution is reached and can be left to run unattended, but less solution feedback is accessible during calculation.

Discretization

The fluid discretization setting for the *Laminar Flow* interface was set to **P2 + P1** (explanation follows). The *Transport of Diluted Species* elements were cubic and the *Electric Currents* elements were quadratic.

From the in-GUI help descriptions for fluid element orders [66]:

- **P1+P1**: linear elements for both the velocity components and the pressure field. Linear elements are computationally cheaper than higher-order elements and are also less prone to introducing spurious oscillations, thereby improving the numerical robustness. In other words, this can be computationally efficient but requires streamline stabilization of the Navier-Stokes equations. This is the default element order for the Laminar Flow and Turbulent Flow single-phase flow interfaces and the discretization of fluids in the multiphase flow interfaces.
- **P2+P1**: second-order elements for the velocity components and linear elements for the pressure field. Second-order elements work well for low flow velocities. This is the default element order for the Creeping Flow interface.
- **P3+P2**: third-order elements for the velocity components and second-order elements for the pressure field. This can add additional accuracy but it also adds additional degrees of freedom compared to P2+P1 elements.

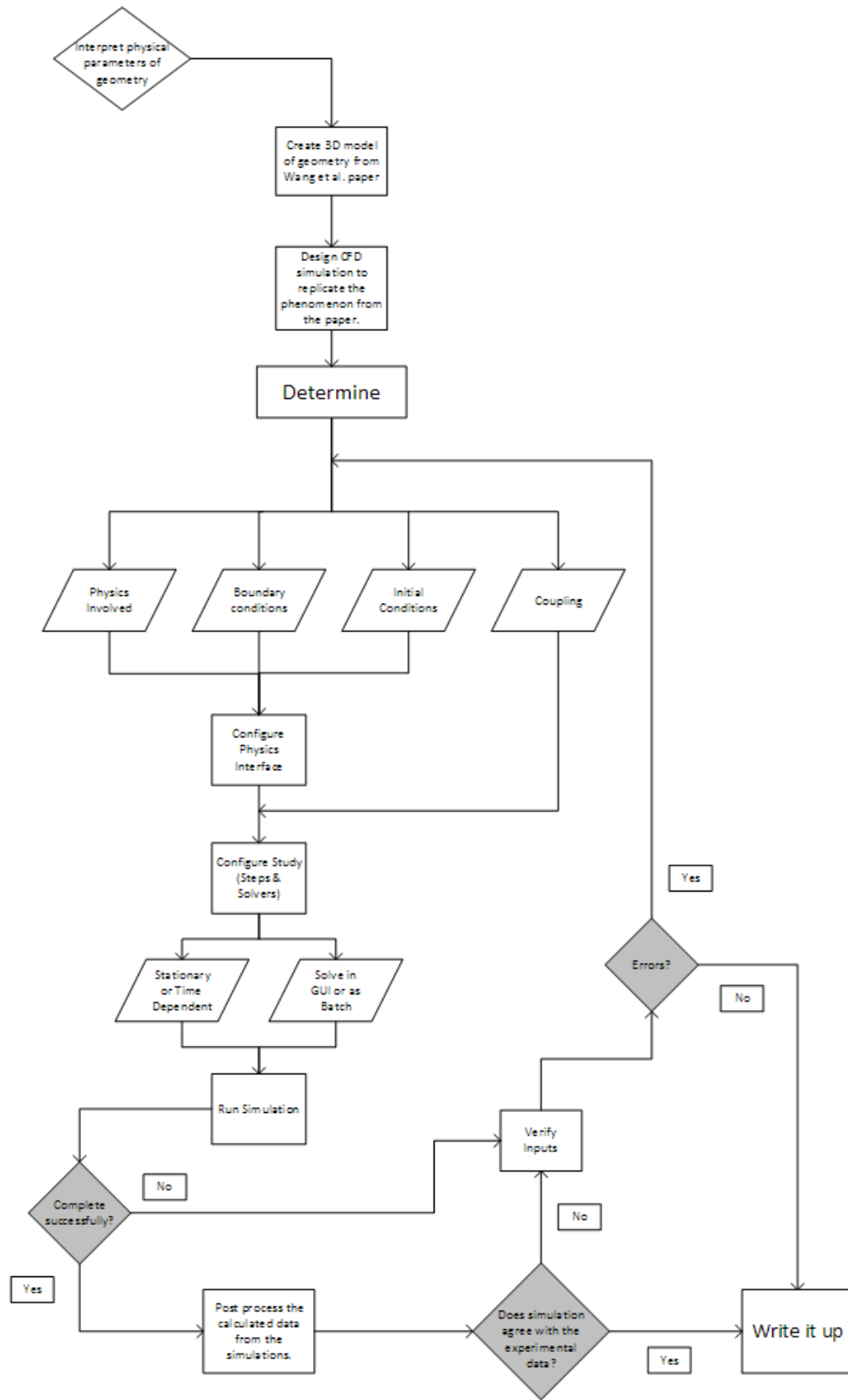


Figure 7: Simulation Design Process

Defining Geometry and Materials

The imported geometry was divided into boundaries and then the microchannel body itself was ignored leaving only the fluid domains of concern. The material and fluid selections were made based on the initial Wang et al. paper, subsequent papers and personal correspondence with the author [25] [27].

This problem was modeled using two fluids with a conductivity ratio of 5000:1 and at time $t = 0s$ the fluids are separated into two domains (see Figure 8) leaving a fluid-fluid boundary with a high conductivity gradient which was expected to be the source of the turbulence-creating body force [28] [29]. The domains were defined in COMSOL with different initial condition materials; the red fluid in Figure 8 had a material definition of dilute saline solution (2.88 mol/m^3), and the blue in Figure 8 had de-ionized (DI) water. In addition to an equal inlet velocity condition, the inlets for each domain had an *Inlet Flux* boundary condition applied to calculate the ion concentration of Na^+ and Cl^- entering the domains as part of the fluid solution. The *Inlet Flux* boundary condition multiplies the velocity on the defined boundary by the calculated velocity. The DI water domain had zero concentration added while the sodium chloride domain had equal parts (as NaCl is a 1:1 compound) of each ion added.

NOTE: All coordinates in this thesis reference the simulation geometry's coordinate system, even when referencing the experiment, so that comparisons can be made without looking to the Wang paper for clarification. Table 5 shows the conversion.

Table 5: Coordinate conversion

Experiment	x	z	y
Thesis	x	y	-z

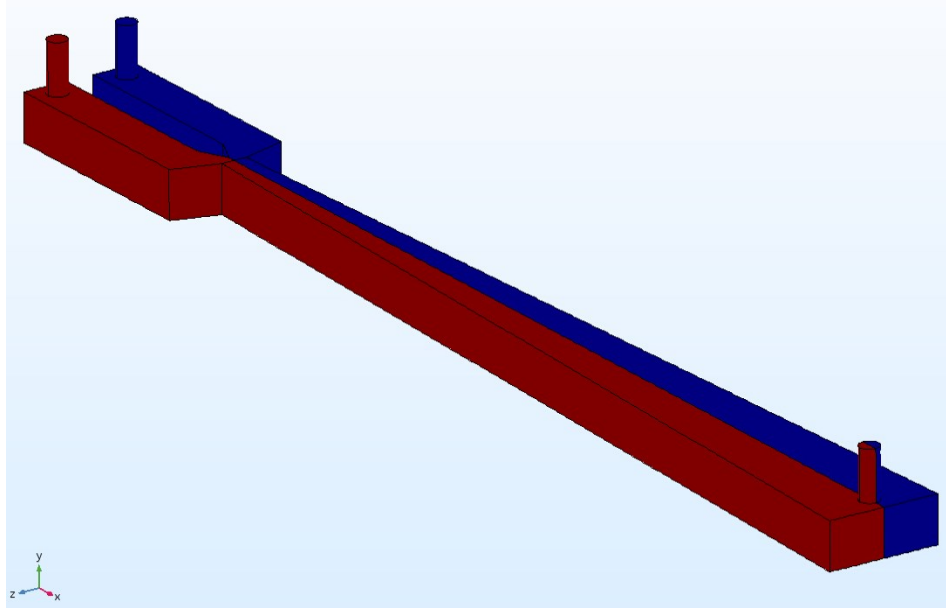


Figure 8: Fluid Domains

With the exception of the two inlets and the single outlet, all other boundary conditions were set to no-slip wall conditions. Acrylic was assigned as the wall material on all boundaries except the electrodes which were defined as gold (foil), see [Figure 9](#).

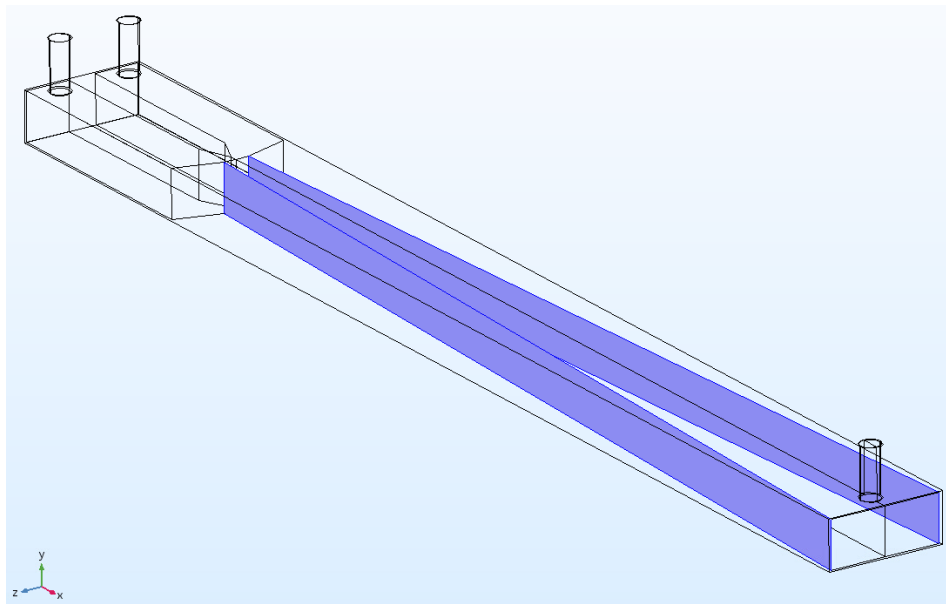


Figure 9: Electrode Placement

Physics Coupling

Physics coupling in COMSOL can be done automatically, manually or as a combination of the two. Automatic physics coupling is added by the software when two physics interfaces are added to a model where one solution can be directly used as input to the other; for example when an *Electric Currents*, *Laminar Flow* and a *Transport of Diluted Species* interface are added as shown in [Figure 10](#), the *Multiphysics* nodes of *Flow Coupling* and *Potential Coupling* are added (here the *Potential Coupling* is manually disabled to ignore species migration due to the electric field). The user determines what interfaces to use for the source and destination of the coupling which, here, tells COMSOL to use the *Laminar Flow* solution to drive the species transport due to convection. In the case of manual coupling, an example would be the definition of the electrokinetic body force shown in [Figure 17](#).

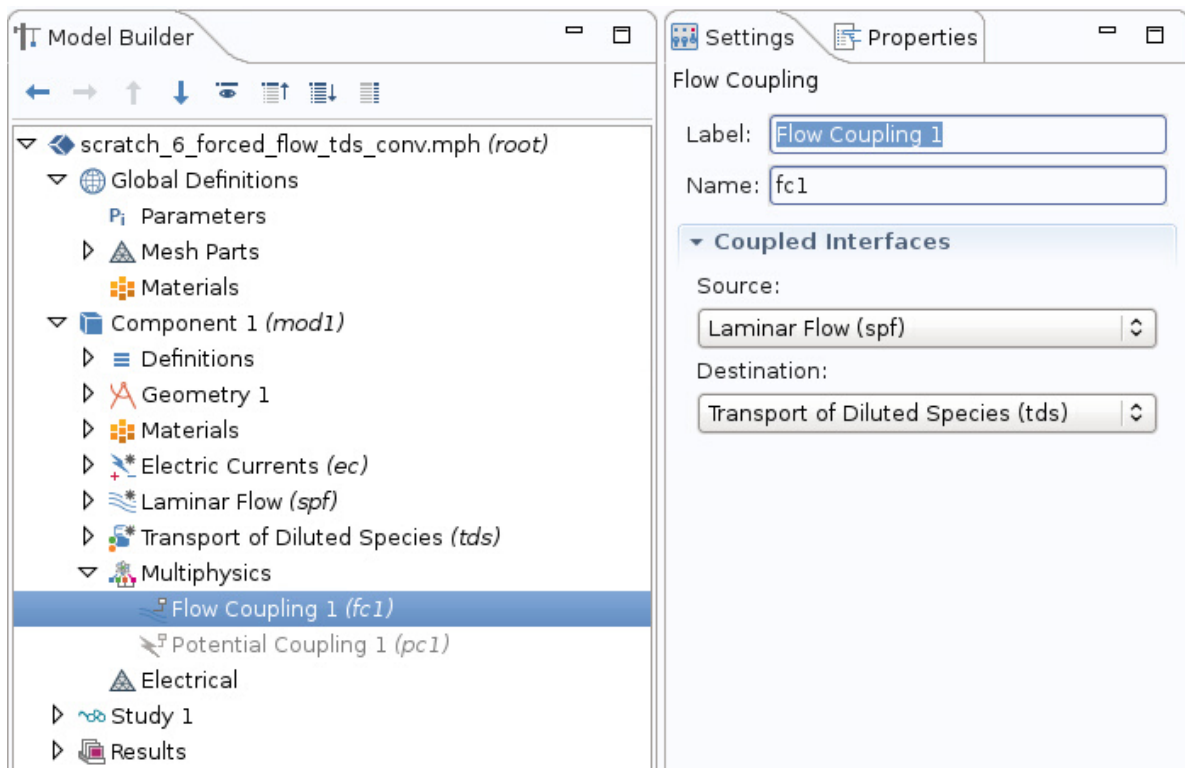


Figure 10: Transport Coupling

COMSOL defines “coupling” as [64] :

One-way coupling: Information is passed from one physics interface to the other in a single direction. (single-ended arrows in Figure 11 & Figure 12).

Two-way coupling: Information is passed back and forth between physics interface. (double-ended arrows in Figure 11 & Figure 12).

Loaded coupling: The results from one physics interface affect the loading of other physics interface.

Material coupling: The results from one physics interface affect the material properties of other physics interface.

Non-linear coupling: The results of one physics interface affect other physics interface and itself.

Fully coupled: All the types above.

Weakly coupled: The physics interface don't affect the loads/properties of other physics interface.

Strongly coupled: The opposite of weakly coupled.

The coupling relationships between the physics interfaces involved are mapped out in Figure 11. The physics interfaces are shown in circles including an optional interface that could be used to couple the species transport back to the fluid flow using the drag force generated by the movement of the particles through a viscous liquid. SS means steady state, SS-SF is steady state-

steady flow, and both are solved as Stationary study steps in COMSOL while transient is solved as Time-Dependent study steps.

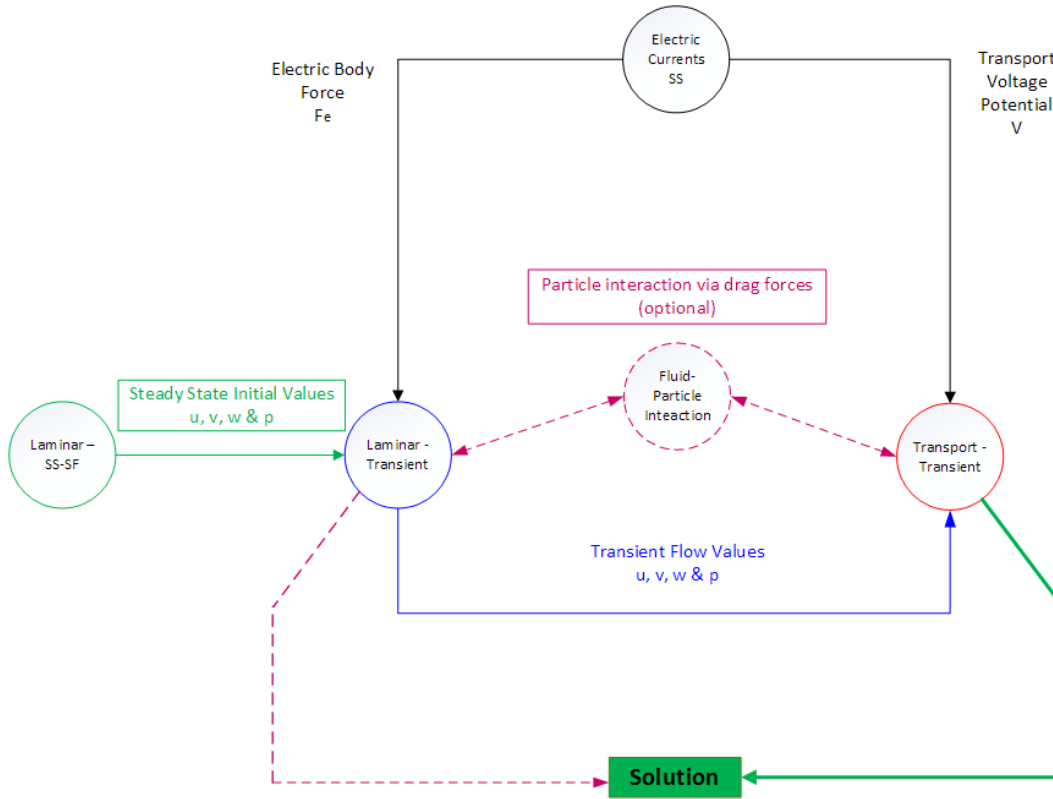


Figure 11: Physics Relations & Coupling

Due to simplifications and assumptions made about the physics involved, [Figure 12](#) shows the relational map used to design the models with the transport being included only to measure the effect of the electric field on the diffusion process. The first simplification shown here is dropping the Particle-Fluid Interaction interface due to the negligible drag forces created by the small ion diameters (see equation (34)) moving through the fluid. The second simplification was deciding to ignore the portion of the species migration through the fluid due to the electric field. This was done to more accurately show the effects that the electrokinetic force has on the species

movement compared to a flow without an electric body force applied, namely the effect on the system's entropy.

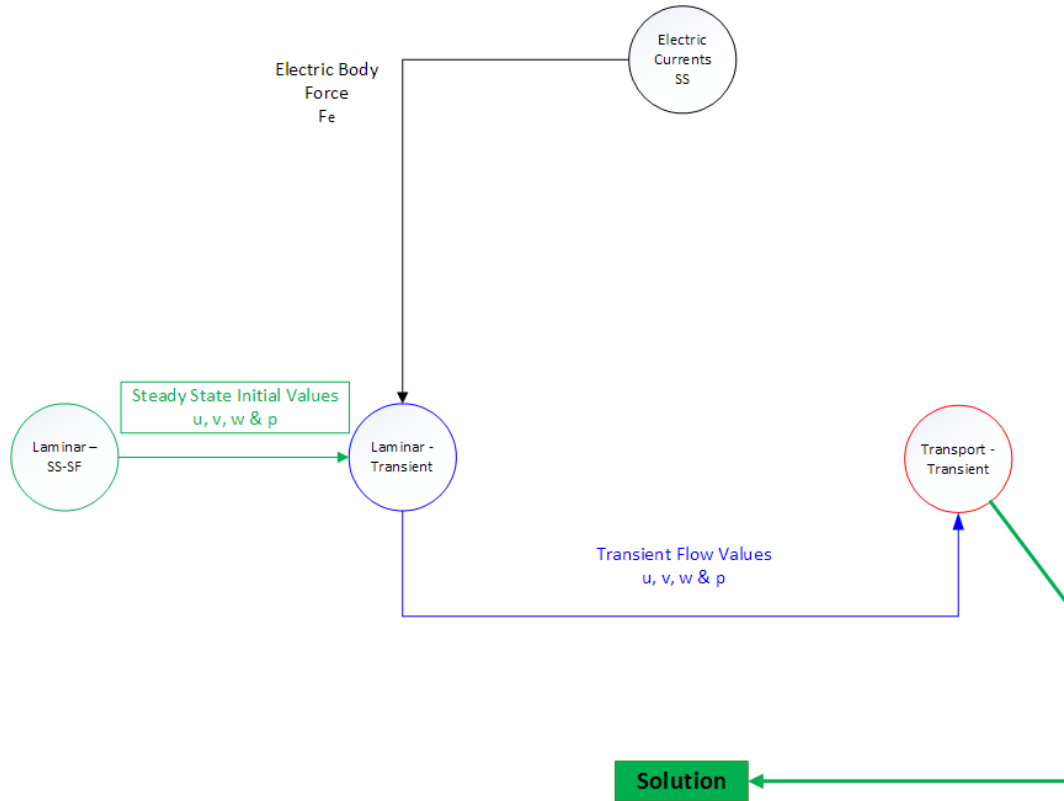


Figure 12: Simplified Physics Relations

When solving time-dependent studies, inconsistent boundary conditions can create problems with convergence and make it difficult to reach a solution. This occurs when the time-zero values and the initial conditions are not the same value. For example, when the inflow velocity at time zero is defined as $u = 1$ but the value for u *inside* the control volume is $u = 0$ an inconsistency across the inlet boundary is created, as in [Figure 13](#).

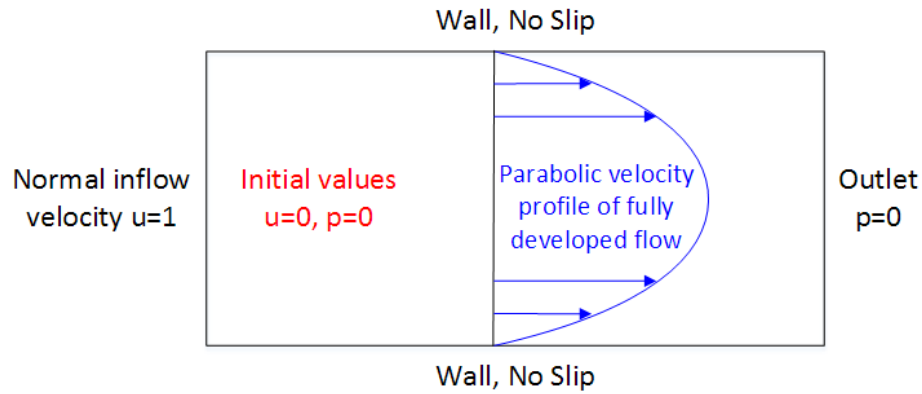


Figure 13: Conflicting Boundary Conditions

To prevent conflicting boundary conditions when defining initial conditions there are two options [61]: run a stationary step and use its solution as the initial conditions for a time dependent study step *or* define a step function (see Figure 14) and apply it to the input parameter to allow the values to “ramp up” to the defined initial boundary condition to prevent the inconsistency, the former was chosen here. If all steps (Stationary and Time-Dependent) are part of a single Study, the coupling of stationary solution to time-dependent initial conditions is made automatically by COMSOL unless overridden by the user.

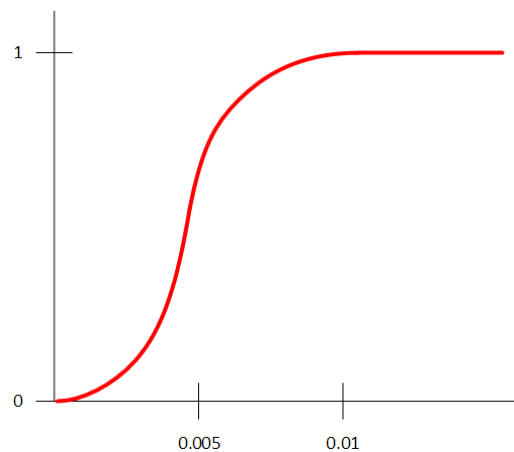


Figure 14: Step Function

Table 6: Initial & Boundary Conditions (20V_{pp} shown)

	Voltage Potential (V)	Velocity (m/s)	Pressure (Pa)	Flowrate (m ³ /s)	Body Force - i th component (N/m ³)	NaCl Concentration (mol/m ³)
Electric Current (Positive Electrode)	10				$\rho_f * E_i$	
Electric Current (Negative Electrode)	-10				$\rho_f * E_i$	
Laminar Flow (at each inlet)		0.0042				
Pressure (at outlet)			0	6.66E-11		
Initial Conditions (internal)	0	0	0	0		
Transport of Diluted Species						2.88
Species Flux (at each inlet)		v				2.88 * v

Table 6 shows the initial and boundary conditions chosen for the simulations, with swept voltage values highlighted in green. The flow rate shown is theoretical based on hand calculations using equation (17).

The electric field was solved using the *Electric Currents* physics interface as an electrostatic field with a user input voltage potential. This potential is defined on the electrodes on each side of the channel with a phase difference of 180° for example a potential of ± 0-10V on each electrode results in a peak-to-peak voltage of 0-20V with a phase difference of 180°. The equations solved by COMSOL are

$$\nabla \cdot \vec{j} = Q_j \quad (29)$$

$$\vec{j} = \sigma \vec{E} + \vec{j}_e \quad (30)$$

$$\vec{E} = -\nabla V \quad (31)$$

The electrostatic solution of the electric field is used as the source of the driving force in Navier-Stokes (equation (12)) and implemented in COMSOL as in equation (37). However, because this solution effectively represents a DC electric potential on the electrodes, an adjustment is made when the driving force is defined in equation (37) by multiplying the electric field components by $\cos(\omega t)$. This yields the same solution as applying the AC potential to the electrodes directly as $V_0 \cos(\omega t)$ where $\omega = 2\pi f_f$.

The Nernst-Planck equation is a mass conservation equation that describes the motion of a charged chemical species in a fluid medium [70]

$$\frac{\partial c}{\partial t} = \nabla \cdot \left[D \nabla c - \vec{v} c + \frac{Dze}{k_q T} c \left(\nabla \phi + \frac{\partial \vec{A}}{\partial t} \right) \right] \quad (32)$$

It describes the flux of ions under the influence of both an ionic concentration gradient, ∇c , and an electric field $\vec{E} = -\nabla \phi + \frac{\partial \vec{A}}{\partial t}$.

The physics interface chosen to model the species transport was *Transport of Diluted Species* (TDS). Both a large concentration gradient and an electric field are present in the Wang et al. experiment and while Nernst-Planck (equation (32)) is a stand-alone physics interface in COMSOL, it is also built-in to the TDS interface when the “migration in an electric field” option is enabled. At this time however, all simulations have been done with this option disabled. Although this interaction would exist in any physical experiment, this thesis is trying to quantify the *specific* effects due to enhanced mixing caused by μ EKT which would justify ignoring effects that would be present if an electric field was applied but μ EKT was absent. This justification relies on two assumptions: 1) that the migration due *solely* to the electric field acting on the charged species would be the same with or without turbulence and 2) the fluid-particle

interaction is negligible meaning the additional particle motion would not appreciably effect the flow, together these assumptions would render the migration inconsequential when comparing total entropies between forced and unforced cases.

For the second assumption consider the Stokes drag coefficient for a spherical particle in low-Reynolds flow is [20]

$$C_D = \frac{2F_d}{\rho v^2 A} = \frac{24}{Re} \quad (33)$$

By rearranging equation (33), and using equation (15), the drag force on a spherical particle becomes [19]

$$\vec{F}_d = 3\pi\mu\vec{v}D_{eff} \quad (34)$$

where \vec{v} is the fluid velocity relative to the particle and D_{eff} is the effective diameter of the particle

$$D_{eff} = d + 2\kappa^{-1} \quad (35)$$

The effective diameters of Sodium and Chlorine ions are roughly the same even though their *actual* diameters, d , are quite different which gives an equal drag force on each particle, (see Table 7).

Since the effective particle diameters are small (nanometer range) it is accepted practice to consider the electrophoretic force as negligible [30] along with the drag force which is negligible compared to the electric body force (simulation results show $F_e \sim 10^5$). This can be seen in

equation (28) as the electrophoretic force is dominated by the cubic radius term which in this case would make $F_{DEP} \sim 10^{-27}$.

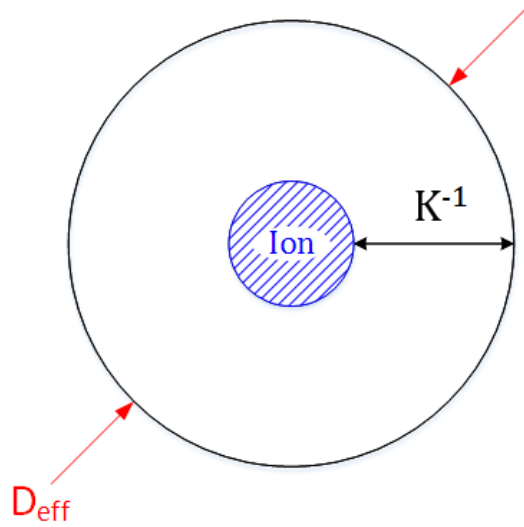


Figure 15: Effective Diameter

Table 7: Na and Cl Diameters and Particle Drag Force

	Ion Diameter (m)	Cross-sectional Area (m ²)	Effective Diameter (m)	Effective Cross-sectional Area (m ²)	Drag Force (N)
Na	350E-12	96E-21	11.7E-9	108E-18	468E-9
Cl	454E-12	162E-21	11.8E-9	110E-18	472E-9

Having already eliminated the effects of the AC electroosmotic force as a source term and looking at the balance of forces on the particle in Figure 16 it can be seen that after also eliminating the electrophoretic and drag forces, the remaining forces acting on the particle are due only to the driving pressure and the electrokinetic body force due to the electric field. This force, F_e , considered the most important in creating the instabilities seen in the experiment [25], is given by equation (13) which can be simplified

$$\vec{F}_e = \rho_f \vec{E} - \frac{1}{2}(\vec{E} \cdot \vec{E})\nabla\epsilon + \frac{1}{2}\left[\rho\vec{E} \cdot \vec{E} \left(\frac{\partial\epsilon}{\partial\rho}\right)\right]_T \quad (36)$$

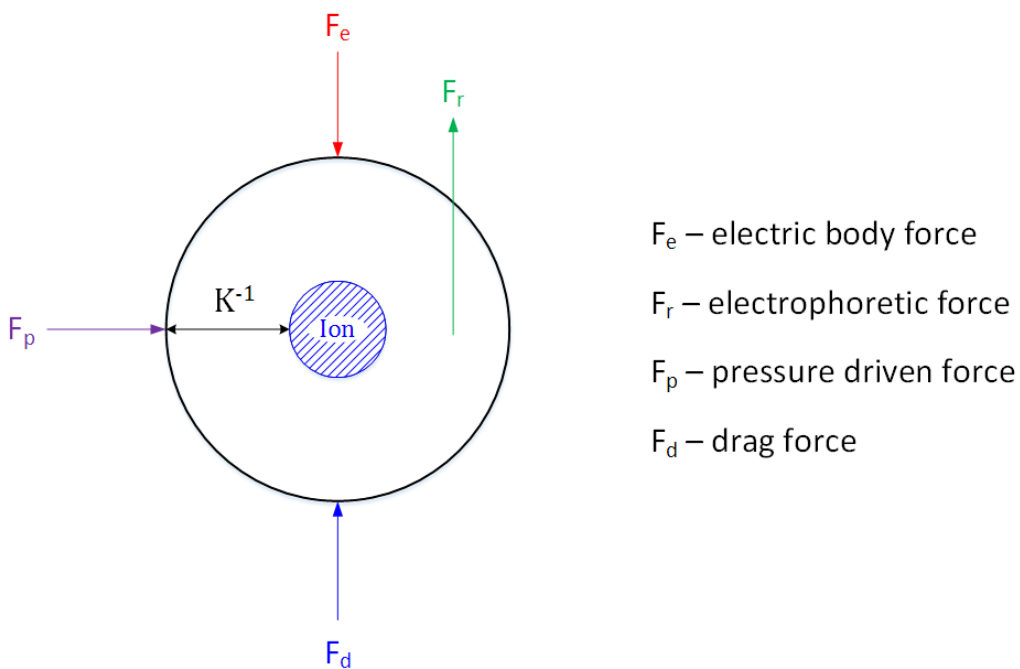


Figure 16: Particle Force Balance

by assuming that the partial derivative term disappears for incompressible fluids and the second term is typically much smaller (and therefore negligible) than the first when two fluids of different conductivities meet [27] leaving only the free charge density term which can then be defined in COMSOL as a “volume force” under the *Laminar Flow* physics interface as

$$F_e = \begin{cases} \text{ec.rhoq} * \text{ec.Ex} * \cos(\text{omega} * t) & x \\ \text{ec.rhoq} * \text{ec.Ey} * \cos(\text{omega} * t) & y \\ \text{ec.rhoq} * \text{ec.Ez} * \cos(\text{omega} * t) & z \end{cases} \quad \text{N/m}^3 \quad (37)$$

where ec.rhoq is the volume charge density and ec.E_i is the component of the electric field in the ith direction.

While the contribution of the ignored forces to the creation of turbulence is considered negligible they are still important to the sustainment of the turbulence and to species transport [25].

Figure 17 is an example of manually coupling physics interfaces in COMSOL; specifically it shows the *Laminar Flow* loosely coupled to the *Electric Currents*. Because the volume force is not calculated by the *Electric Currents* interface it cannot be automatically coupled. Here the stationary study step solves for the electric field which is then passed to, and used by, the *Laminar Flow* interface to calculate the body force at each point in the flow at any given time t .

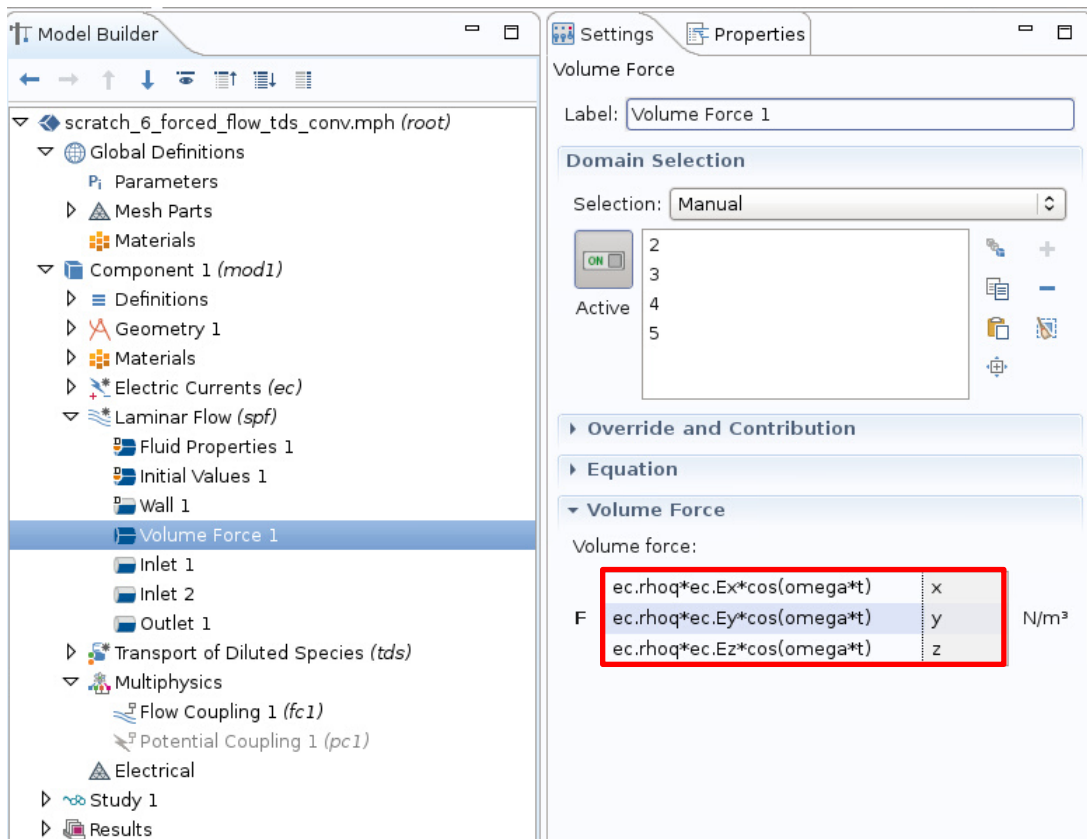


Figure 17: Manual Physics Coupling

Entropy

Why study the entropy of a system?

“...the Second Law is the basis for much of the engineering motive for formulating and solving convection problems. For example, in the development of know-how for the heat-exchanger industry, we strive for improved thermal contact and reduced pump power loss in order to improve the thermodynamic efficiency.” [3]

When comparing two different physical processes it is necessary to find a common relationship between them to base the comparison on. For example, when measuring the effectiveness of a heat transfer process, it is accepted practice to look at the Nusselt number Nu as a performance gauge [7]. For internal flow one looks at the pressure differential to determine system losses, this is good for comparing the efficiency of a design as it relates to frictional flow loss. However, if the system involves heat transfer as well, the temperature differential is used to quantify thermal losses. Pressure drop is measured in Pascals while temperature gradients are measured in degrees (Kelvin, Celsius or Fahrenheit), two units that do not add together for the purpose of determining a total system loss without first converting to some unit-less expression.

To describe the total system losses requires all involved expressions to be comparable in terms of units and order which is where the study of entropy really starts to make sense. Entropy ($[W/K \cdot m^3]$) can be calculated from the incompatible variables of each process (fluid flow, heat transfer, species diffusion etc.) typically in post processing when using finite element software. Once a single equation of similar terms is expressed, cause-effect relationships can be more readily seen.

The entropy generation (S_{gen}) equation is

$$S_{gen} = \frac{\partial S_{cv}}{\partial t} - \sum \frac{q_i}{T_i} - \sum_{in} \dot{m}S + \sum_{out} \dot{m}S \geq \emptyset \quad (38)$$

Entropy generation must always be greater than or equal to zero, and the strength of this inequality determines the irreversibility of the process [3]. The energy lost due to these irreversibilities is [3]

$$W_{lost} = T_0 * S_{gen} \quad (39)$$

The entropy generation rate per unit volume due to finite-temperature gradients is [3]

$$S'''_{gen} = \frac{k}{T^2} \left[\left(\frac{\partial T}{\partial x} \right)^2 + \left(\frac{\partial T}{\partial y} \right)^2 + \left(\frac{\partial T}{\partial z} \right)^2 \right] \geq \emptyset \quad (40)$$

where k is the thermal conductivity of the fluid and T is the absolute temperature while the entropy generation due to viscous dissipation is [3]

$$S'''_{gen} = \frac{\mu}{T} \left\{ \begin{array}{l} 2 \left[\left(\frac{\partial u}{\partial x} \right)^2 + \left(\frac{\partial v}{\partial y} \right)^2 + \left(\frac{\partial w}{\partial z} \right)^2 \right] \\ + \left(\frac{\partial u}{\partial y} + \frac{\partial v}{\partial x} \right)^2 + \left(\frac{\partial u}{\partial z} + \frac{\partial w}{\partial x} \right)^2 + \left(\frac{\partial v}{\partial z} + \frac{\partial w}{\partial y} \right)^2 \end{array} \right\} \geq \emptyset \quad (41)$$

For laminar flow (in the x-direction) equation (41) simplifies to

$$S'''_{gen} = 2 \frac{\mu}{T} \left(\frac{\partial u}{\partial x} \right)^2 \geq \emptyset \quad (42)$$

Because the flow in the context of this thesis is 3-dimensional, this simplification is NOT made.

To measure the total entropy in the simulated system the entropy generation equation must also include the entropy generated from concentration gradients due to diffusion of species [9]

$$S'''_{gen} = \frac{RD}{c} \left[\left(\frac{\partial C}{\partial x} \right)^2 + \left(\frac{\partial C}{\partial y} \right)^2 + \left(\frac{\partial C}{\partial z} \right)^2 \right] + \frac{RD_e}{T} \left[\left(\frac{\partial T}{\partial x} \right) \left(\frac{\partial C}{\partial x} \right) + \left(\frac{\partial T}{\partial y} \right) \left(\frac{\partial C}{\partial y} \right) + \left(\frac{\partial T}{\partial z} \right) \left(\frac{\partial C}{\partial z} \right) \right] \geq \emptyset \quad (43)$$

Where C is the concentration, De is the diffusion coefficient, and R is the gas constant (8.314 J/K-mol). Because this thesis is assuming isothermal conditions equation (40) in its entirety and the second term of equation (43) can be neglected making the overall entropy generation equation

$$S'''_{gen} = \frac{\mu}{T} \left\{ \begin{array}{l} 2 \left[\left(\frac{\partial u}{\partial x} \right)^2 + \left(\frac{\partial v}{\partial y} \right)^2 + \left(\frac{\partial w}{\partial z} \right)^2 \right] \\ + \left(\frac{\partial u}{\partial y} + \frac{\partial v}{\partial x} \right)^2 + \left(\frac{\partial u}{\partial z} + \frac{\partial w}{\partial x} \right)^2 + \left(\frac{\partial v}{\partial z} + \frac{\partial w}{\partial y} \right)^2 \end{array} \right\} + \frac{RD}{c} \left[\left(\frac{\partial C}{\partial x} \right)^2 + \left(\frac{\partial C}{\partial y} \right)^2 + \left(\frac{\partial C}{\partial z} \right)^2 \right] \geq \emptyset \quad (44)$$

Obviously, this simplification would not be made if heat transfer were added as a parameter of this study in the future. The units of entropy generation per unit volume are $\frac{W}{m^3 \cdot K}$ [8] for equations (40)-(44) no matter which physics is involved (electrical, flow, or species transport).

Mesh Study

To get accurate results in a finite element analysis, a mesh convergence study is used to determine the mesh size needed to balance the computational cost with the desired solution accuracy. A laminar flow simulation was completed for 4 meshes of increasing resolution (Coarser, Coarse, Normal and Fine) at a forcing voltage of 20V_{pp}.

Typically a mesh study is done by looking at the simulation results for parameters that are of interest to the researcher. In this case many of the parameters of interest are derived from

velocity but velocity is difficult to compare volumetric totals when flow is moving in both the positive and negative stream-wise directions. This mesh study looked at the total values for T_e and S_{gen} over the volume shown in [Figure 27](#) at each mesh size. Because the differences are on the order of 10^{-11} for each mesh it shows that the choice of mesh in this case is arbitrary as the velocities involved are on the order of 10^{-3} , the values of T_e are on the order of 10^{-6} and the values of S_{gen} at the channel entrance is as high as 200. For this reason the Coarse Mesh (see [Figure 20](#) & [Figure 21](#)) was used as it was the best choice with regards to solution time with each voltage run taking approximately 1hr 22min with *Transport of Diluted Species* included. For comparison, *without* TDS, a simple forced flow simulation with a *Normal* mesh resolution took 1hr 47min and the *Fine* resolution took 2hrs 33min.

The elements making up the meshes included tetrahedral, pyramid, prism, triangular, quadrilateral, edge and vertex elements. Plots of the individual mesh plots of T_e , additional mesh images and statistics for all four meshes can be found in [APPENDIX B, Figure 18 \(b\) - Figure 66](#).

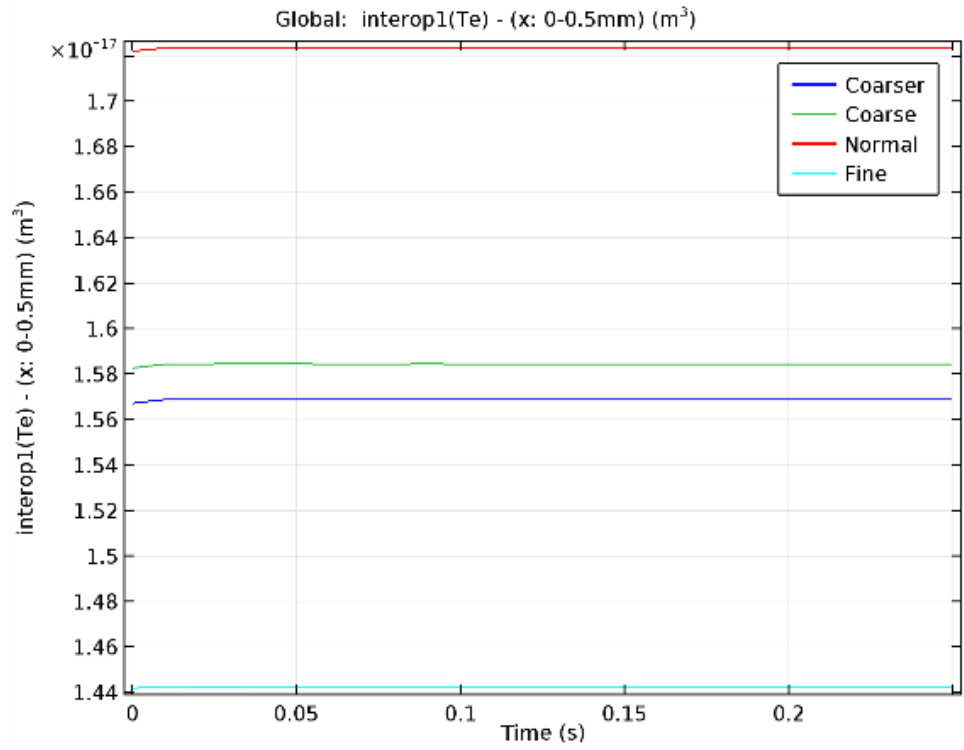


Figure 18(a): Comparison of total Te values for different mesh resolutions (Total Te integrated over volume from trailing edge to 0.5mm)

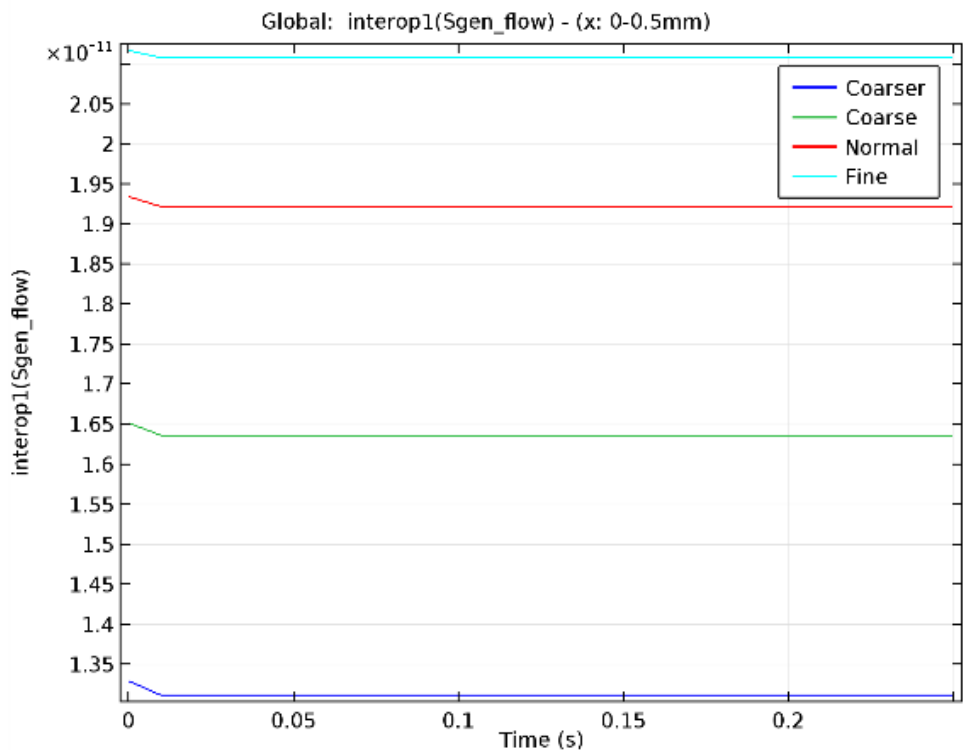


Figure 19: Comparison of total Entropy values for different mesh resolutions (Total Entropy integrated over volume from trailing edge to 0.5mm)

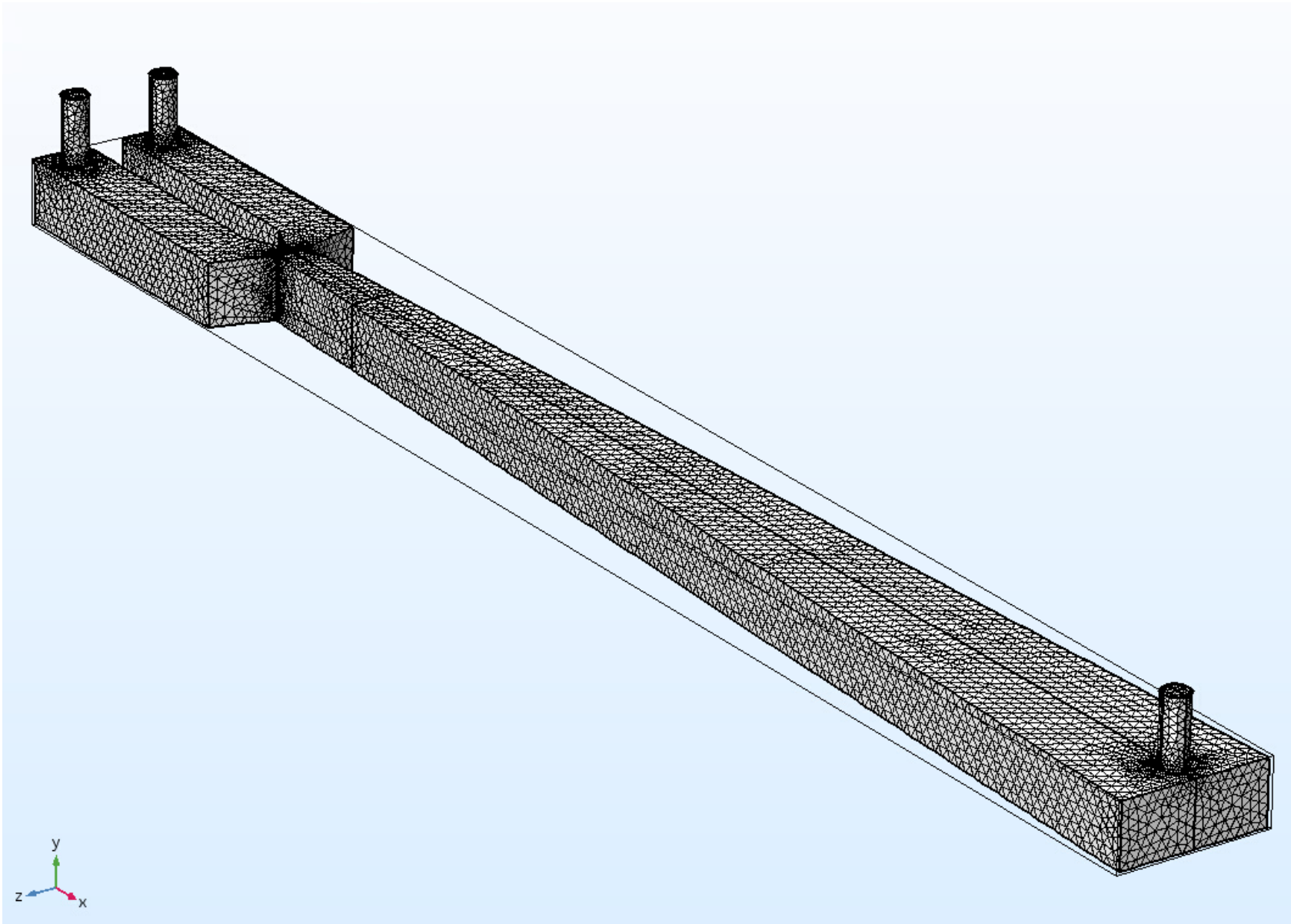


Figure 20: Coarse Mesh

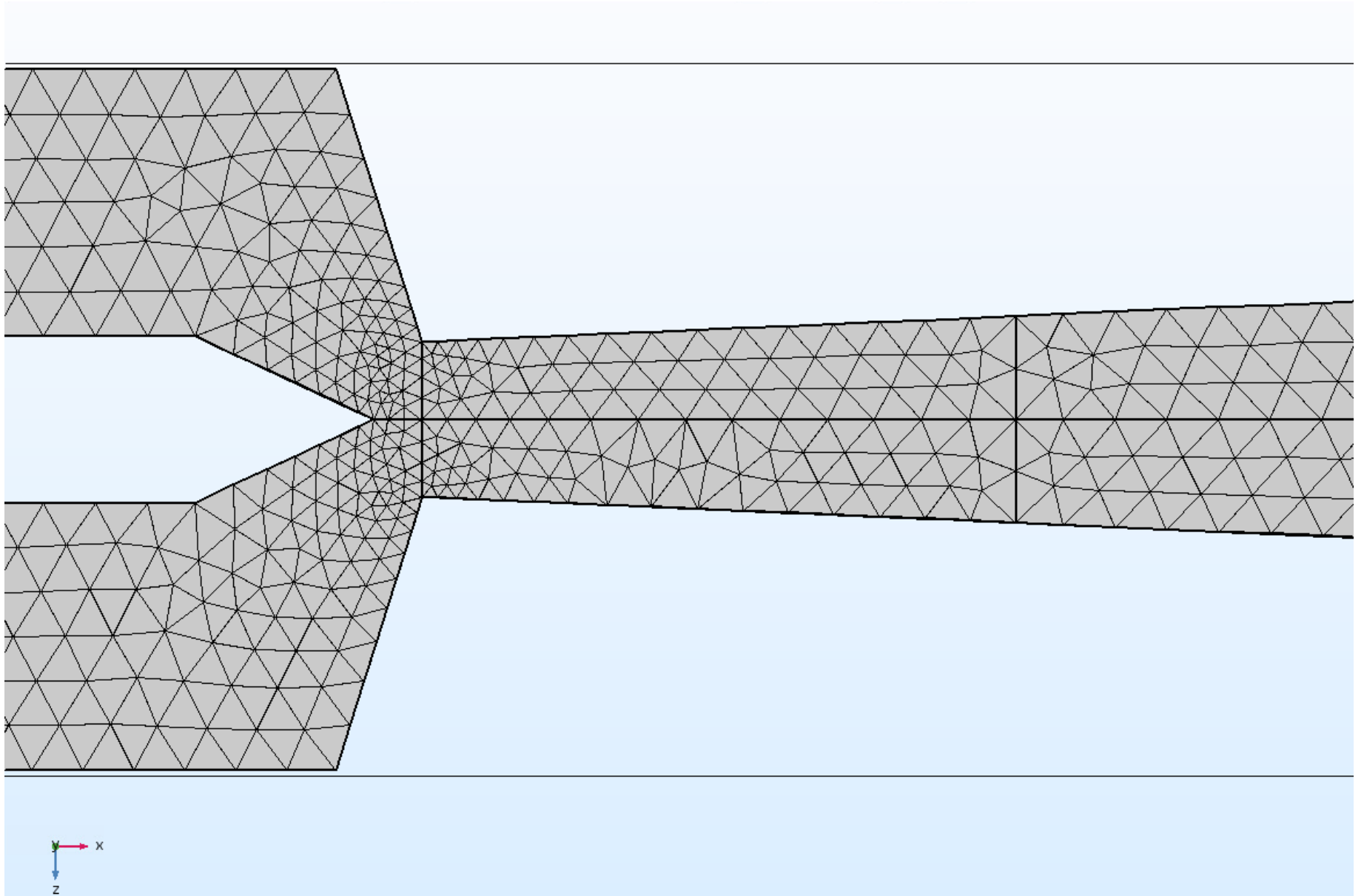


Figure 21: Coarse Mesh (in channel)

PAGE LEFT INTENTIONALLY BLANK

CHAPTER IV: RESULTS

The simulation results from this thesis yielded results that agree with the experimental results within the same order of magnitude. Identical simulations were run for a sweep of voltages from 0-20Vpp at specific data collection points (Figure 22 thru Figure 26) necessary to compare the data to the Wang et al. paper.

Points of Interest

The primary point for data collection was at (100, 0, 0) shown in Figure 22; this is the point at which T_e , Ra_e and u_s were calculated for the plots presented in this chapter. Although the simulations were done using *Laminar Flow and Transport of Diluted Species* (TDS), the TDS component serves only to illustrate the effects of the flow on the diffusion of the conductive solution and to calculate diffusion based entropy; it is not bi-directionally coupled to the flow.

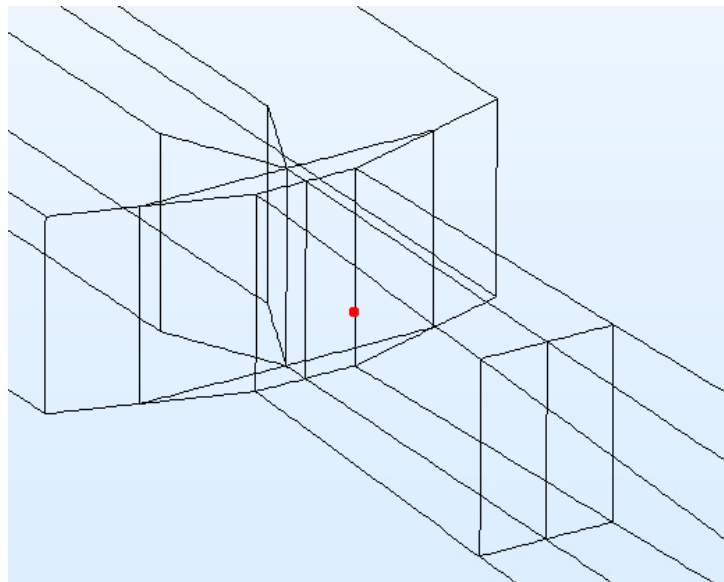


Figure 22: Point at (100, 0, 0) μm

The lines spanning the z-axis transversely to the flow (from one electrode to the other) at $y = 0\mu\text{m}$ for $x = 0\mu\text{m}$ & $x = 100\mu\text{m}$, are the lines along which the mean velocity, u_s , was calculated and then plotted versus time.

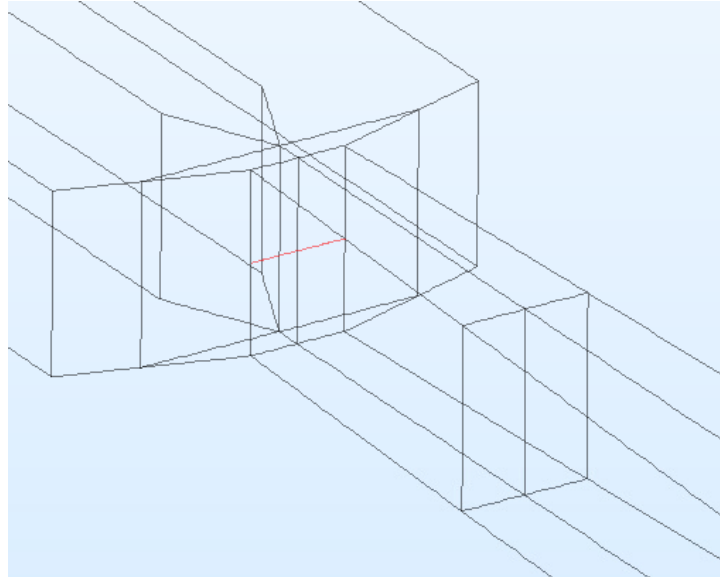


Figure 23: Transverse line at $x = 0\mu\text{m}$

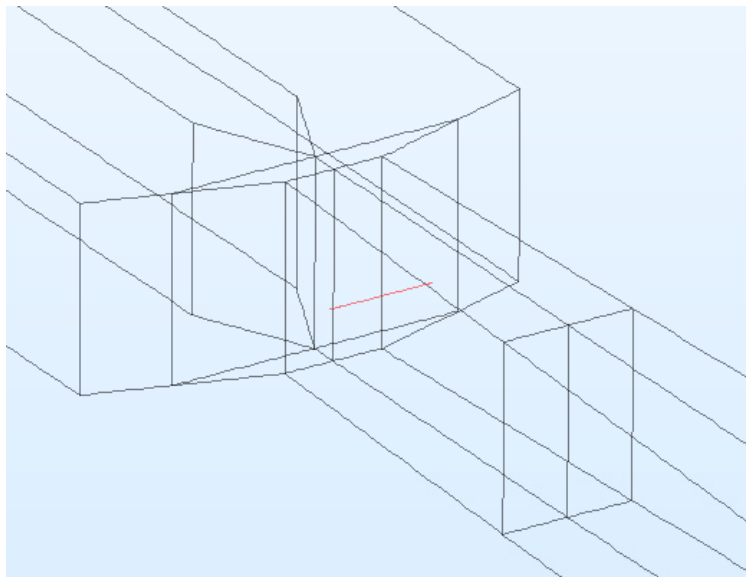


Figure 24: Transverse line at $x = 100\mu\text{m}$

The lines spanning the z-axis transversely to the flow (from one electrode to the other) at $x = 100\mu\text{m}$ for $y = 0\mu\text{m}$ & $y = (-100)\mu\text{m}$, are the lines along which T_e was calculated and then plotted versus the position z from $\pm 35\mu\text{m}$.

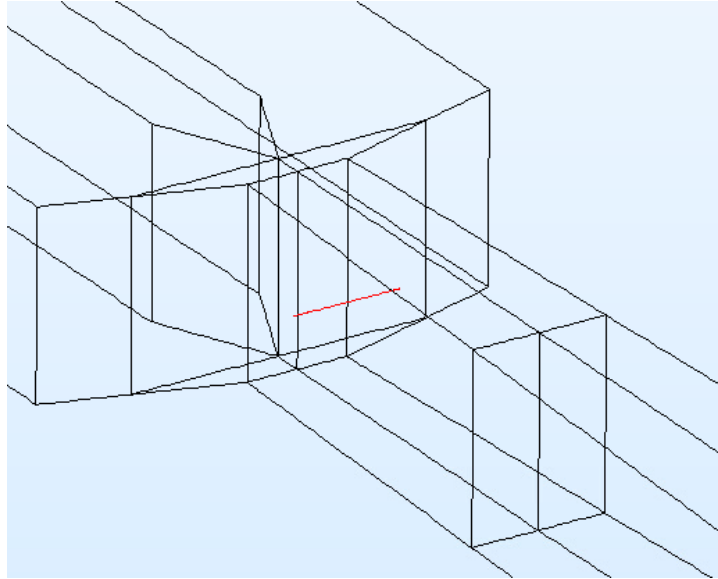


Figure 25: Transverse line at $x = 100\mu\text{m}$, $y = 0\mu\text{m}$

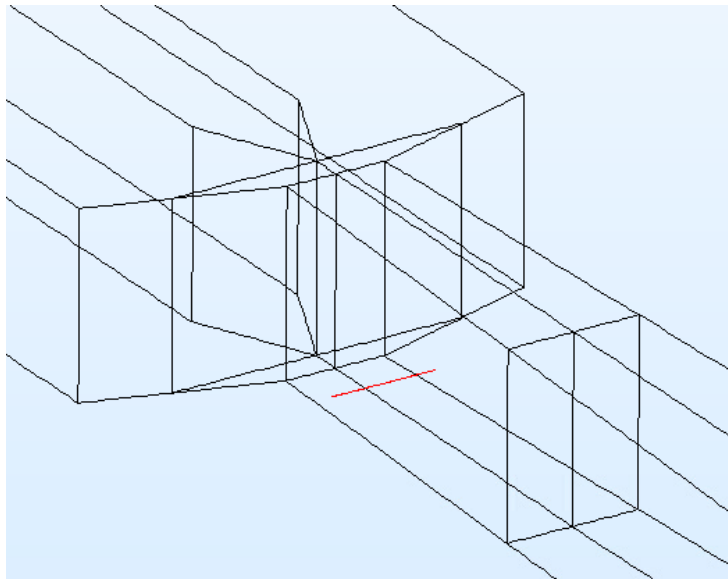


Figure 26: Transverse line at $x = 100\mu\text{m}$, $y = (-100)\mu\text{m}$

The volume shown in [Figure 27](#) covers the geometry from the trailing edge of the separating plate to the entrance of the channel and from the entrance to the plane $x = 0.5\text{mm}$. The volume between the trailing edge and the channel entrance includes the region with the largest concentration gradient ($\Delta\sigma \sim 5000:1$) and charge density; the complete volume was used to calculate the total entropy generated.

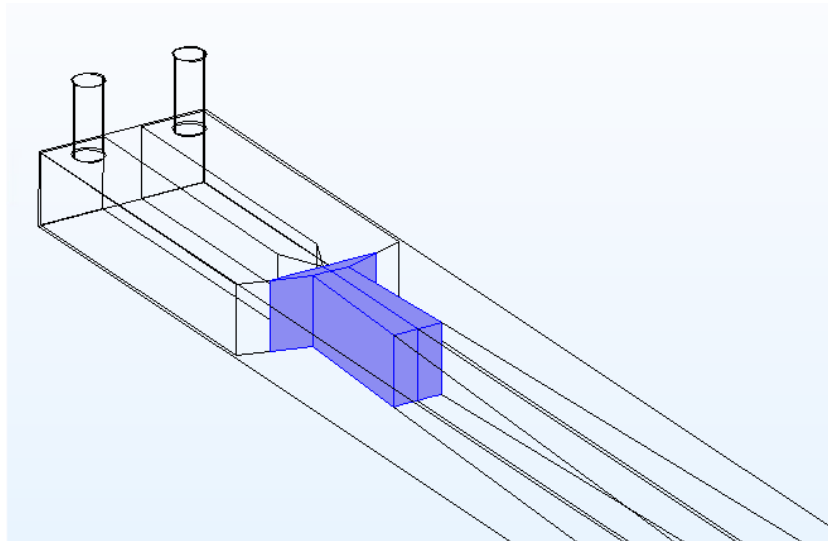


Figure 27: Volume from trailing edge to $x = 0.5\text{mm}$

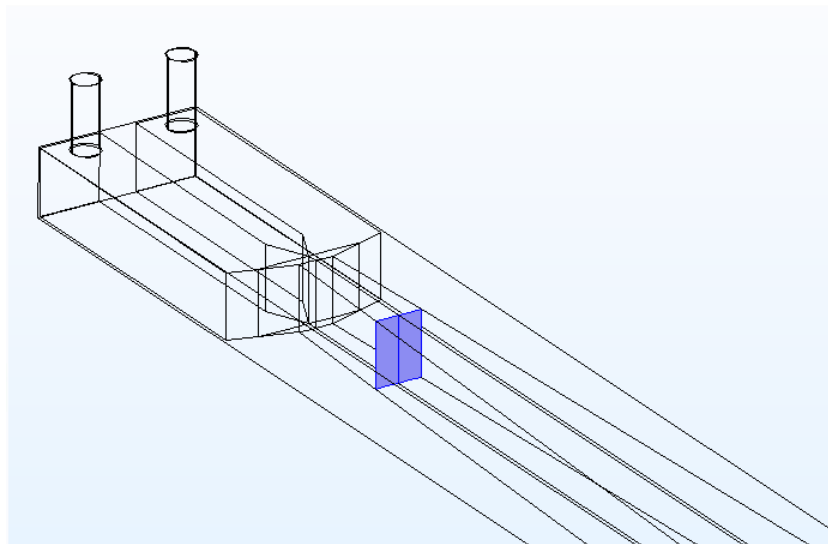


Figure 28: Flow rate through surface $x = 100\mu\text{m}$

The plane in [Figure 28](#) is the end surface of the volume highlighted in [Figure 27](#) and was used to calculate the average flow rate of $6.50 \times 10^{-11} \text{ m}^3/\text{s}$ through the volume (see [Table 8](#) for comparison).

Table 8: Flowrate

$$(Q_{0.5\text{mm}} = \text{spf.out1.Mflow}/\text{spf.rho} \text{ (m}^3/\text{s)})$$

	Q_{0.5mm} at 0V_{pp}	Q_{0.5mm} at 8V_{pp}	Q_{0.5mm} at 20V_{pp}
Thesis Results	6.5005E-11	6.5030E-11	6.5030E-11
Theoretical	6.66E-11	6.66E-11	6.66E-11

In Wang et al., the experimental results are discussed as they relate to the previously mentioned six indicators of turbulent flow [26]: fast diffusion, high dissipation, irregularity, multi-scale eddies, continuity and 3-D flow. Of these six parameters, this thesis will present results correlated to four: fast diffusion, high dissipation, irregularity and 3-D flow.

The non-parallel electrodes are closest at the channel entrance, the electric field is strongest there and the interaction between the electric field and the conductivity gradient which, from equation (14), can be seen to create the maximum value for the charge density. The effect of transverse electric fields on conductivity gradients have been studied by Storey et al. [45] and Lin et al. [46]. From the definition for the body force (equation (37)) in Navier-Stokes, the maximum body force will be in the same area as the maximum free charge density; see [Figure 29](#) and [Figure 30](#). This result concurs with that of Wang et al. [27].

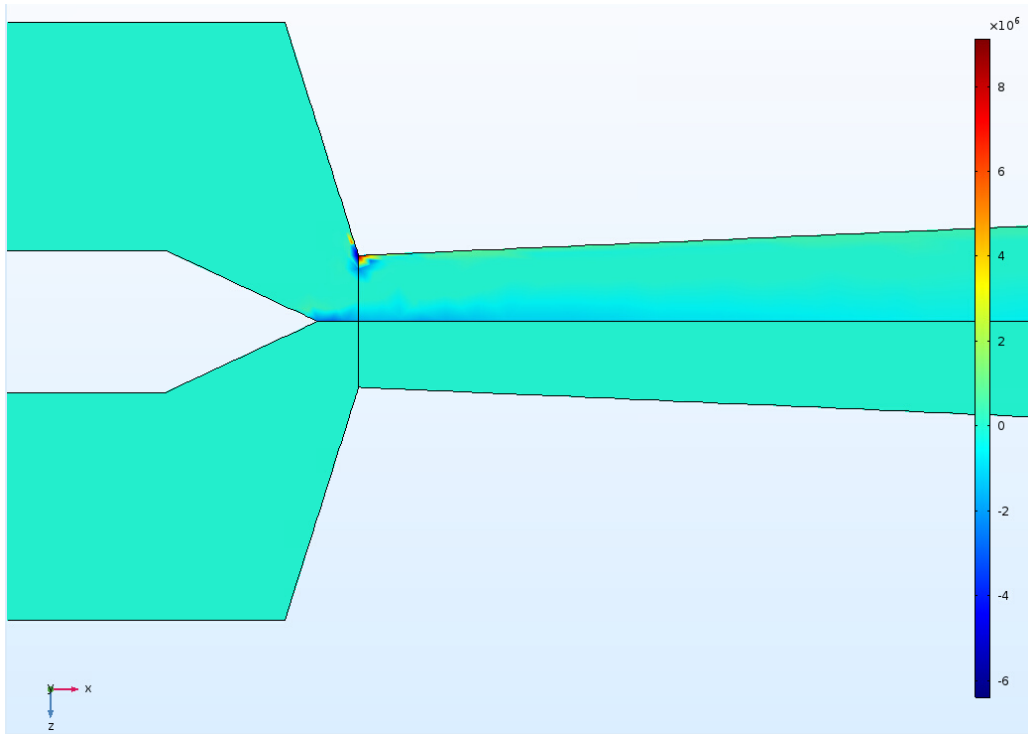


Figure 29: Body Force (N/m^3)
 $(\epsilon_c \cdot \rho_{hoq} \cdot \epsilon_c \cdot E_z \cdot \cos(\omega t))$ at $t=0.25\text{s}$

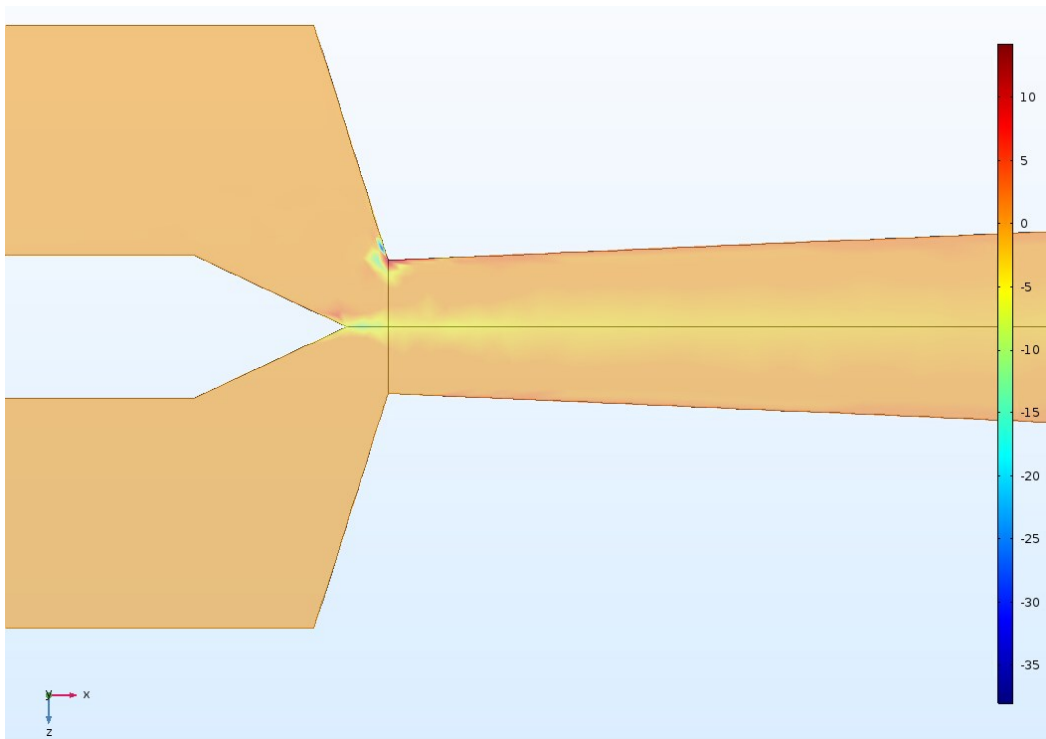


Figure 30: Space Charge Density (C/m^3)
 $(\epsilon_c \cdot \rho_{hoq})$ at $t=0.25\text{s}$

Features of Turbulence

The simulations in this thesis were completed using a *Laminar Flow* study instead of *Turbulent Flow* study. When using turbulent models, one of the dependent variables calculated by COMSOL is the turbulent energy (T_e) which is a parameter used by Wang et al. to verify the results of their experiments were indeed turbulent. All the figures presented are at $t = 0.25s$.

Fast Diffusion

From [Figure 31](#) it can be seen that, without forcing, the flow is completely laminar and becomes more turbulent in appearance as the forcing voltage increases. While comparing the simulation stream lines to the LIFPA images of diffusion in the Wang experiment is not completely analogous, the experiment's visualization images using polystyrene particles as tracing devices shows similar results to the streamlines in [Figure 32](#) and [Figure 33](#).

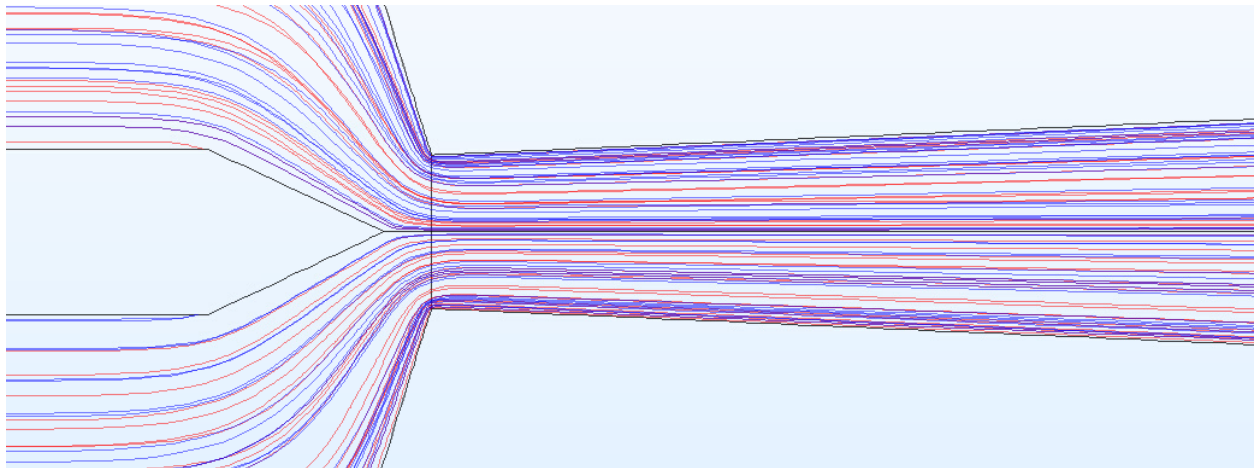


Figure 31: Streamlines - 0Vpp (unforced)

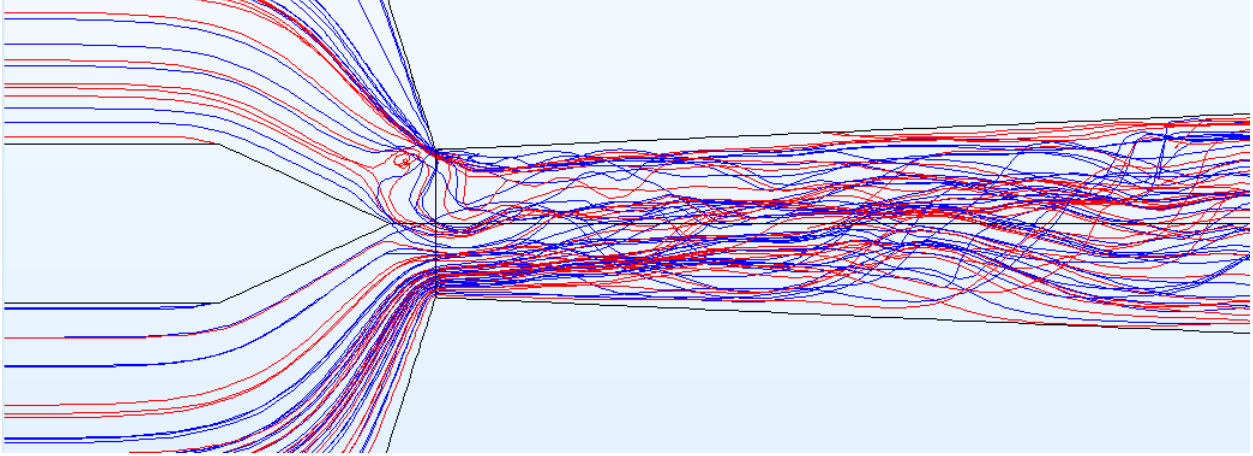


Figure 32: Streamlines - 8Vpp

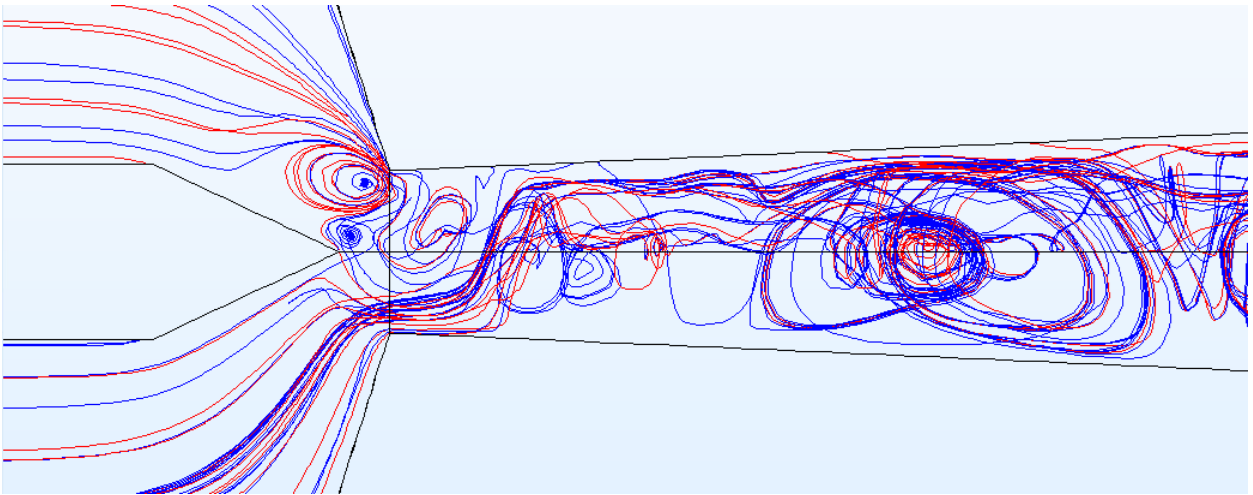


Figure 33: Streamlines - 20Vpp

The increase in dissipation due to increasing the electric field can also be seen in [Figure 34](#) through [Figure 36](#). Slices shown are $x = 0, 100, 200, 300, 400, \& 500\mu\text{m}$. At a forcing voltage of $20V_{pp}$ the mixture appears to be completely homogenous at the plane $x = 0.5\text{mm}$. Because the two fluid domains are discretely populated at $t = 0\text{s}$ with fluids of concentrations shown in the inlets, [Figure 37](#) shows that homogeneity disappears shortly after this plane but it can be assumed that if the simulation was continued past 0.25s , the entire channel would become completely mixed due to the developing secondary flows that can be clearly seen downstream. See [APPENDIX B](#) for figures that illustrate the progression of streamline disruption as voltage increases.

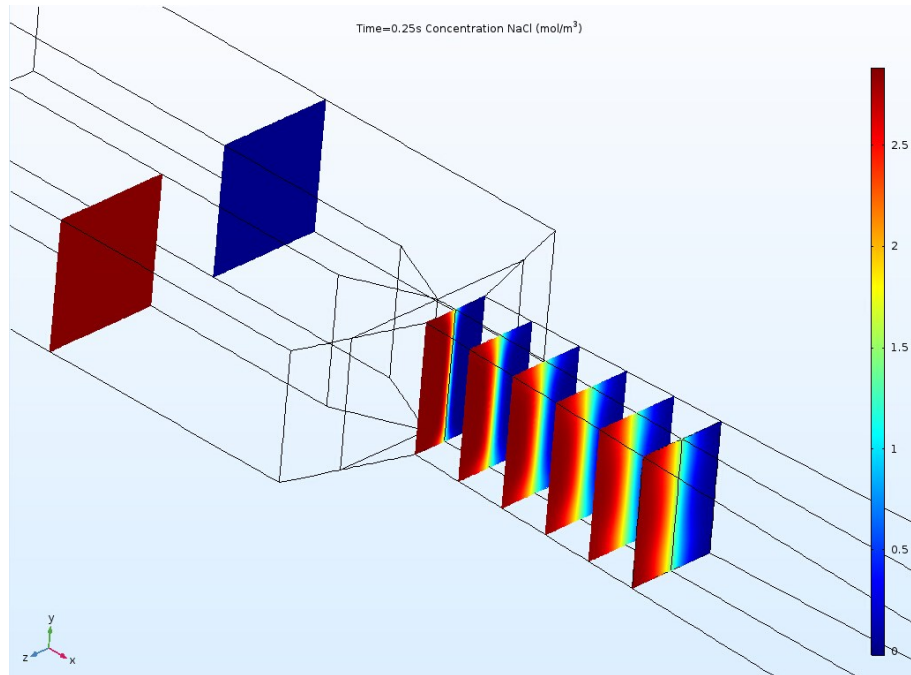


Figure 34: NaCl Concentration Slices (mol/m³) - 0Vpp (unforced)

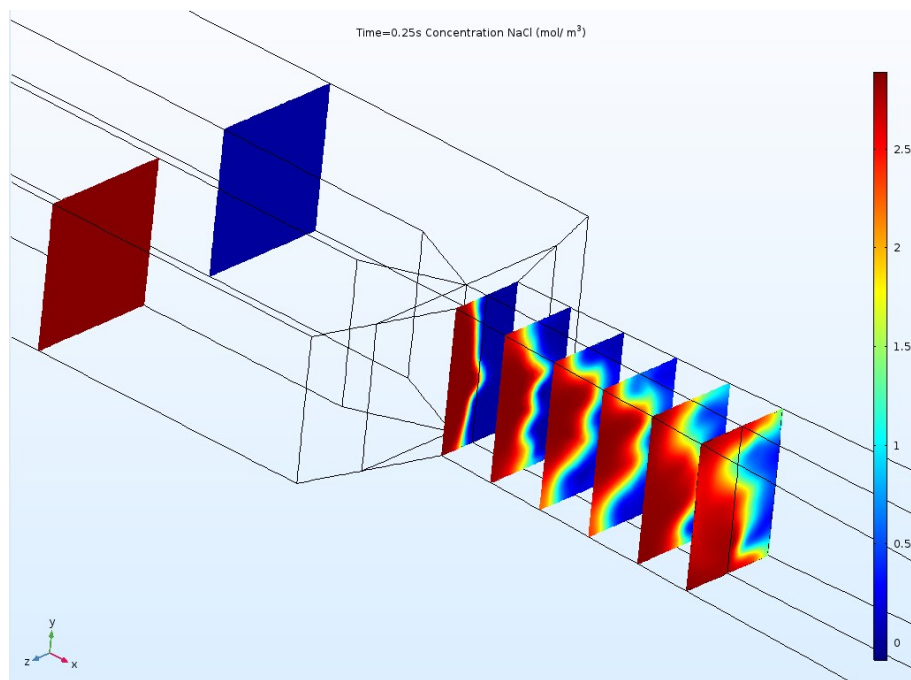


Figure 35: NaCl Concentration Slices (mol/m³) - 8Vpp

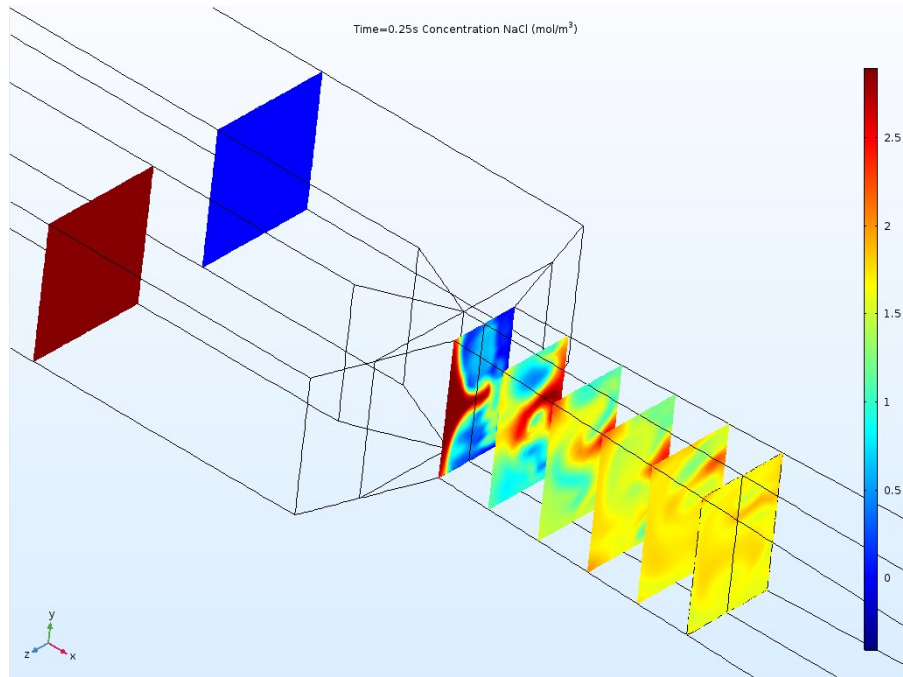


Figure 36: NaCl Concentration Slices (mol/m³) - 20Vpp

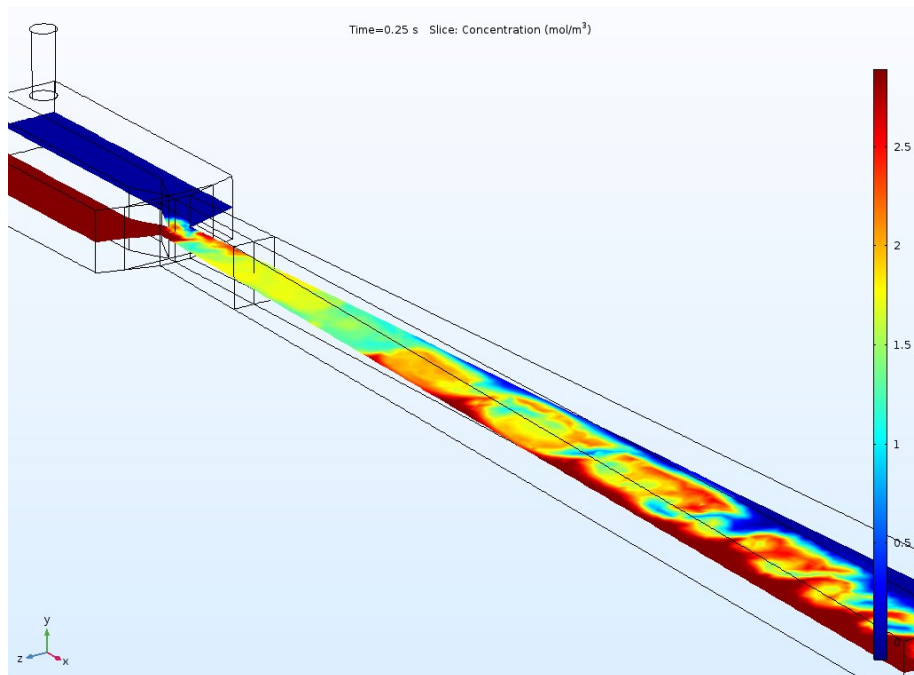


Figure 37: Downstream NaCl concentration (mol/m³) - 20Vpp

High Dissipation

In macro-flows, a rapid, non-linear increase in the turbulent dissipation (another way of denoting pressure drop) signals the release of turbulent energy [26] so if the dissipation rate is high then the rate of change of turbulent energy is also high, indicating turbulence. The turbulent energy, T_e , was calculated at the point (100, 0, 0), Figure 22, see also Detail A in Figure 6 for x-coordinate reference. The voltage range for the data points in Figure 38 thru Figure 40 are for the voltage range 2-20V_{pp} (from left to right); 0V_{pp} yields an undefined Electric Rayleigh number (Ra_e), equation (49), and cannot be plotted.

Wang et al. calculated the turbulent energy using

$$T_e = \langle u_s'^2 \rangle \quad (45)$$

where

$$u_s' = u_s - \langle u_s \rangle \quad (46)$$

and

$$u_s = \sqrt{u^2 + v^2 + w^2} \quad (47)$$

An alternate, expanded form given uses a factor of one-half [33]

$$T_e = \frac{1}{2} \left(\overline{u_x'^2} + \overline{u_y'^2} + \overline{u_z'^2} \right) \quad (48)$$

The Electric Rayleigh number is defined as [26]

$$Ra_e = \frac{\varepsilon w^2 E_0^2 (\sigma_2 - \sigma_1)}{\sigma_1 \mu D_e} \quad (49)$$

where ε is the absolute permittivity given by multiplying the relative permittivity, ε_r , by the vacuum permittivity ε_0 . The channel width at the entrance is w , E_0 is the value of the electric field, σ_2 is the conductivity of the NaCl solution and σ_1 is the conductivity of the distilled water. The diffusivity (or diffusion coefficient) is D_e and the value used in the experimental paper [26] and in this thesis was $1.5 \times 10^{-9} \text{ m}^2/\text{s}$.

The difference between equations (45) and (48) is shown by comparing the y-values of Figure 38 and Figure 39, the biggest difference being the range of turbulent energy.

Unfortunately, COMSOL only calculates this turbulent energy if a flow study is done using the *Turbulent Flow* physics interface so a method of calculating this was devised using a custom equation to depict T_e as

$$T_e = \text{sum}((us - (\text{sum}(us, t, 0, t_end)/25))^2, t, 0, t_end)/25 \quad (50)$$

And Ra_e was calculated using the custom equation

$$Ra_e = ((80.2 * \text{root.} \varepsilon_0 \text{const}) * (2 * (V_0^2)) * (0.0275 - 5.56e - 6))/(5.5e - 6 * 0.001[\text{Pa} * \text{s}] * 1.5e - 9[\text{m}^2/\text{s}]) \quad (51)$$

While Wang et al. used $\langle \quad \rangle$ to denote ensemble averaging this thesis used time averaging which can, in some cases, be considered equivalent [63].

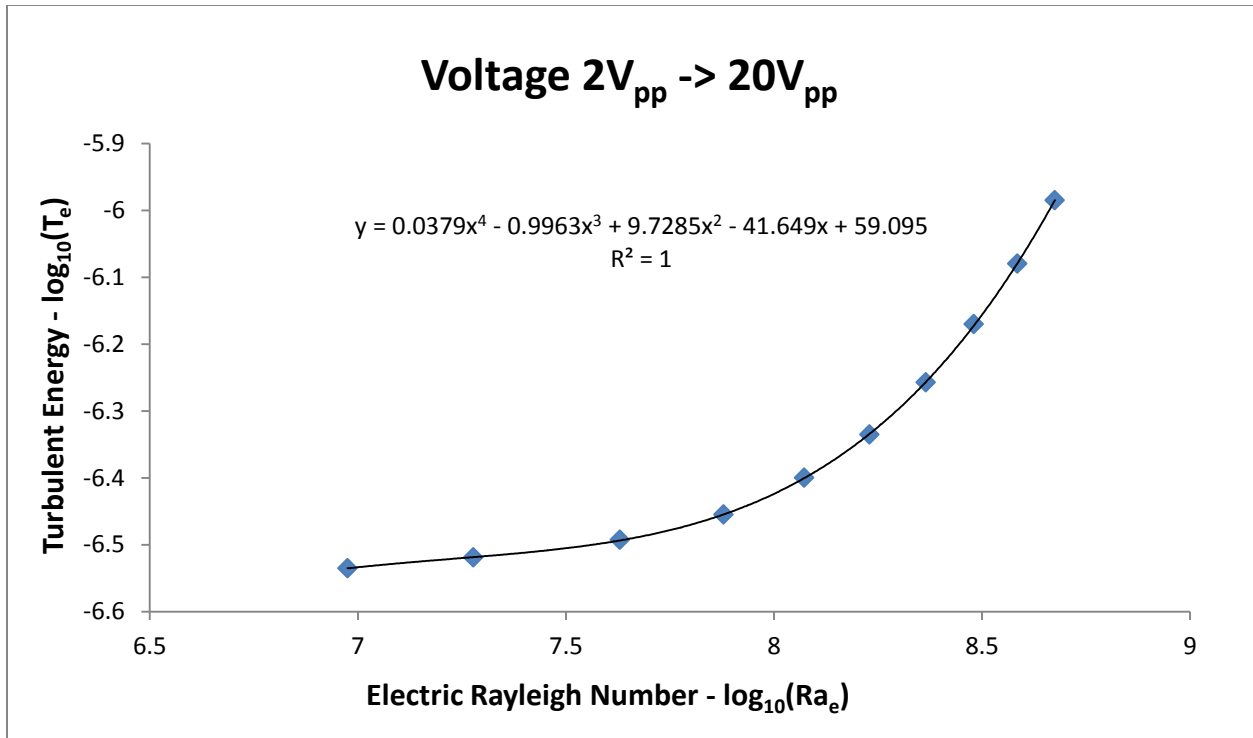


Figure 38: T_e vs Ra_e
(using eq. (48))

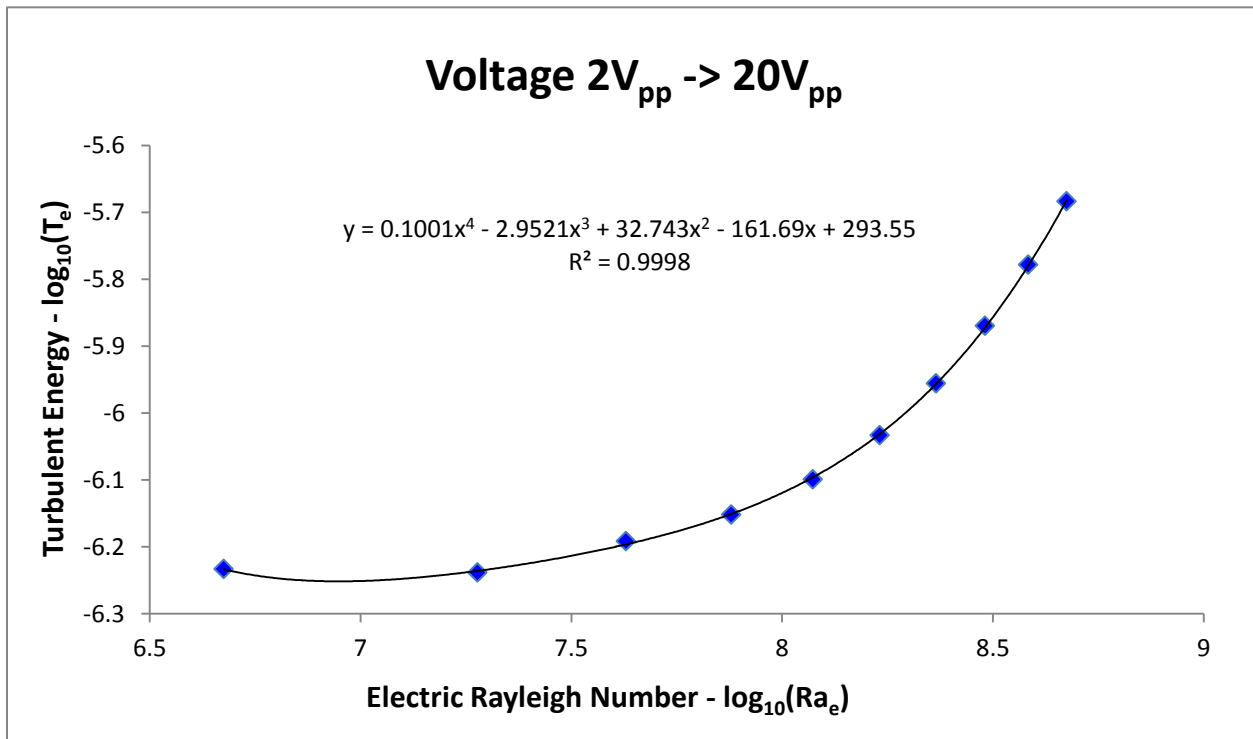


Figure 39: T_e vs Ra_e
(using eq. (45))

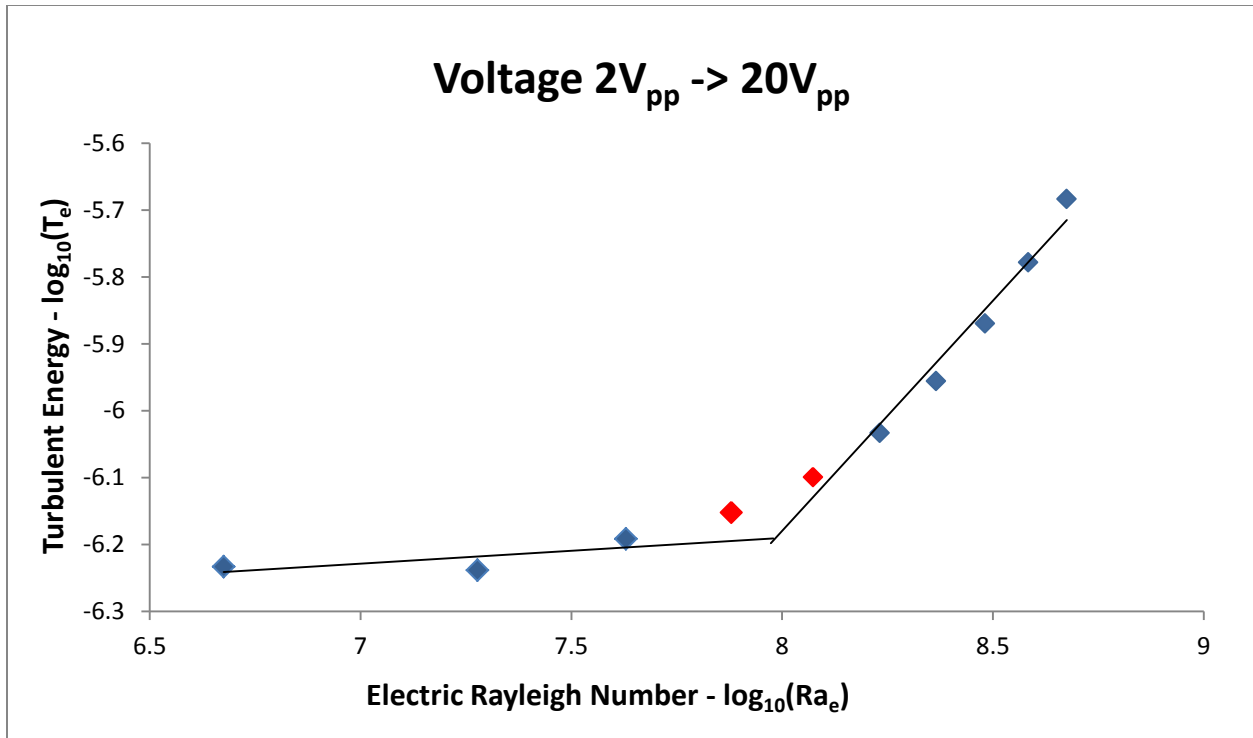


Figure 40: T_e vs Ra_e
(slope increases past the critical Electric Rayleigh number)

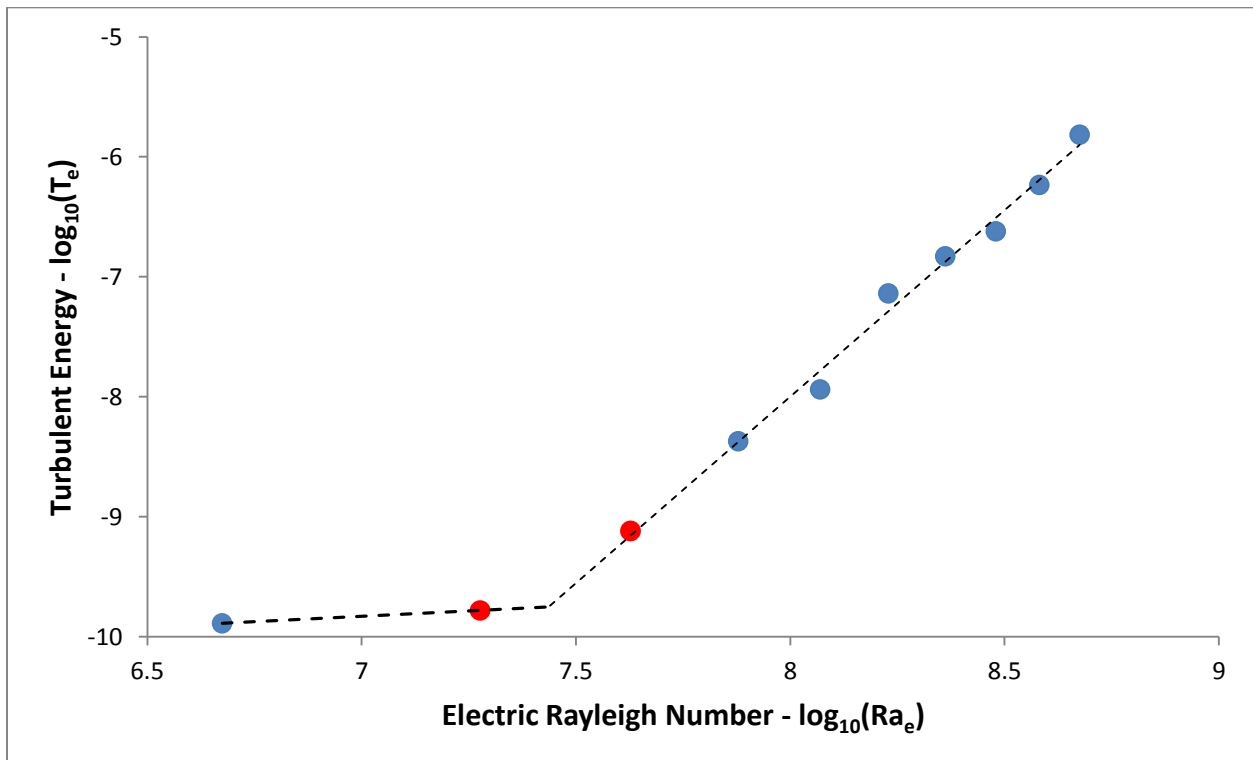


Figure 41: T_e vs Ra_e (Wang et al. experimental data)

Using [Figure 41](#), Wang et al. calculated the critical Rayleigh number which is the point in the plot after which the slope increases much faster (between the points shown in red). Comparisons between the experimental data and that gathered from these simulations of this thesis are in [Table 9](#).

Table 9: T_e vs. Ra_e Result Comparison

	Ra_{ec} (range)	log-log Laminar Slope	log-log Turbulent Slope	Turbulent Slope/ Laminar Slope
Thesis Results	1.18e7 - 7.57e7	0.044	0.690	15.738
Wang Results	1.9e7 - 4.3e7	0.16	3.03	18.938

[Table 9](#) clearly shows that while the slopes are smaller than the experimental values by one order of magnitude, the relationship between the turbulent and laminar slopes (how much greater the turbulent slope is than the laminar) is closer in value, as is the critical Rayleigh number (Ra_{ec}) range discovered from the simulations; both are within the same order of magnitude.

Irregularity

The irregularity feature of turbulence is plotted as a time trace of the velocity at a specific point (see [Figure 22](#)). While fluctuations in the value of u_s became greater as the voltage increased in the experimental paper, the results of this thesis showed relatively constant values over time, [Figure 42](#). However, the mean experimental values are on the same order as those found in these simulations; see [Table 10](#) for a comparison of the experimental-to-thesis values.

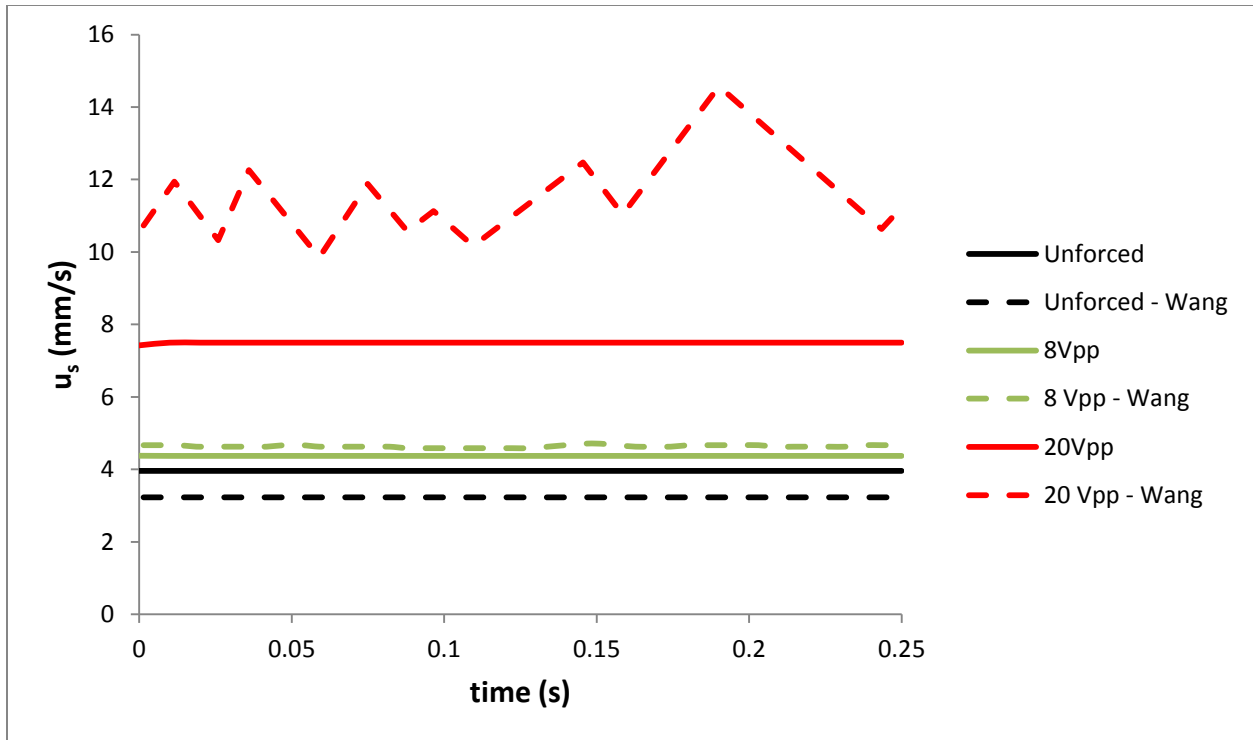


Figure 42: u_s vs time

Table 10: Mean u_s value comparisons
(Wang values approx. from Figure 3 in paper [26])

	u_s at $0V_{pp}$	u_s at $8V_{pp}$	u_s at $20V_{pp}$
Thesis Results	3.96	4.37	7.50
Wang Results over (0.25s)	3.23	4.65	11.29

3-D Flow

With inhomogeneous, 3D flow being a basic feature of turbulence [26], evidence can be found visually by looking to [Figure 33](#), [Figure 43](#) and [Figure 44](#).

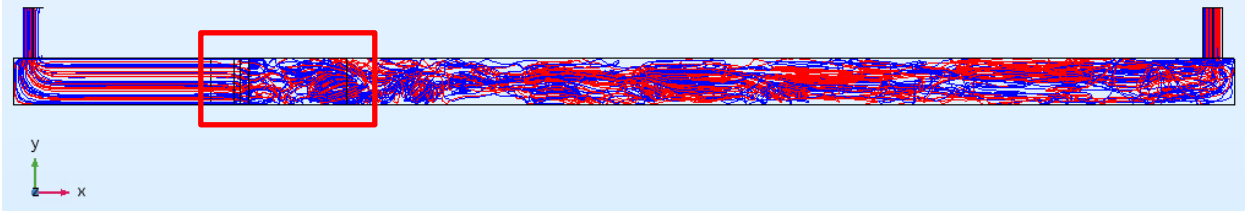


Figure 43: Transverse view of 3D velocity streamlines

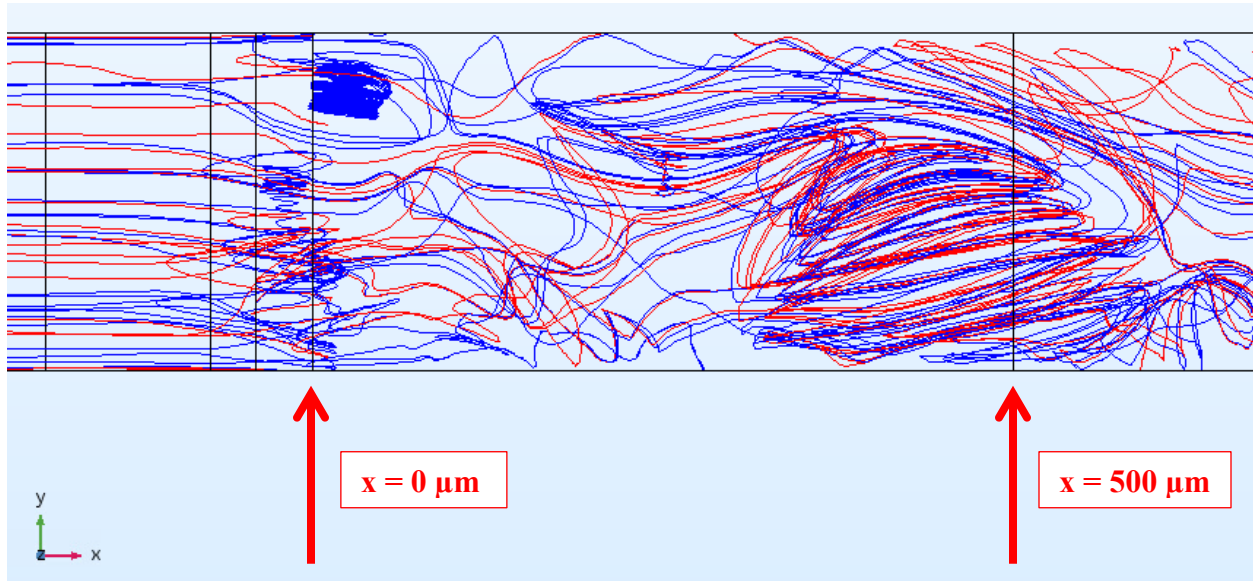


Figure 44: Zoom of Figure 43

or, more analytically, by referring to Figure 45 which shows a similar distribution of T_e along z to the Wang et al. results. It must be noted that the Wang results show unforced values of T_e on the order of 10^{-10} and mean *forced* values of 10^{-7} while this thesis reports values of 10^{-7} and 10^{-6} , respectively.

For a voltage of $20V_{pp}$, the experimental data showed that at $z = 0 \mu\text{m}$ in the y -direction, the value for T_e at $y = 0 \mu\text{m}$ was about 2.7 times larger than the value at $y = -100 \mu\text{m}$ (see Figure 46) which is understandable as the value of T_e is greater towards the centerline of the channel as depicted in Figure 45. The simulation results showed a maximum difference of 1.4 times at $z = -15 \mu\text{m}$.

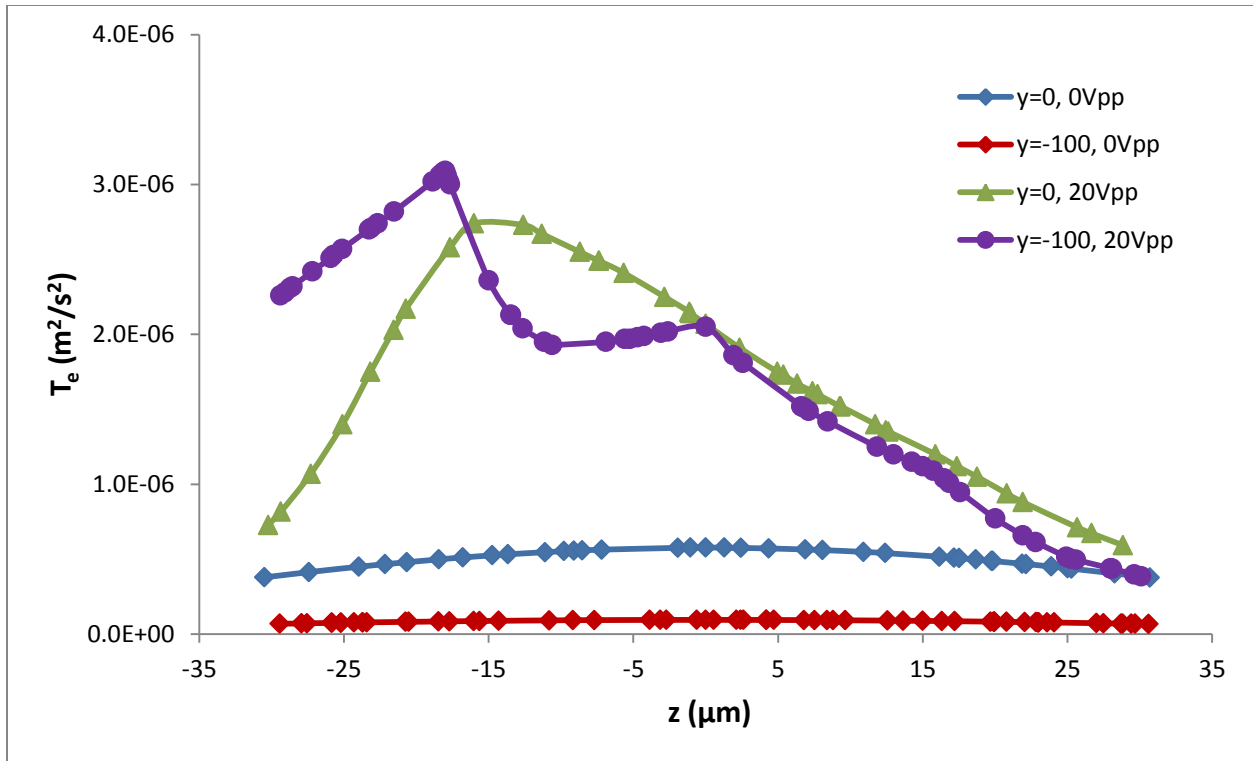


Figure 45: T_e vs z (inhomogeneity of flow in transverse plane)

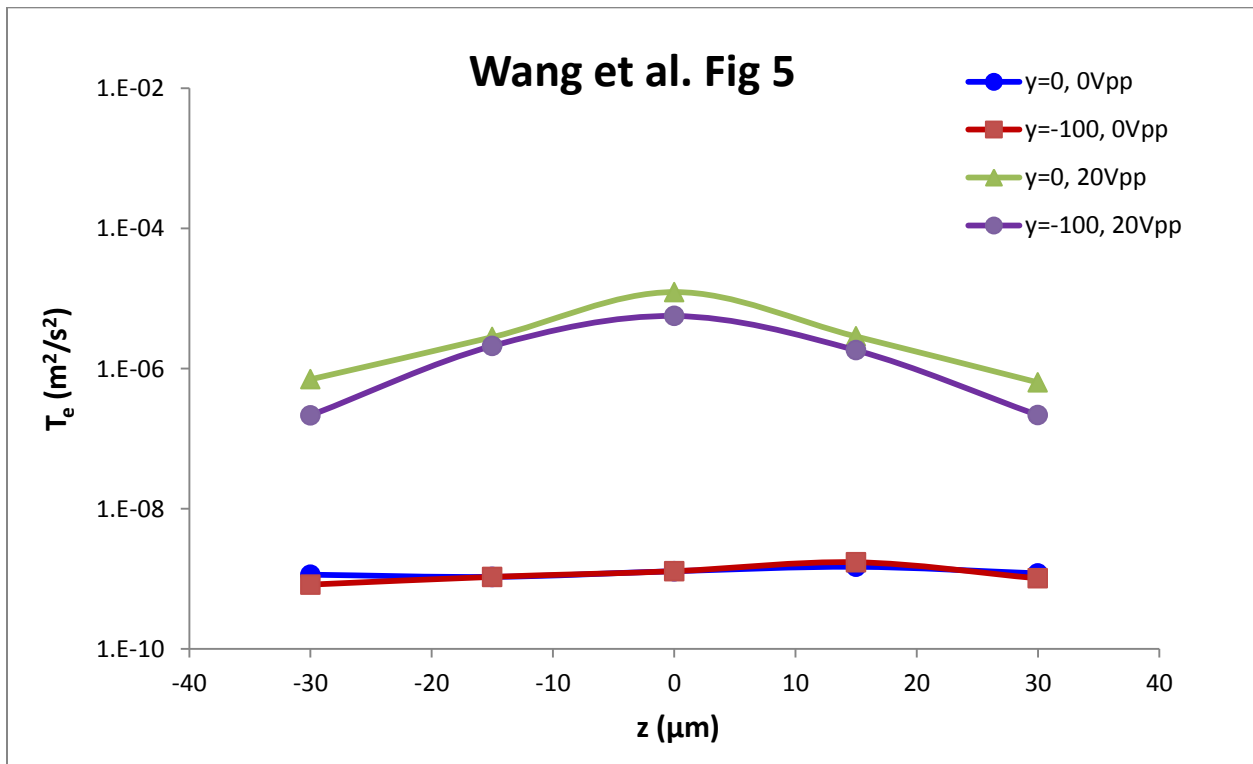


Figure 46: T_e vs z (Wang et al. experimental data)
 (original paper coordinates converted to thesis coordinates using [Table 5](#))

Entropy

The entropy calculated by the simulations in this thesis come from two sources, the flow itself and the transport of the NaCl ions using equations (41) and (43) respectively. Table 11 shows the values for each component of the entropy calculated at time $t = 0.25s$.

Table 11: Entropy components (at $t = 0.25s$)

	S_{gen} at 0V_{pp}	S_{gen} at 8V_{pp}	S_{gen} at 20V_{pp}
Entropy_{flow}	1.65E-13	9.17E-13	2.70E-11
Entropy_{TDS}	2.89E-10	5.27E-10	6.04E-10
Entropy_{total}	2.90E-10	5.28E-10	6.31E-10

Figure 47 shows the entropy generated by the forced flow and Figure 48 shows the entropy generated by the species transport, both at three different forcing voltages. While the transport component contributes the majority of entropy to the system initially (on the order of 10^{-9} compared to 10^{-11}), its contributions diminish over time as the concentration gradient decreases from 5000:1 towards equilibrium at which point the contributions are separated by only a single order of magnitude.

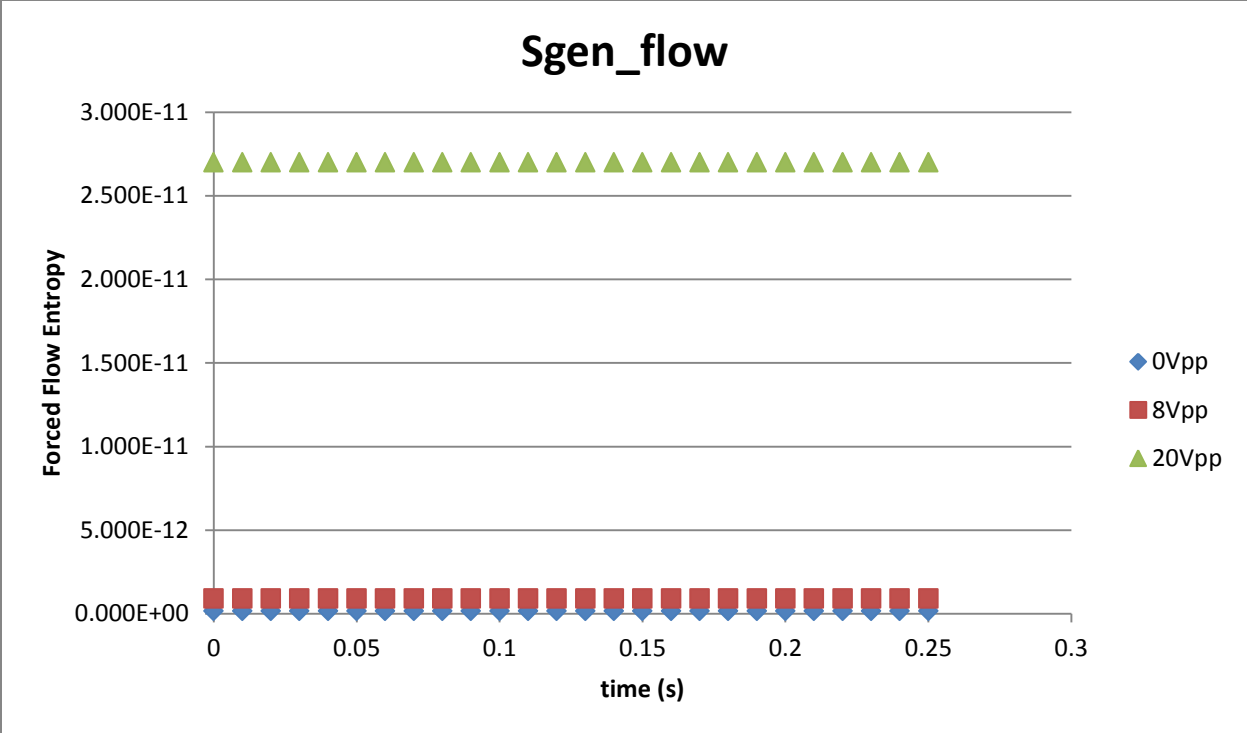


Figure 47: Entropy generated by flow

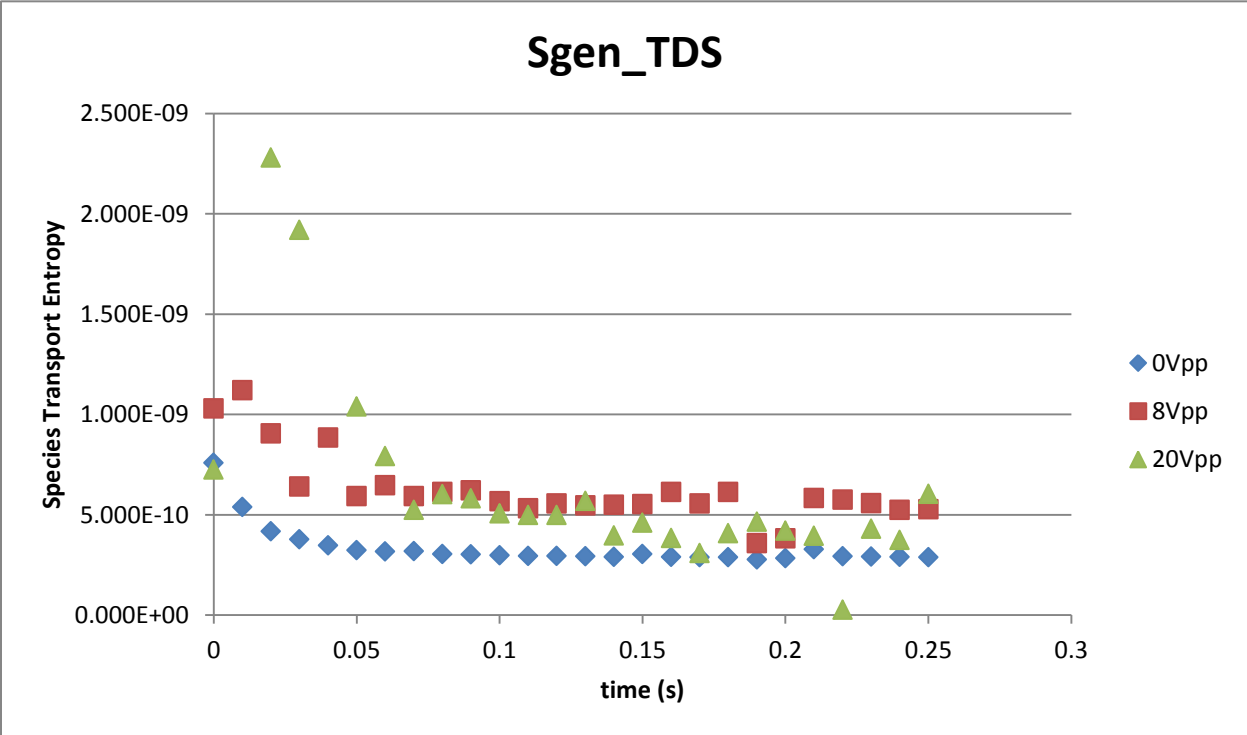


Figure 48: Entropy generated by species transport (ignoring negative values in 20V_{pp})

Alternatively, the entropy generated by the flow has a smaller magnitude but is constant over the length of the simulation and it illustrates the impact that the increase in forcing voltage has on the flow entropy. The increase from $0V_{pp}$ to $8V_{pp}$ is less than 1 order of magnitude while the increase from $8V_{pp}$ to $20V_{pp}$ increases the entropy value by 2 orders of magnitude.

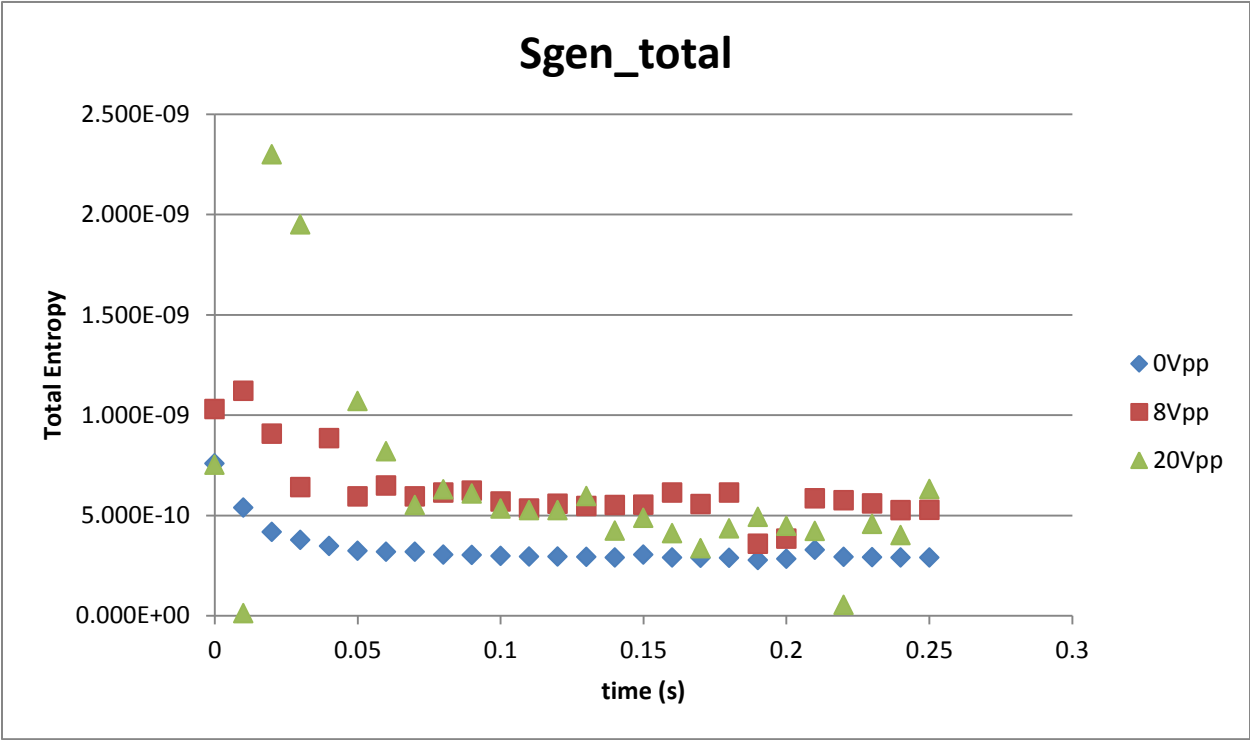


Figure 49: Total Entropy generated

PAGE LEFT INTENTIONALLY BLANK

CHAPTER V: CONCLUSIONS

The results of this thesis show that it is feasible to observe (using CFD) the turbulent flow properties witnessed in the electrokinetically-forced microfluidic mixer experiments performed by Wang et al [26]. While the calculated values for the quantities of interest were not the same as the experimental data, the values were within the same order of magnitude of those reported by the experiments and showed the same trends in each of the indicators of turbulence looked at: fast diffusion, high dissipation, irregularity and 3-D flow.

The results section illustrates the effects of electrokinetic forcing in microfluidic mixing found through the use of CFD software. [Figure 36](#) & [Figure 37](#) depict the fast diffusion in the channel that takes place within 0.25s of starting the flow and applying the electric field. The concentration has reached a near-homogeneous state at $x = 0.5\text{mm}$ and secondary flows have started downstream which shows that a 5.0 mm channel is more than long enough for complete mixing of the 2 fluids; in fact a 0.75mm channel would likely suffice to completely mix the fluids in 0.25s. From [Figure 45](#) it can be seen that with a $20V_{pp}$ forcing voltage the turbulent energy increases by up to two orders of magnitude ($10^8 - 10^6$) which indicates a greater mixing capability and, by extension, greater heat transfer potential; the two-magnitude increase in entropy seen in figures [Figure 47](#) - [Figure 49](#) would indicate the same.

Discrepancies in the range of T_e compared to Wang et al. may be due to assuming-out real world phenomena in an effort to simplify the simulations. Adding in the effects from an electroosmotic-wall boundary condition and the drag effects on the fluid due to the movement of the sodium and chlorine atoms in the electric field may help to explain the differences seen between the experimental and simulation data. Also, this study was done using laminar flow

equations that are much less complex than the turbulent model equations. While there are many different turbulence models that can be used for incompressible turbulent flow, the standard is the Reynolds averaged Navier-Stokes (RANS), κ - ϵ model [58].

The RANS equation showing the components of turbulent kinetic energy (k here) [24] using the Einstein summation notation is

$$\underbrace{\frac{\partial k}{\partial t}}_{\text{Local derivative}} + \underbrace{\bar{u}_j \frac{\partial k}{\partial x_j}}_{\text{Advection}} = \underbrace{\frac{1}{\rho_0} \frac{\partial \overline{u'_i p'}}{\partial x_i}}_{\text{Pressure diffusion}} - \underbrace{\frac{1}{2} k \frac{\overline{u'_j u'_j u'_i}}{\partial x_i}}_{\substack{\text{Turbulent} \\ \text{transport} \\ \mathcal{T}}} + \underbrace{\frac{1}{\mu} \frac{\partial^2 k}{\partial x_j^2}}_{\substack{\text{Molecular} \\ \text{viscous} \\ \text{transport}}} - \underbrace{\overline{u'_i u'_j} \frac{\partial \bar{u}_i}{\partial x_j}}_{\substack{\text{Production} \\ \mathcal{P}}} - \underbrace{\frac{1}{\mu} \frac{\partial \overline{u'_i} \partial \overline{u'_i}}{\partial x_j \partial x_j}}_{\substack{\text{Dissipation} \\ \epsilon_k}} - \underbrace{\frac{g}{\rho_0} \overline{\rho' u'_i} \delta_{i3}}_{\substack{\text{Buoyancy flux} \\ b}}$$

(52)

The five right-most terms in equation (52) are not accounted for in this thesis and may account for deviations from the experimentally observed data.

Future work recommendations include:

- Move the trailing edge of the inlet dividing plate to the entrance of the channel instead of upstream. This may eliminate secondary flows that occur before the fluid enters the channel and confine the entropy generation to the channel (i.e. largest $\Delta\sigma$ is at the plane $x = 0$).
- Run simulations at the *Normal* mesh resolution and increase the solution time to determine the time needed to reach a fully-mixed outflow.

- Incorporate heat transfer into the simulation to quantify the effects of μ EKT on heat transfer. Determine viability of scavenging excess heat with Peltier-type device to provide electrode voltage.
- Develop simulation using *Turbulent Flow* interface for comparison to this thesis's results and to provide additional validation for Wang et al. experiments.
- Possible collaboration with Wang et al. to further develop the simulation models.

PAGE LEFT INTENTIONALLY BLANK

REFERENCES

- [1] Assael, Marc J., Ifigeneia Mextexa, Konstantinos E. Kakosimos. "Thermal Conductivity of Nanofluids – Experimental and Theoretical" *International Journal of Thermophysics*, 27 (4): 999-1017. January 2006.
- [2] Putra, Nandy et al. "An Experimental Study on Thermal Performance of Nano Fluids in Microchannel Heat Exchanger." *International Journal of Technology* [Online], 4.2 (2013): 167-177. Web. 23 Sep. 2016.
- [3] Bejan, Adrian. *Convection Heat Transfer*. John Wiley & Sons, 1984.
- [4] Chang, Chih-Chang ; Yang, Ruey-Jen. "Electrokinetic Mixing in Microfluidic Systems" *Microfluidics and Nanofluidics* 3.5 (2007): 501-525. *ProQuest*. Web 4 Dec 2016.
- [5] Groisman, Alexander, and Victor Steinberg. "Elastic turbulence in a polymer solution flow." *Nature* 405.6782 (2000): 53-55.
- [6] Herwig, Heinz, and Bastian Schmandt. "How to determine losses in a flow field: A Paradigm Shift towards the Second Law Analysis." *Entropy* 16.6 (2014): 2959-2989.
- [7] Herwig, Heinz. "What Exactly is the Nusselt Number in Convective Heat Transfer Problems and are There Alternatives?" *Entropy* 18.5 (2016): 198.
- [8] Herwig, Heinz, and Christoph Redecker. "Heat transfer and entropy." *Heat transfer studies and applications*. ISBN (2015): 978-953.
- [9] Oztop, Hakan F., and Khaled Al-Salem. "A review on entropy generation in natural and mixed convection heat transfer for energy systems." *Renewable and Sustainable Energy Reviews* 16.1 (2012): 911-920.

- [10] Hinze, J.O. *Turbulence: An Introduction to Its Mechanism and Theory*. McGraw-Hill Book Company, Inc., 1959.
- [11] Incropera, Frank P., David P. Dewitt, Theodore L., Bergman, and Adrienne S. Lavine. *Fundamentals of Heat and Mass Transfer*. John Wiley & Sons, Inc., 2007.
- [12] Kandlikar, S., S. Garimella, D. Li, S. Colin, M.R. King. *Heat transfer and fluid flow in minichannels and microchannels*. Elsevier, 2005.
- [13] Lee, Chia-Yen et al. "Microfluidic Mixing: A Review." *International Journal of Molecular Sciences* 12.5 (2011): 3263–3287. PMC. Web. 23 Sept. 2016.
- [14] Lemley, Evan C., et al. "Milli-Scale Junction Flow Experiments." *ASME 2010 3rd Joint US-European Fluids Engineering Summer Meeting collocated with 8th International Conference on Nanochannels, Microchannels, and Minichannels*. American Society of Mechanical Engineers, 2010.
- [15] Luo, Lingai, Yilin Fan, and Daniel Tondeur. "Heat exchanger: from micro- to multi- scale design optimization." *International Journal of Energy Research* 31.13 (2007): 1266- 1274.
- [16] Martin, Holger. *Heat Exchangers*. Hemisphere Publishing Corporation, 1992.
- [17] Mehendale SS, Jacobi AM, Shah RK. "Fluid Flow and Heat Transfer at Micro- and Meso-Scales with Application to Heat Exchanger Design." *ASME. Appl. Mech. Rev.* 53.7 (2000):175-193. doi:10.1115/1.3097347.
- [18] Peng XF, Peterson OP, and Wang BX. "Heat transfer characteristics of water flowing through microchannels" *Exp Heat Transfer* 7(1994): 265-283.
[dx.doi.org/10.1080/08916159408946485](https://doi.org/10.1080/08916159408946485).

- [19] Munson, Bruce R., Donald F. Young, and Theodore H. Okiishi. *Fundamentals of Fluid Mechanics*. John Wiley & Sons, Inc., 2006.
- [20] *HYDRODYNAMIC FORCES*. Clarkson University, n.d. Web. 25 Nov. 2016.
webspaces.clarkson.edu/projects/fluidflow/courses/me537/1_2Drag.pdf.
- [21] Saffaripour, Meghdad, and Richard Culham. "Measurement of Entropy Generation in Microscale Thermal-Fluid Systems." *Journal of Heat Transfer* 132.12 (2010): 121401-1 - 121401-9.
- [22] Stone, H.A., A.D. Stroock, and A. Ajdarji. "Engineering Flows in Small Devices: Microfluidic Toward a Lab-on-a-Chip." *Annu. Rev. Fluid Mech.* 36 (2004):381-411.
- [a] Sammarco, Timothy S., and Mark A. Burns. "Thermocapillary pumping of discrete drops in microfabricated analysis devices." *AIChE Journal* 45.2 (1999): 350-366.
deepblue.lib.umich.edu/bitstream/handle/2027.42/34237/690450215_ftp.pdf?sequence=1
- [b] Pollack, Michael G., Richard B. Fair, and Alexander D. Shenderov. "Electrowetting-based actuation of liquid droplets for microfluidic applications." *Applied Physics Letters* 77.11 (2000): 1725-1726. microfluidics.ee.duke.edu/doc/Pollack.2000.pdf .
- [c] Prins, M. W. J., W. J. J. Welters, and J. W. Weekamp. "Fluid control in multichannel structures by electrocapillary pressure." *Science* 291.5502 (2001): 277-280.
www.jstor.org.vortex3.uco.edu/stable/3082337?seq=1#page_scan_tab_contents
- [d] Gallardo, Benedict S., et al. "Electrochemical principles for active control of liquids on submillimeter scales." *Science* 283.5398 (1999): 57-60.
web.a.ebscohost.com.vortex3.uco.edu/ehost/

- [e] Kataoka, Dawn E., and Sandra M. Troian. "Patterning liquid flow on the microscopic scale." *Nature* 402.6763 (1999): 794-797. web.a.ebscohost.com.vortex3.uco.edu/ehost/
- [f] Bau, Haim H., Jihua Zhong, and Mingqiang Yi. "A minute magneto hydro dynamic (MHD) mixer." *Sensors and Actuators B: Chemical* 79.2 (2001): 207-215. repository.upenn.edu/cgi/viewcontent.cgi?article=1130&context=meam_papers
- [g] Johnson, R. Daniel, et al. "Development of a fully integrated analysis system for ions based on ion-selective optodes and centrifugal microfluidics." *Analytical chemistry* 73.16 (2001):3940-3946. pubs.acs.org.vortex3.uco.edu/doi/abs/10.1021/ac0102819.
- [23] "Micro Heat Exchanger." *Wikipedia*. Wikimedia Foundation, n.d. Web. 06 Dec. 2016. en.wikipedia.org/wiki/Micro_heat_exchanger.
- [24] "Turbulence kinetic energy." *Wikipedia*. Wikimedia Foundation, n.d. Web. 06 Jan. 2017. en.wikipedia.org/wiki/Turbulence_kinetic_energy.
- [25] Wang, Guiren. Email correspondence with author, December 2016.
- [26] Wang, G. R., Fang Yang, and Wei Zhao. "There can be turbulence in microfluidics at low Reynolds number." *Lab on a Chip* 14.8 (2014): 1452-1458.
- [27] Wang, G. R., Fang Yang, and Wei Zhao. "Microelectrokinetic turbulence in microfluidics at low Reynolds number." *Physical Review E* 93.1 (2016):013106-1 - 013106-9. dx.doi.org/10.1103/PhysRevE.93.013106.
- [28] Wang, Guiren, et al. "On micro-electrokinetic scalar turbulence in microfluidics at a low Reynolds number." *Lab on a Chip* 16.6 (2016): 1030-1038. DOI: [10.1039/c5lc01541c](https://doi.org/10.1039/c5lc01541c)

- [29] Yang, Fang. "Electrokinetic Mixing and Separation in Microfluidic Systems." (Diss. U of South Carolina, 2013. *Scholar Commons*. University of South Carolina, 3 Dec. 2013. Web. 15 Nov. 2016. scholarcommons.sc.edu/etd/2260).
- [30] Yang, Fang, et al. "AC electrokinetic fast mixing in non-parallel microchannels." *Chemical Engineering Communications* just-accepted (2016).
[dx.doi.org/10.1080/00986445.2016.1253009](https://doi.org/10.1080/00986445.2016.1253009)
- [31] Zhao, Wei. "Low Reynolds Number Turbulence: Mechanisms and Applications." Diss. U South Carolina, 2014. *Scholar Commons*. University of South Carolina, 26 Jan. 2015. Web. 15 Nov. 2016. scholarcommons.sc.edu/etd/2999.
- [32] Zhao, Wei, et al. "Measurement of velocity fluctuations in microfluidics with simultaneously ultrahigh spatial and temporal resolution." *Experiments in Fluids* 57.1 (2016): 1-12.
- [33] *CFD Online*. N.p., 11 June 2011. Web. Nov. 2016. www.cfd-online.com/Wiki/Turbulence_kinetic_energy.
- [34] Han, Yanhui, et al. "A review of development of micro-channel heat exchanger applied in air-conditioning system." *Energy Procedia* 14 (2012): 148-153.
- [35] Stolpa, Scott. "Turbulent heat transfer." *South Bend: University of Notre Dame* (2004).
[10.1.1.119.9693](https://doi.org/10.1.1.119.9693)
- [36] Yang, Chien-Yuh, Chun-Ta Yeh, Wei-Chi Liu, Bing-Chwen Yang. "Advanced micro-heat exchangers for high heat flux." *Heat Transfer Engineering* 28.8-9 (2007): 788-794.
- [37] Baygents, J.C. and F. Baldessari, "Electrohydrodynamic instability in a thin fluid layer with an electrical conductivity gradient". *Physics of Fluids* 10 (1998): 301.

- [38] Pethig, R. and G.H. Markx. "Applications of dielectrophoresis in biotechnology". *Trends in Biotechnology*, 1997. 15(10): 426-432.
- [39] Markx, G.H., P.A. Dyda, and R. Pethig. "Dielectrophoretic separation of bacteria using a conductivity gradient". *Journal of Biotechnology* **51.2** (1996): 175-180.
- [40] Schnelle, T., et al. "Single micro electrode dielectrophoretic tweezers for manipulation of suspended cells and particles". *Biochimica et Biophysica Acta (BBA) - General Subjects* 1428.1 (1999): 99-105.
- [41] Hughes, M.P., et al., "Manipulation of herpes simplex virus type 1 by dielectrophoresis". *Biochimica et Biophysica Acta (BBA) - General Subjects* 1425.1 (1998): 119-126.
- [42] Becker, F.F., et al. "Separation of human breast cancer cells from blood by differential dielectric affinity". *Proceedings of the National Academy of Sciences of the United States of America* 92.3 (1995): 860-864.
- [43] Huang, Y., et al. "The Removal of Human Breast Cancer Cells from Hematopoietic CD34+ Stem Cells by Dielectrophoretic Field-Flow-Fractionation". *Journal of Hematotherapy & Stem Cell Research* 8.5 (1999): 481-490.
- [44] Ahmed, Daniel, et al. "A fast microfluidic mixer based on acoustically driven sidewall-trapped microbubbles." *Microfluidics and Nanofluidics* 7.5 (2009): 727-731.
- [45] Storey, Brian D., et al. "Electrokinetic instabilities in thin microchannels." *Physics of Fluids (1994-present)* 17.1 (2005): 018103. aip.scitation.org/doi/10.1063/1.1823911
- [46] Lin, Hao, et al. "Instability of electrokinetic microchannel flows with conductivity gradients." *Physics of Fluids (1994-present)* 16.6 (2004): 1922-1935.

- [47] Polshettiwar, S. A. *AuthorSTREAM*. Maeer's Maharashtra Institute of Pharmacy, n.d. Web. 1 Jan. 2017. www.authorstream.com/Presentation/satishmip-1168615-osmotic-pump-delivery-system/.
- [48] Ryden, Barbara. *Astronomy 825 - Radiative Gas Dynamics*. Ohio State Department of Astronomy, 3 Jan. 2011. Web. 2 Dec. 2016. www.astronomy.ohio-state.edu/~ryden/ast825/ch7.pdf.
- [49] Schlegel, Fabrice. "Modeling Electroosmotic Flow and the Electrical Double Layer." Blog post. *COMSOL Multiphysics*. COMSOL Inc., 28 Oct. 2013. Web. 10 Nov. 2016. www.comsol.com/blogs/modeling-electroosmotic-flow-electrical-double-layer/.
- [50] Temiz, Yuksel, et al. "Lab-on-a-chip devices: How to close and plug the lab?" *Microelectronic Engineering* 132 (2015): 156-175.
- [51] Beebe, David J., Glennys A. Mensing, and Glenn M. Walker. "Physics and applications of microfluidics in biology." *Annual review of biomedical engineering* 4.1 (2002): 261-286.
- [52] Kee, Robert J., et al. "The design, fabrication, and evaluation of a ceramic counter-flow microchannel heat exchanger." *Applied Thermal Engineering* 31.11 (2011): 2004-2012.
- [53] Jiang, Pei-Xue, et al. "Thermal-hydraulic performance of small scale micro-channel and porous-media heat-exchangers." *International Journal of Heat and Mass Transfer* 44.5 (2001): 1039-1051.
- [54] Tuckerman, David B., and R. F. W. Pease. "High-performance heat sinking for VLSI." *IEEE Electron device letters* 2.5 (1981): 126-129.
- [55] Chen, Chuan-Hua, et al. "Convective and absolute electrokinetic instability with conductivity gradients." *Journal of Fluid Mechanics* 524 (2005): 263-303.

- [56] Chan, Derek YC. "A simple algorithm for calculating electrical double layer interactions in asymmetric electrolytes—poisson–boltzmann theory." *Journal of colloid and interface science* 245.2 (2002): 307-310.
- [57] Lamb, Horace. *Hydrodynamics*. Cambridge university press, 1932.
- [58] NGOC-CUONG NGUYEN. "Turbulence Modeling". MIT, 5 Nov. 2005. Web. 26 Dec. 2016. www.mit.edu/~cuongng/Site/Publication_files/TurbulenceModeling_04NOV05.pdf
- [59] Wang, Xiayan, et al. "Electroosmotic pumps and their applications in microfluidic systems." *Microfluidics and Nanofluidics* 6.2 (2009): 145-162.
- [60] "What Is Convergence?" *COMSOL Discussion Forum*. COMSOL Inc. n.d. Web. 1 Dec. 2016. www.comsol.com/community/forums/general/thread/35375/.
- [61] "Solving Time Dependent CFD Simulations." *COMSOL Knowledge Base*. COMSOL Inc., n.d. Web. 02 Jan. 2017. www.comsol.com/support/knowledgebase/1172/.
- [62] "Solving Multiphysics Problems" *COMSOL Discussion Forum*. COMSOL Inc., n.d. Web. 25 Feb. 2017. www.comsol.com/blogs/solving-multiphysics-problems
- [63] McQuarrie, Donald Allan. *Mathematical methods for scientists and engineers*. University Science Books, 2003.
- [64] COMSOL Inc., n.d. Web. multiscalemodeling.colorado.edu/liu/misc/COMSOL_training/Day1.pdf
- [65] COMSOL Inc., n.d. Web. multiscalemodeling.colorado.edu/liu/misc/COMSOL_training/Day2.pdf
- [66] COMSOL Multiphysics® v. 5.2a. www.comsol.com. COMSOL AB, Stockholm, Sweden.

- [67] CADImportModuleUsersGuide. COMSOL Multiphysics® v. 5.2a. COMSOL AB, Stockholm, Sweden. 2016.
- [68] LiveLinkForSOLIDWORKSUsersGuide. COMSOL Multiphysics® v. 5.2a. COMSOL AB, Stockholm, Sweden. 2016.
- [69] CFDModuleUsersGuide. COMSOL Multiphysics® v. 5.2a. COMSOL AB, Stockholm, Sweden. 2016.
- [70] ChemicalReactionEngineeringModuleUsersGuide. COMSOL Multiphysics® v. 5.2a. COMSOL AB, Stockholm, Sweden. 2016.
- [71] MicrofluidicsApplicationLibraryManual. COMSOL Multiphysics® v. 5.2a. COMSOL AB, Stockholm, Sweden. 2016.
- [72] MicrofluidicsModuleUsersGuide. COMSOL Multiphysics® v. 5.2a. COMSOL AB, Stockholm, Sweden. 2016.
- Included for readers reference, not specifically cited in thesis.
- i. COMSOL_MultiphysicsInstallationGuide. COMSOL Multiphysics® v. 5.2a. COMSOL AB, Stockholm, Sweden. 2016.
 - ii. COMSOL_ReferenceManual. COMSOL Multiphysics® v. 5.2a. COMSOL AB, Stockholm, Sweden. 2016.
 - iii. ACDCModuleUsersGuide. COMSOL Multiphysics® v. 5.2a. COMSOL AB, Stockholm, Sweden. 2016.
 - iv. COMSOL_PostprocessingAndVisualization. COMSOL Multiphysics® v. 5.2a. COMSOL AB, Stockholm, Sweden. 2016.
 - v. COMSOL_SpecializedTechniquesForPostprocessingAndVisualization. COMSOL Multiphysics® v. 5.2a. COMSOL AB, Stockholm, Sweden. 2016.

PAGE LEFT INTENTIONALLY BLANK

APPENDIX A

These are the scripts used to run COMSOL as a batch job on the BUDDY cluster. The associated hostfile (a list of available nodes) is given for each script as well. It requests run parameters from the user at execution and automates the COMSOL job creation requiring no programming and limited Linux knowledge; a user only needs to navigate to the folder containing the batch script and run the “./” command on the script.

hostfile

```
buddy1.cluster  
buddy2.cluster  
buddy3.cluster  
buddy4.cluster  
buddy5.cluster  
buddy6.cluster  
buddy7.cluster  
buddy8.cluster  
buddy9.cluster  
buddy10.cluster  
buddy11.cluster  
buddy12.cluster  
buddy13.cluster  
buddy14.cluster  
buddy15.cluster  
buddy16.cluster  
buddy17.cluster  
buddy18.cluster  
buddy19.cluster  
buddy20.cluster  
buddy21.cluster  
buddy22.cluster  
buddy23.cluster  
buddy24.cluster  
buddy25.cluster  
buddy26.cluster  
buddy27.cluster
```

hostfile_himem

```
hi-mem01.cluster  
hi-mem02.cluster  
hi-mem03.cluster  
hi-mem04.cluster
```

COMSOL batch scripts

```
#!/bin/bash

#####
####          To run this file use          ####
####          ./willy_test.sh              ####
#####

echo -n "What would you like to name your job? "
read JOB_NAME
echo -n "How many cores do you want to run on? "
read NUM_CORES
echo -n "How long do you want to give the job to run? (D-HH:MM:SS) "
read RUNTIME
echo -n "Enter the input file path > "
read INPUTFILE
echo -n "Enter the output file path > "
read OUTPUTFILE
echo -n "Enter the email you would like alerts sent to: "
read EMAIL                                     #uncomment to accept user input for email

#=====Calculate the number of nodes needed ($NNODES)=====
CORE_PER_NODE_MAX=16                          #16 sets the max node load to 80%, 18 sets it to 90%

if ((NUM_CORES < $((CORE_PER_NODE_MAX + 1)))
then
    NNODES=1
else
#calculates a floating value for NNODES
    NNODES=$(echo "scale=2; $NUM_CORES/$CORE_PER_NODE_MAX" | bc)

#simulate "floor"
    FLOOR=$(echo $NNODES|cut -f1 -d".")

#simulate "ceiling"
    CEILING=$((FLOOR + 1))

#Check if NNODES is multiple of CORE_PER_NODE_MAX
    TEMP=$(echo "scale=2; $CEILING-$NNODES" | bc)

#Determine if NNODES should be rounded up or left alone (i.e. mult. of
CORE_PER_NODE_MAX)
    if (( $(bc <<< "$TEMP == 1.00") ))
    then
        #NNODES is good, convert back to integer
        NNODES=$(echo $NNODES|cut -f1 -d".")
    else
        #Round NNODES up and convert to integer
        NNODES=$(echo $CEILING|cut -f1 -d".")
    fi
fi

#=====
sbatch <<EOT          # this wrapper allows the sbatch commands to run using user
                    # input from above
#!/bin/bash

##SBATCH --test-only          # Validate the batch script and return an estimate
                             # of when a job would be scheduled

#SBATCH -J $JOB_NAME          # job name ##--job-name= < 10
characters
#SBATCH -o ${JOB_NAME}.out    # .out file
```

```

#SBATCH -p nodes # partition
#SBATCH -e ${JOB_NAME}.err # .err file
#SBATCH -t $RUNTIME # job runtime (D-HH:MM:SS)
#SBATCH -n $NUM_CORES --tasks-per-node=$CORE_PER_NODE_MAX # total cores per node
#SBATCH --exclusive
##SBATCH --exclude=gpu01,hi-mem03,hi-mem04 # exclude known down nodes

#SBATCH --mail-type=ALL
#SBATCH --mail-user=$EMAIL

#=====
if [ X"$SLURM_STEP_ID" = "X" -a X"$SLURM_PROCID" = "X"0 ]
then
  echo "print ====="
  echo "print SLURM_JOB_ID = $SLURM_JOB_ID"
  echo "print SLURM_NODELIST = $SLURM_NODELIST"
  echo "print ====="
fi
#=====

#in/out files (example paths)
#INPUTFILE=/home/wduffle/thesis/Thesis_Model_6_3_2.mph
#OUTPUTFILE=/home/wduffle/batch/results_6_3_2.mph

#=====
#---module comsol/52a data---
#source /usr/share/Modules/init/bash

module purge
module load comsol/52a

#=====
comsol -nn $NNODES -np $CORE_PER_NODE_MAX batch -f /home/wduffle/batch/hostfile
hostfile_himem
-mpirsh ssh -mpifabrics shm:ofa -mpmode owner -inputfile $INPUTFILE -outputfile
$OUTPUTFILE

# -mpifabrics intranode:internode
# -study "std2" # insert after $INPUTFILE to solve specific study
# where std2 is the COMSOL study name tag

# -clustersimple

EOT

echo "Have a Nice Day :)"

```

Script for running on the high memory nodes (hi-mem01.cluster-hi-mem04.cluster) where the available memory is 128BG vs 64GB for the standard nodes. Script sets max node load to 80%.

```
#!/bin/bash

#####
####          To run this file use          ####
####          ./willy_test_himem.sh          ####
#####

echo -n "What would you like to name your job? "
read JOB_NAME
echo -n "How many cores do you want to run on? "
read NUM_CORES
echo -n "How long do you want to give the job to run? (D-HH:MM:SS) "
read RUNTIME
echo -n "Enter the input file path > "
read INPUTFILE
echo -n "Enter the output file path > "
read OUTPUTFILE
#echo -n "Enter the email you would like alerts sent to: "
#read EMAIL #uncomment to accept user input for email

#=====Calculate the number of nodes needed ($NNODES)=====
CORE_PER_NODE_MAX=16 #16 sets the max node load to 80%

if ((NUM_CORES < (($CORE_PER_NODE_MAX + 1))))
then
    NNODES=1
#    echo $NNODES
else
#calculates a floating value for NNODES
    NNODES=$(echo "scale=2; $NUM_CORES/$CORE_PER_NODE_MAX" | bc)

#simulate "floor"
    FLOOR=$(echo $NNODES|cut -f1 -d".")

#simulate "ceiling"
    CEILING=$((FLOOR + 1))

#Check if NNODES is multiple of CORE_PER_NODE_MAX
    TEMP=$(echo "scale=2; $CEILING-$NNODES" | bc)

#Determine if NNODES should be rounded up or left alone (i.e. mult. of
CORE_PER_NODE_MAX)
    if (( $(bc <<< "$TEMP == 1.00") ))
    then
        #NNODES is good, convert back to integer
        NNODES=$(echo $NNODES|cut -f1 -d".")
    else
        #Round NNODES up and convert to integer
        NNODES=$(echo $CEILING|cut -f1 -d".")
    fi
fi
```



```

=====
sbatch <<EOT          # this wrapper allows the sbatch commands to run using user
input
                    # from above

#!/bin/bash
##SBATCH --test-only          # Validate the batch script and return an estimate
                             # of when a job would be scheduled

#SBATCH -J $JOB_NAME          # job name ##--job-name=
< 10 characters
#SBATCH -o ${JOB_NAME}.out    # .out file
#SBATCH -p nodes              # partition
#SBATCH -e ${JOB_NAME}.err    # .err file
#SBATCH -t $RUNTIME           # job runtime (D-HH:MM:SS)
#SBATCH -n $NUM_CORES --tasks-per-node=$CORE_PER_NODE_MAX # total cores per node
#SBATCH --exclusive
##SBATCH --exclude=gpu01,hi-mem03,hi-mem04 # exclude known down
nodes

#SBATCH --mail-type=ALL
#SBATCH --mail-user=wduffle@uco.edu

=====
if [ X"$SLURM_STEP_ID" = "X" -a X"$SLURM_PROCID" = "X"0 ]
then
  echo "print ====="
  echo "print SLURM_JOB_ID = $SLURM_JOB_ID"
  echo "print SLURM_NODELIST = $SLURM_NODELIST"
  echo "print ====="
fi
=====

#in/out files (example paths)
#INPUTFILE=/home/wduffle/thesis/Thesis_Model_6_3_2.mph
#OUTPUTFILE=/home/wduffle/batch/results_6_3_2.mph

=====
#---module comsol/52a data---
#source /usr/share/Modules/init/bash

module purge
module load comsol/52a

=====

comsol -nn $NNODES -np $CORE_PER_NODE_MAX batch -f
/home/wduffle/batch/hostfile_himem -mpirsh ssh -mpifabrics shm:ofa -mpmode owner
-inputfile $INPUTFILE -outputfile $OUTPUTFILE

# -mpifabrics intranode:internode
# -study "std2"          # insert after $INPUTFILE to solve specific study
                       # where std2 is the COMSOL study name
# -step "time"          # where time is the COMSOL step name
# -clustersimple

EOT

echo "Have a Nice Day :)"

```

Script for running on the high memory nodes (hi-mem01.cluster-hi-mem04.cluster). Script sets max node load to 90% for when only one node is needed but more than 80% loading is desired.

```
#!/bin/bash

#####
####          To run this file use          ####
####          ./willy_test_himem_90.sh      ####
#####

echo -n "What would you like to name your job? "
read JOB_NAME
echo -n "How many cores do you want to run on? "
read NUM_CORES
echo -n "How long do you want to give the job to run? (D-HH:MM:SS) "
read RUNTIME
echo -n "Enter the input file path > "
read INPUTFILE
echo -n "Enter the ouput file path > "
read OUTPUTFILE
#echo -n "Enter the email you would like alerts sent to: "
#read EMAIL

#=====Calculate the number of nodes needed=====
CORE_PER_NODE_MAX=18          #18 sets the max node load to 90%

if ((NUM_CORES < $((CORE_PER_NODE_MAX + 1))))
then
    NNODES=1
#    echo $NNODES
else
#calculates a floating value for NNODES
    NNODES=$(echo "scale=2; $NUM_CORES/$CORE_PER_NODE_MAX" | bc)

#simulate "floor"
    FLOOR=$(echo $NNODES|cut -f1 -d".")

#simulate "ceiling"
    CEILING=$((FLOOR + 1))

#Check if NNODES is multiple of CORE_PER_NODE_MAX
    TEMP=$(echo "scale=2; $CEILING-$NNODES" | bc)

#Determine if NNODES should be rounded up or left alone (i.e. mult. of
CORE_PER_NODE_MAX)
    if (( $(bc <<< "$TEMP == 1.00") ))
    then
        #NNODES is good, convert back to integer
        NNODES=$(echo $NNODES|cut -f1 -d".")
    else
        #Round NNODES up and convert to integer
        NNODES=$(echo $CEILING|cut -f1 -d".")
    fi
fi
```

```

=====
sbatch <<EOT
#!/bin/bash

##SBATCH --test-only                # Validate the batch
script and return an estimate      # of when a job would be
scheduled

#SBATCH -J $JOB_NAME                # job name ##--job-name=
< 10 characters
#SBATCH -o ${JOB_NAME}.out          # .out file
#SBATCH -p nodes                    # partition
#SBATCH -e ${JOB_NAME}.err          # .err file
#SBATCH -t $RUNTIME                 # job runtime (D-HH:MM:SS)
#SBATCH -n $NUM_CORES --tasks-per-node=$CORE_PER_NODE_MAX # total cores --cores
per node
#SBATCH --exclusive
##SBATCH --exclude=gpu01,hi-mem03,hi-mem04 # exclude known down
nodes

#SBATCH --mail-type=ALL
#SBATCH --mail-user=wduffle@uco.edu

=====
if [ X"$SLURM_STEP_ID" = "X" -a X"$SLURM_PROCID" = "X"0 ]
then
  echo "print ====="
  echo "print SLURM_JOB_ID = $SLURM_JOB_ID"
  echo "print SLURM_NODELIST = $SLURM_NODELIST"
  echo "print ====="
fi
=====

#in/out files (example paths)
#INPUTFILE=/home/wduffle/thesis/Thesis_Model_6_3_2.mph
#OUTPUTFILE=/home/wduffle/batch/results_6_3_2.mph

=====
#----module comsol/52a data----
#source /usr/share/Modules/init/bash

module purge
module load comsol/52a

=====

comsol -nn $NNODES -np $CORE_PER_NODE_MAX batch -f
/home/wduffle/batch/hostfile_himem -mpirsh ssh -mpifabrics shm:ofa -mpmode owner
-inputfile $INPUTFILE -outputfile $OUTPUTFILE
# -study "std2"                # insert after $INPUTFILE to solve specific study
                                # where std2 is the COMSOL study name
# -step "time"                 # where time is the COMSOL step name
# -clustersimple

EOT

echo "Have a Nice Day :)"

```

Permission to Publish and Use COMSOL Multiphysics Images

Phil Kinnane
VP of Business Development
COMSOL, Inc.
100 District Avenue
Burlington, MA 01803 USA
Email: phil@comsol.com
Tel: +1 781-273-3322
Fax: +1 781-273-6603

COMSOL hereby grants you permission to reproduce, publish and distribute the image listed in Schedule A, in your Master's Thesis as well as in subsequent editions of your Master's Thesis in all media of expression now known or later developed and in all foreign language translations, for distribution throughout the world subject to your compliance with the following terms and conditions:

1. You shall comply with COMSOL's Trademark Guidelines set forth at: <http://www.comsol.com/company/trademarks/>.
2. You insert the phrase "Image credit: COMSOL." underneath the image.
3. You acknowledge that you are receiving the COMSOL Materials "As Is" without any representations or warranties of any kind including, but not limited to any implied warranties of merchantability, fitness for a particular purpose or non-infringement.

This permission shall last until you receive a written request from COMSOL to terminate this permission, except that no such termination shall operate to revoke permission granted with respect to instances in which the images and/or descriptions have already been placed in circulation. I understand and acknowledge the above requirements,

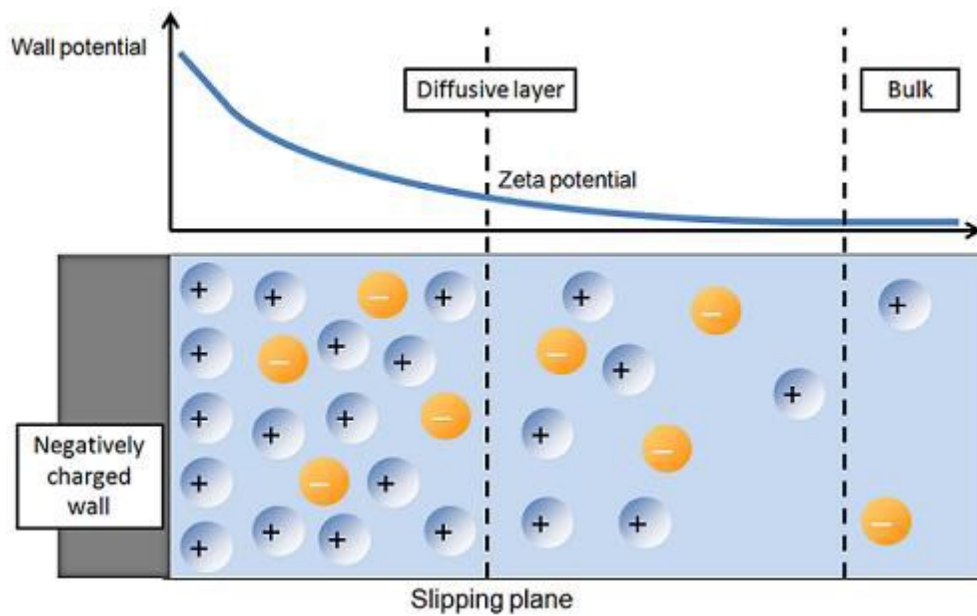
Signed: _____

Name: Willy Duffle

Date: 11 Jan 2017

Company/Institution: University of Central Oklahoma

SCHEDULE A



Electrical double layer (EDL).

Source: <https://www.comsol.com/blogs/modeling-electroosmotic-flow-electrical-double-layer/>

PAGE LEFT INTENTIONALLY BLANK

APPENDIX B

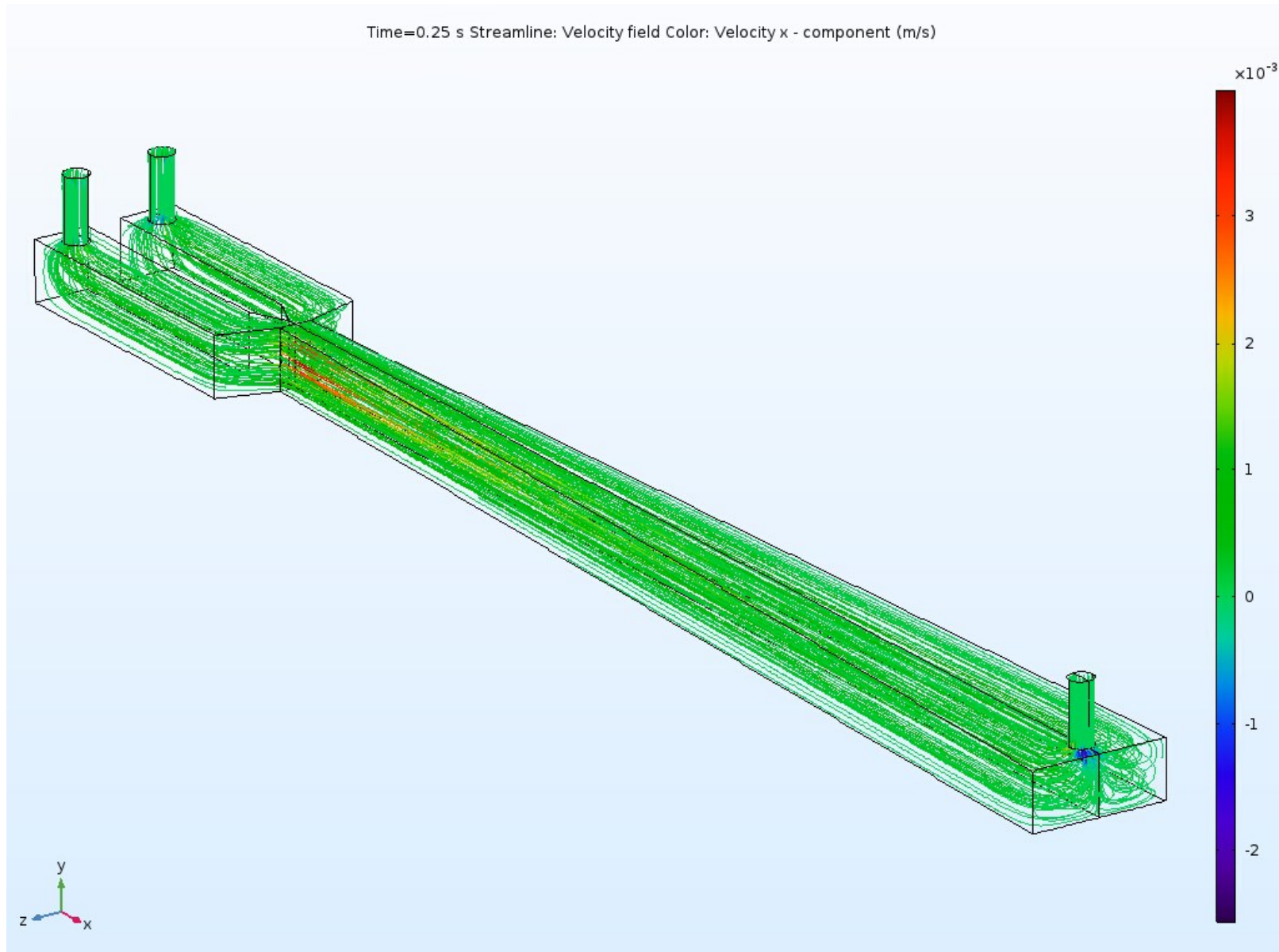


Figure 50: Streamlines $0V_{pp}$

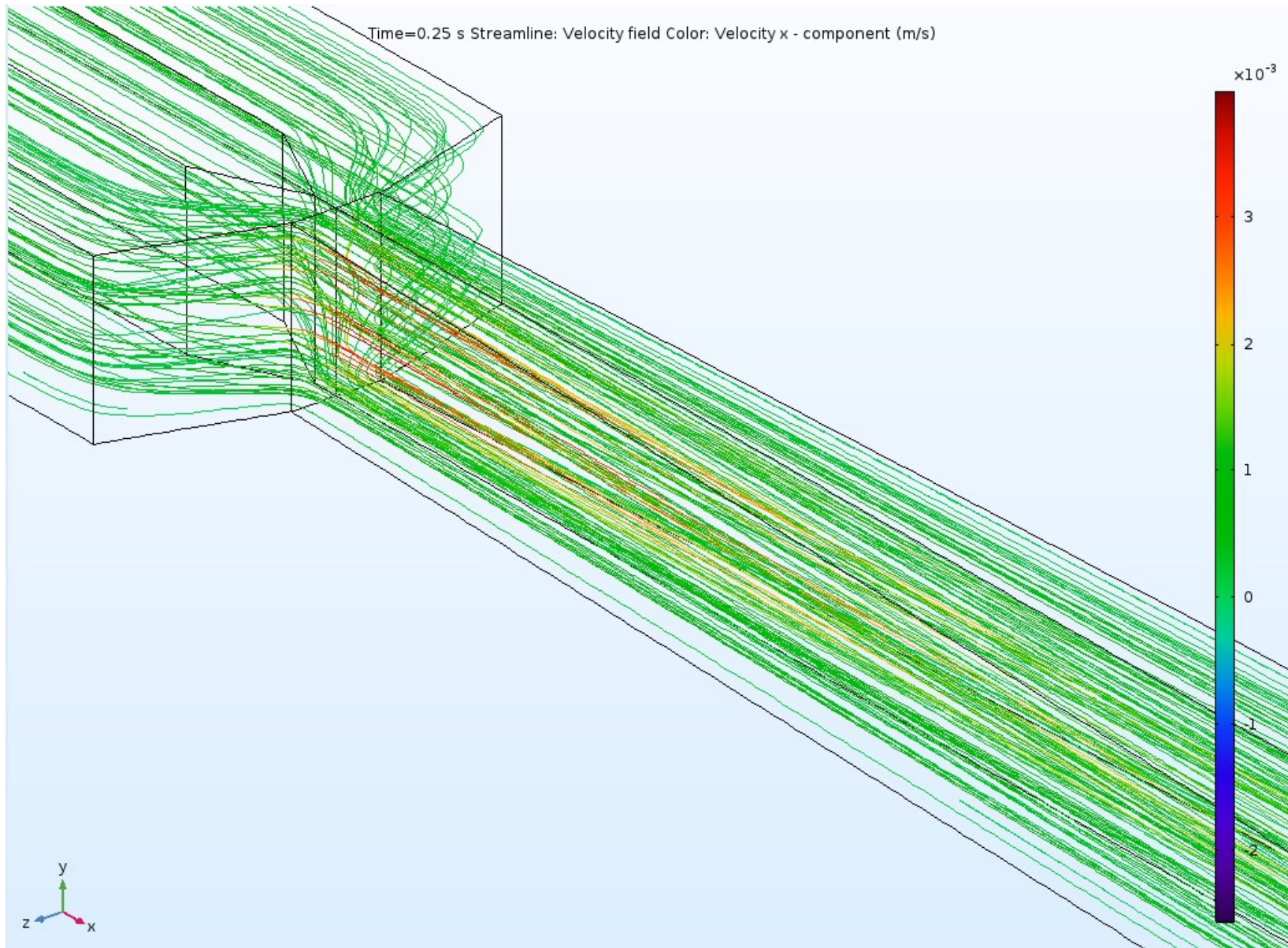


Figure 51: Streamlines $0V_{pp}$

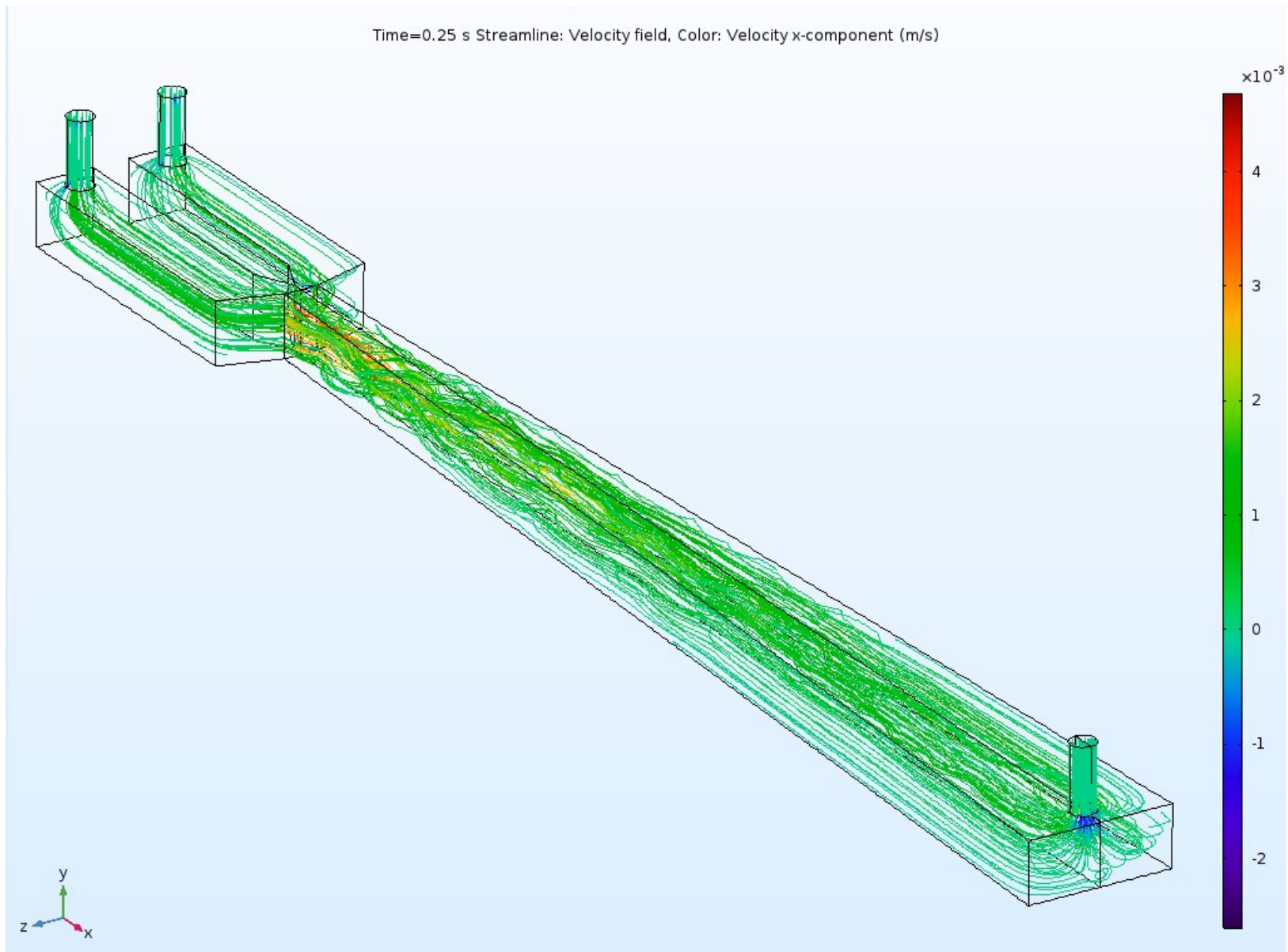


Figure 52: Streamlines $8V_{pp}$

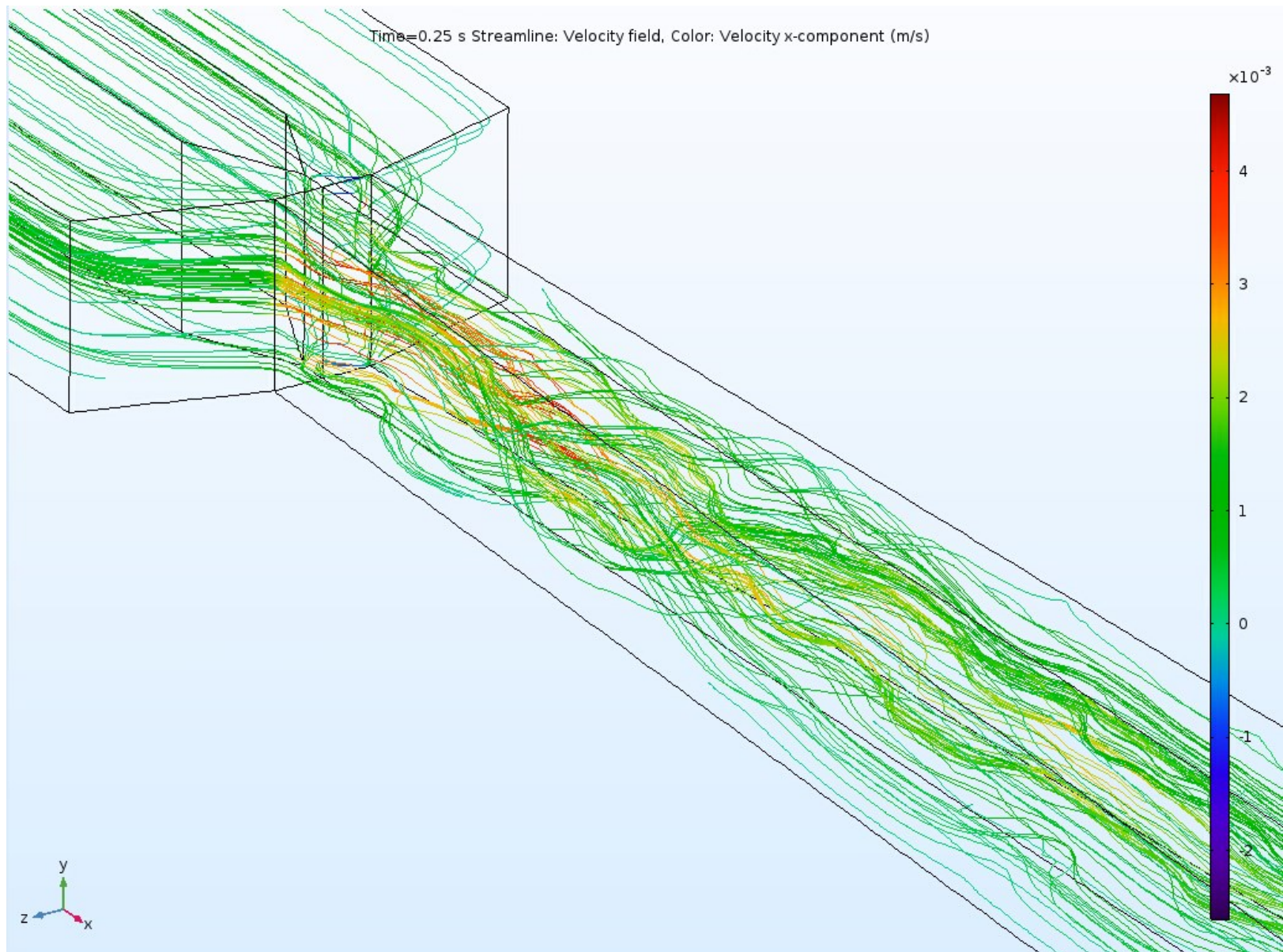


Figure 53: Streamlines $8V_{pp}$

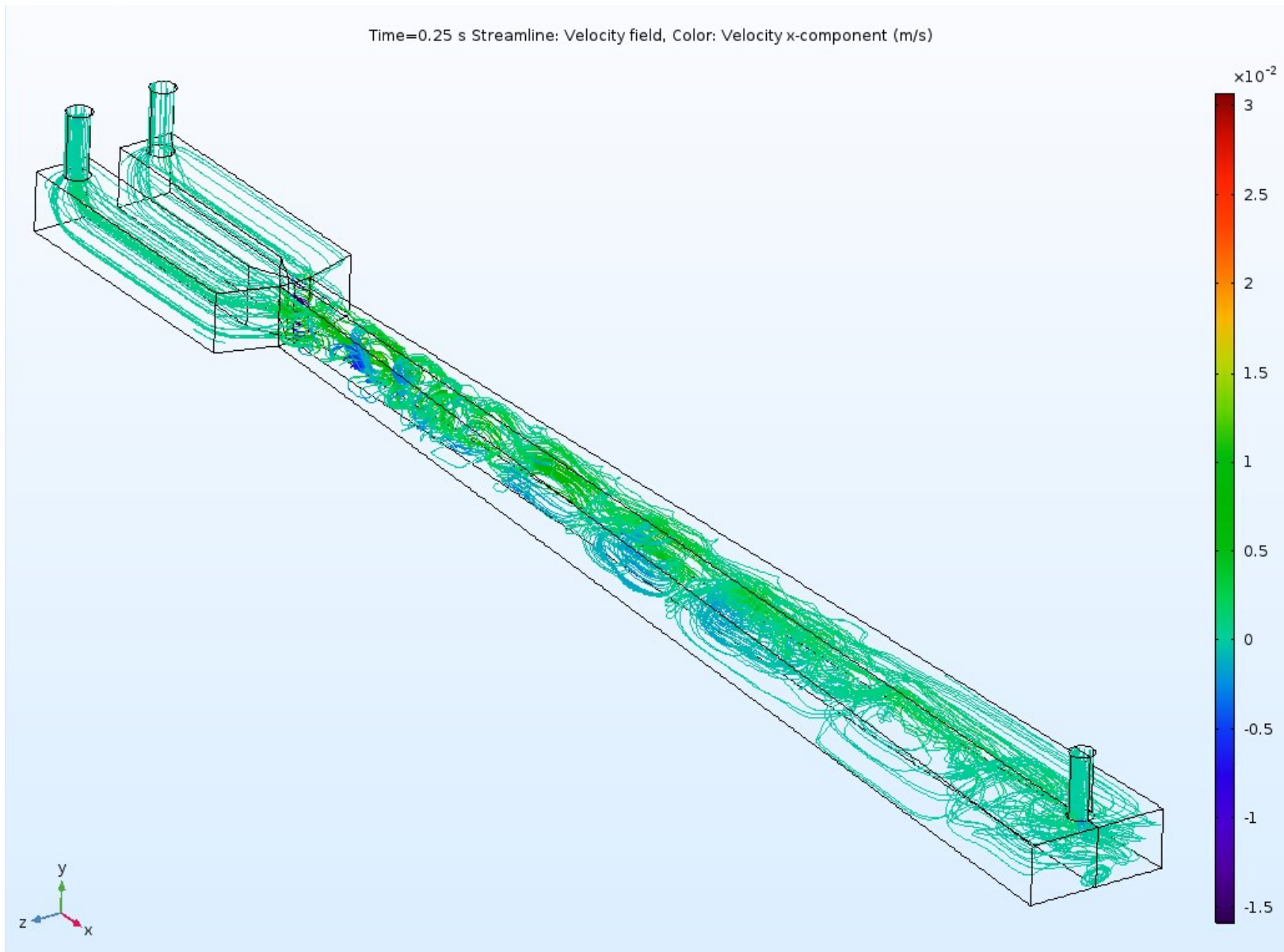


Figure 54: Streamlines $20V_{pp}$

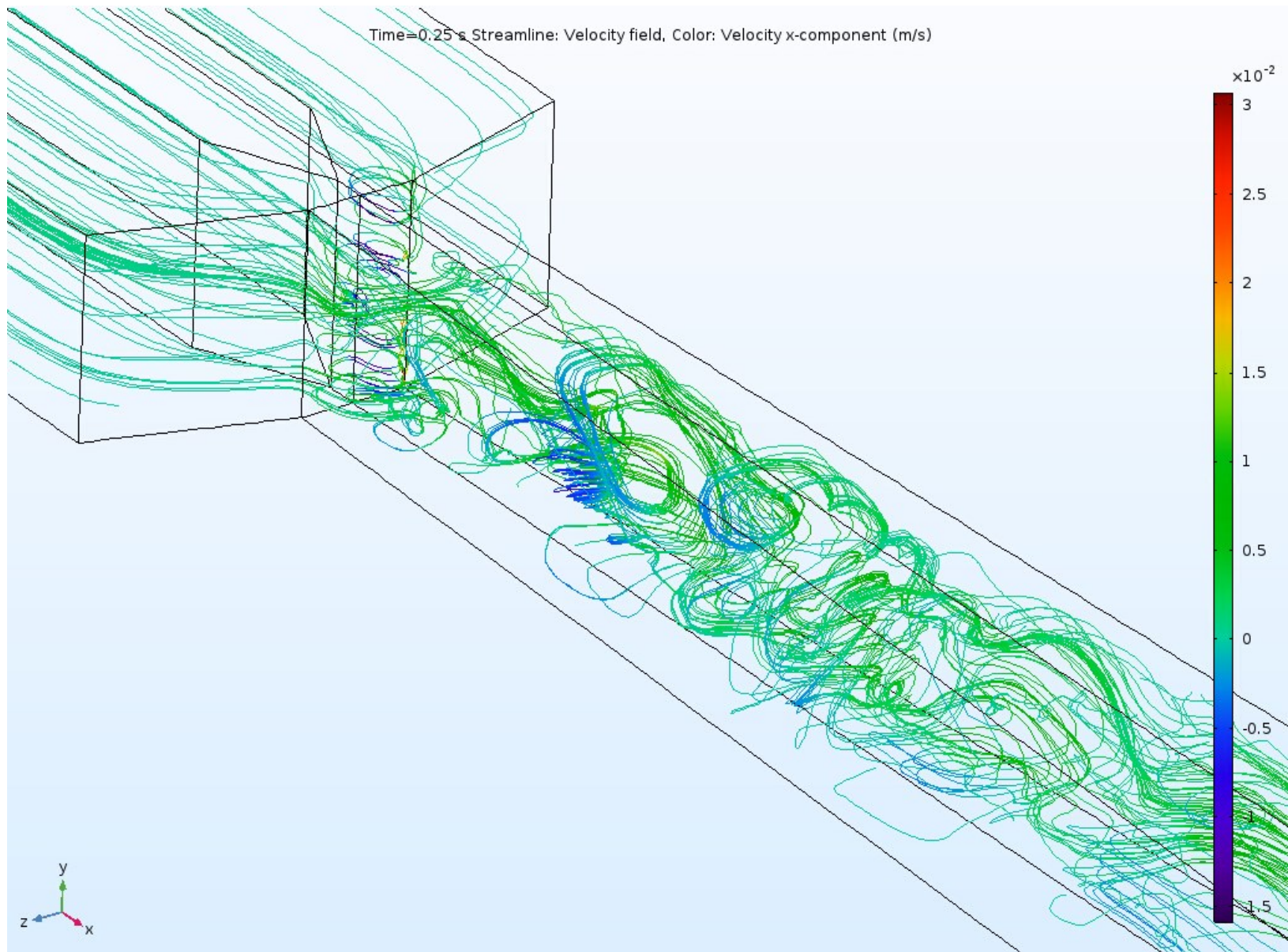


Figure 55: Streamlines $20V_{pp}$

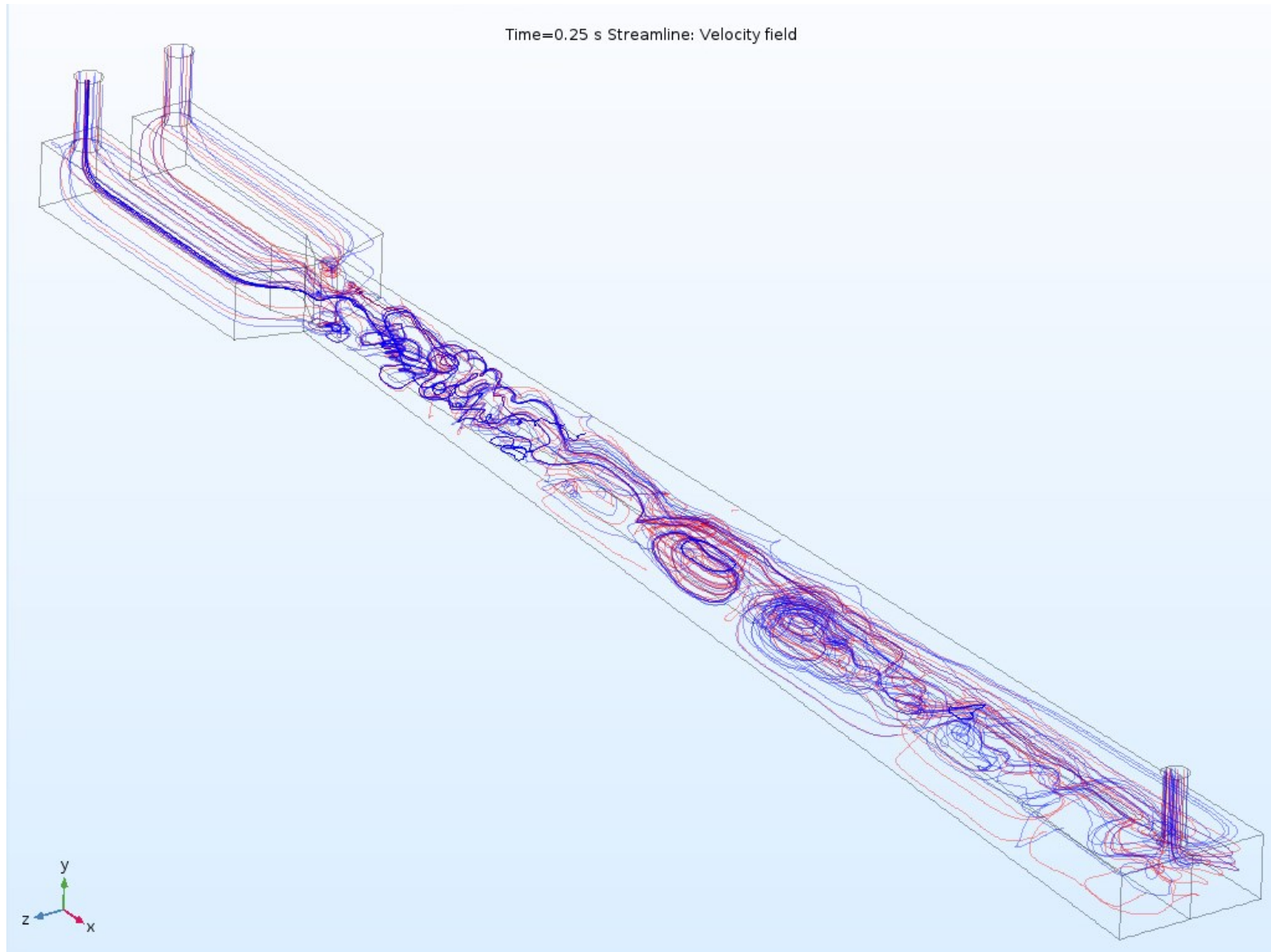


Figure 56: Streamlines $20V_{pp}$
(showing secondary flows at $t = 0.25s$)

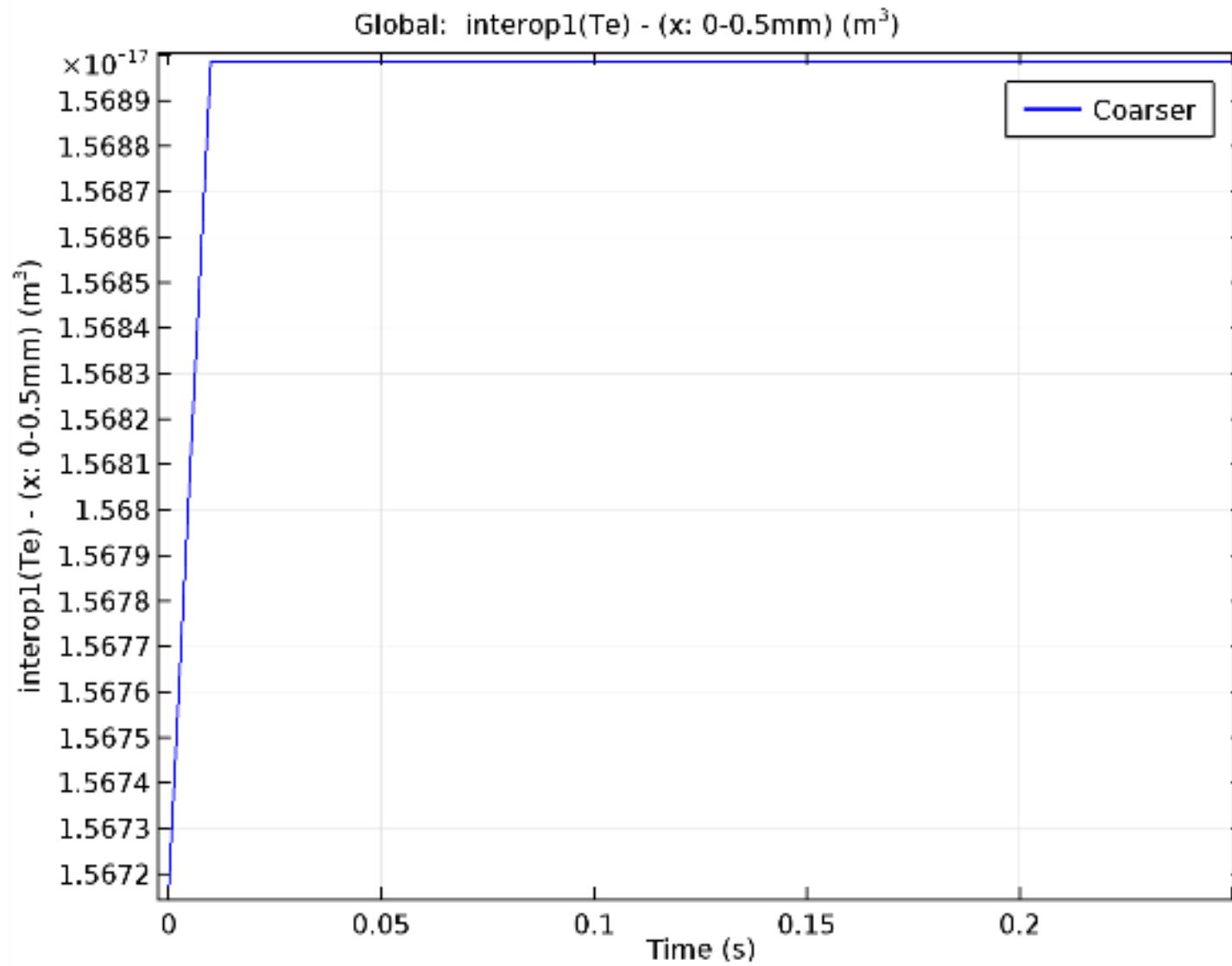


Figure 18 (b): Coarser Mesh

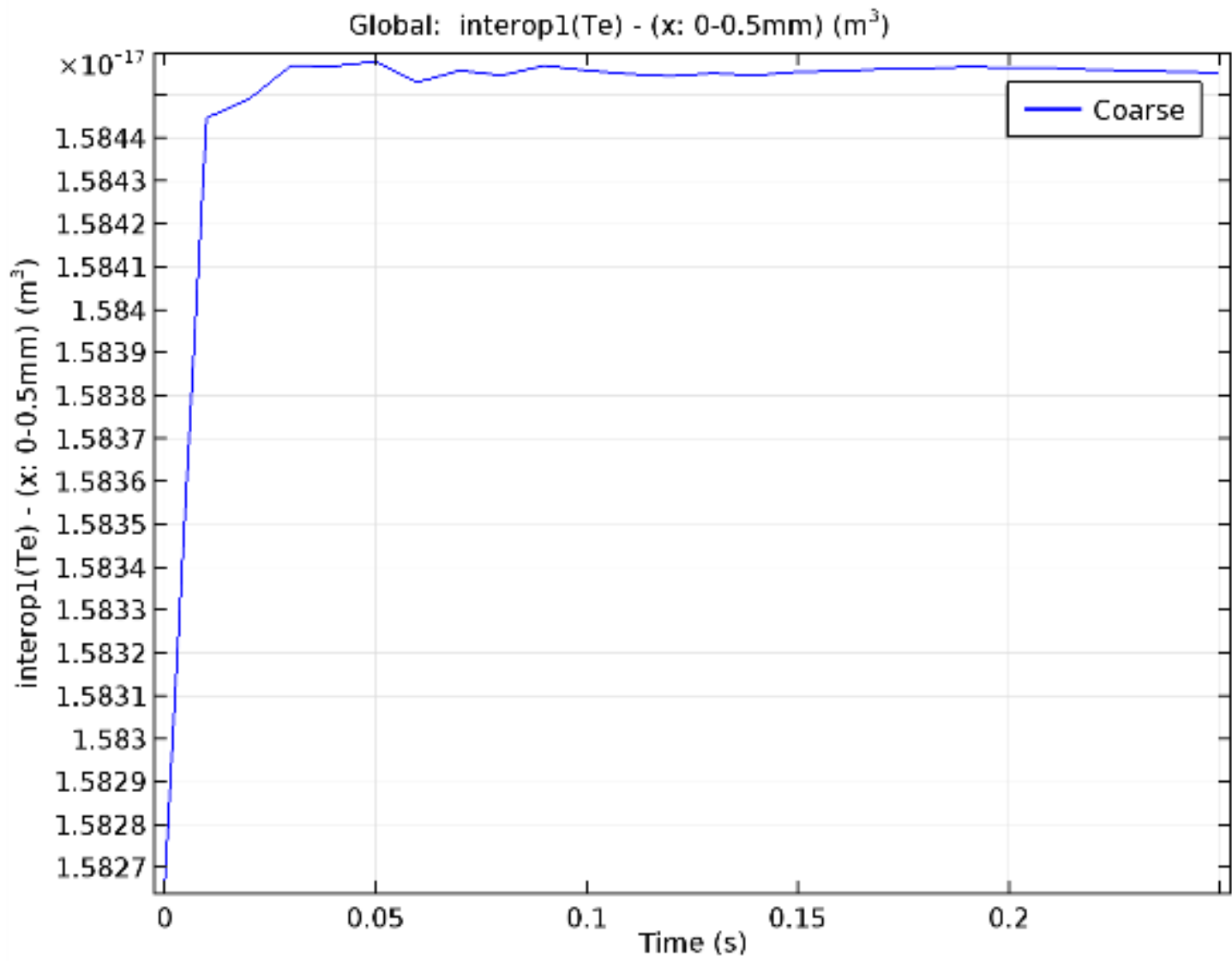


Figure 18 (c): Coarse Mesh

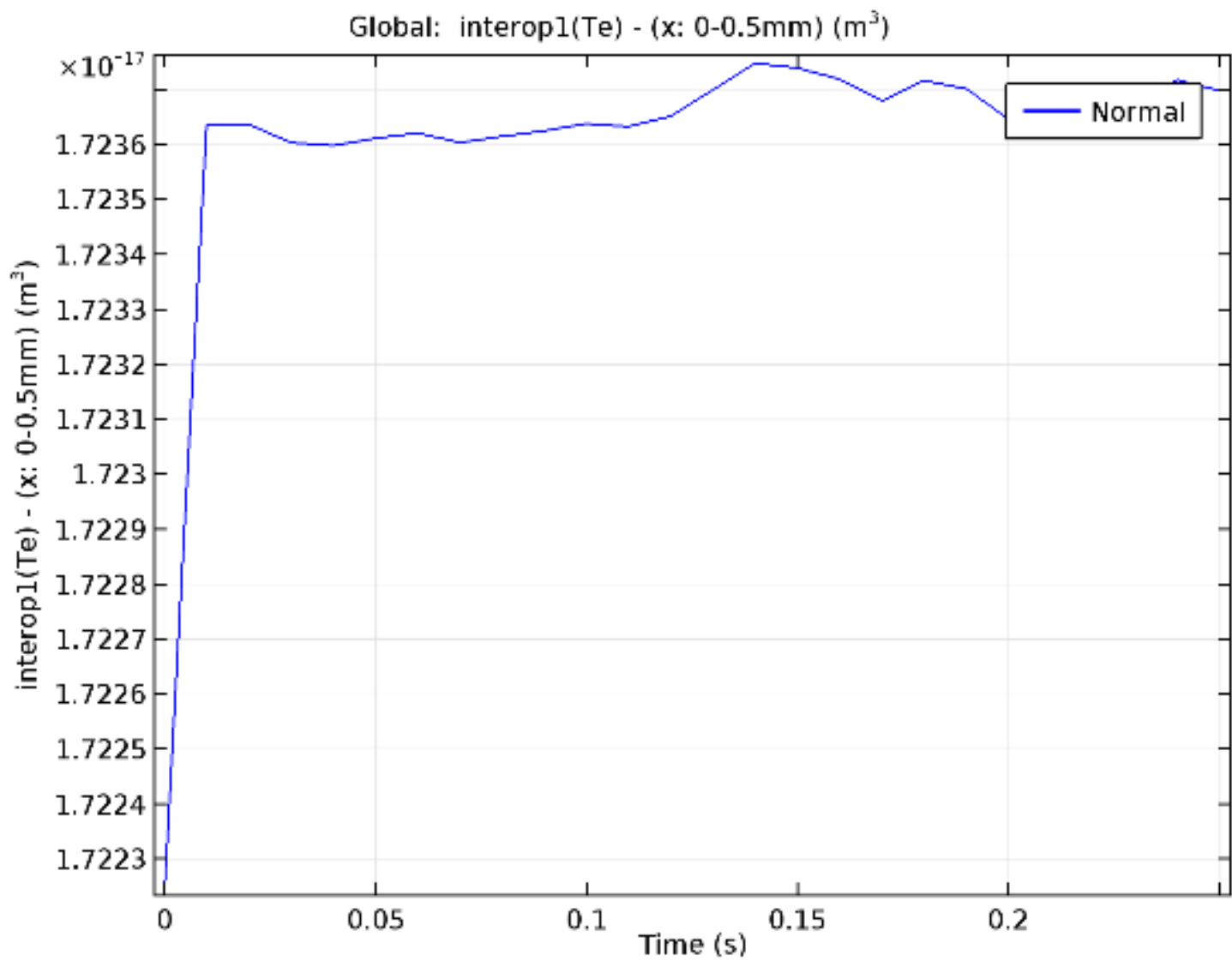


Figure 18 (d): Normal Mesh

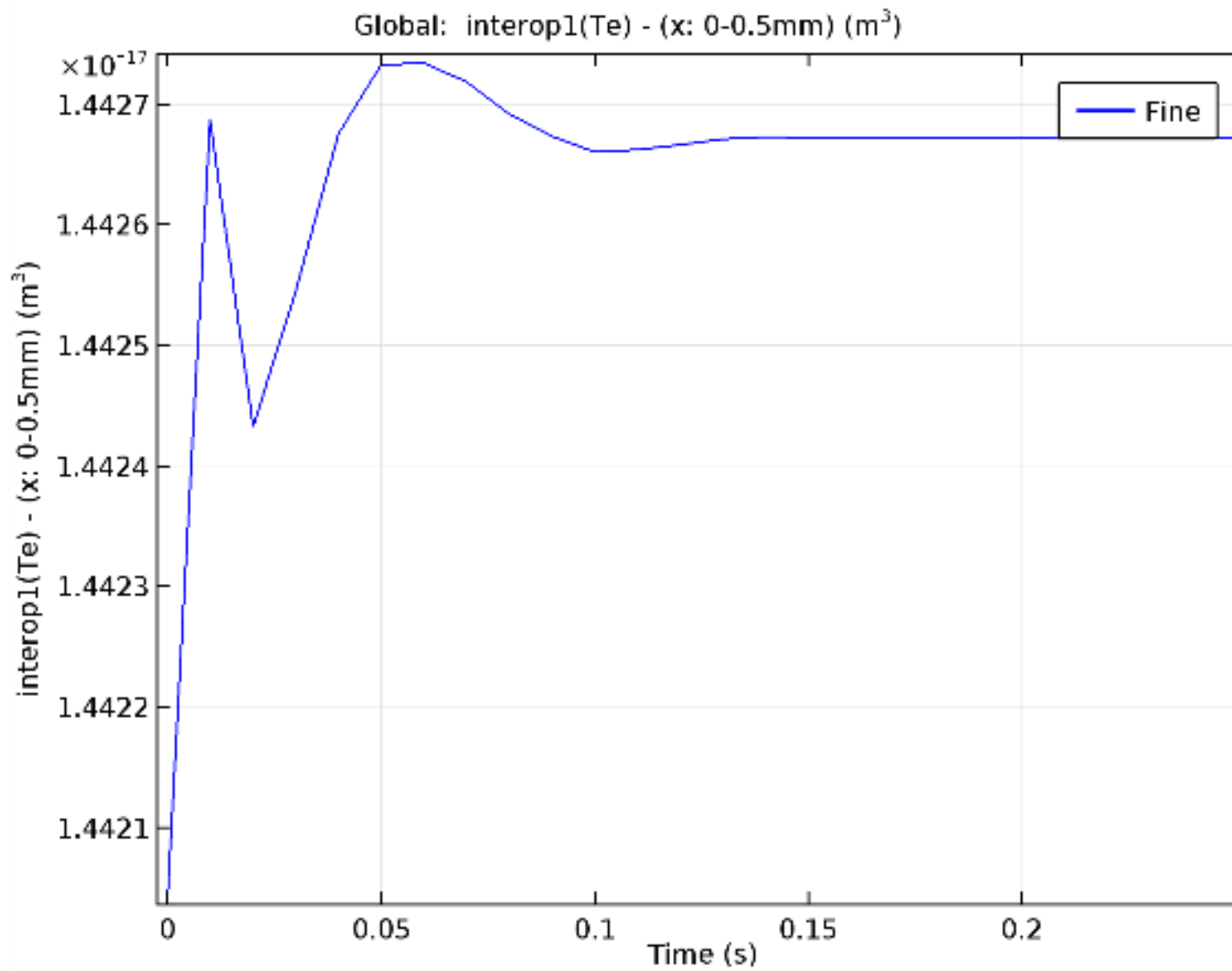
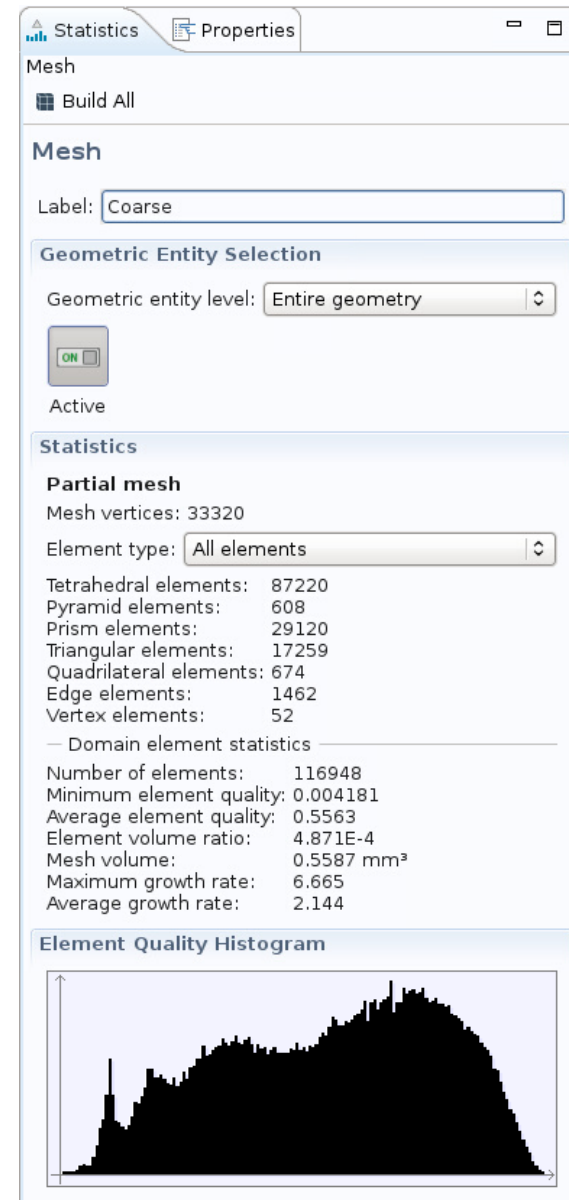
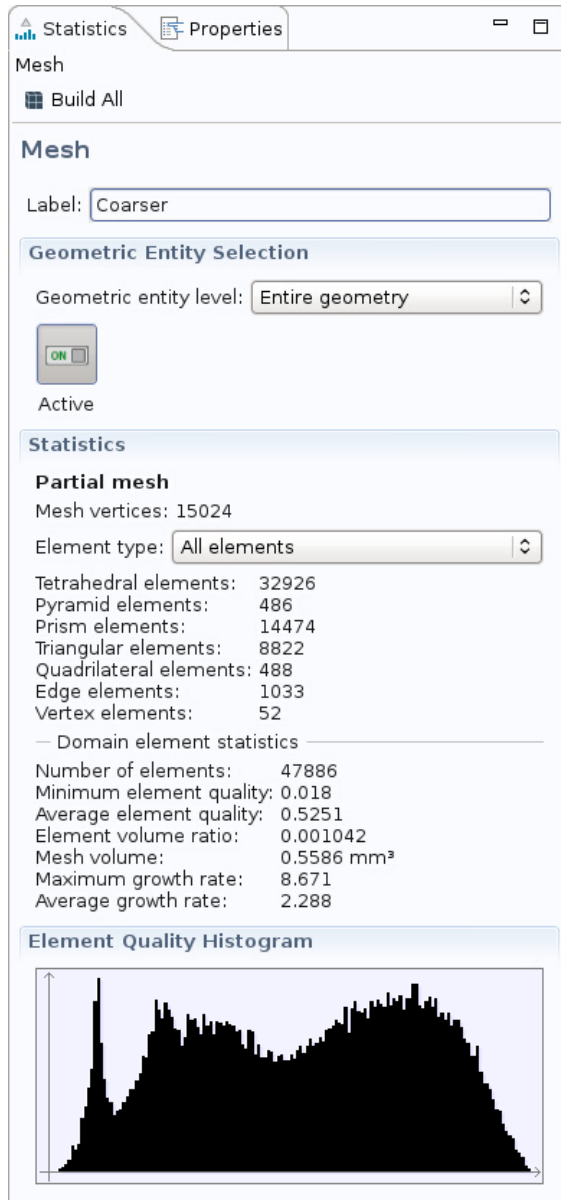


Figure 18 (e): Fine Mesh



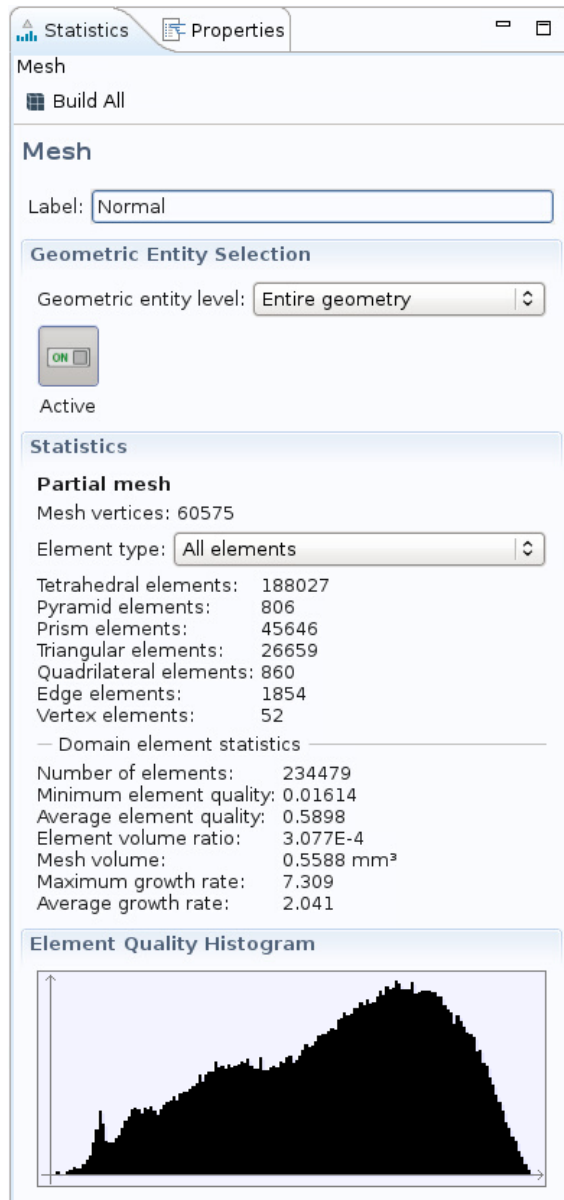


Figure 59: Normal Mesh Statistics

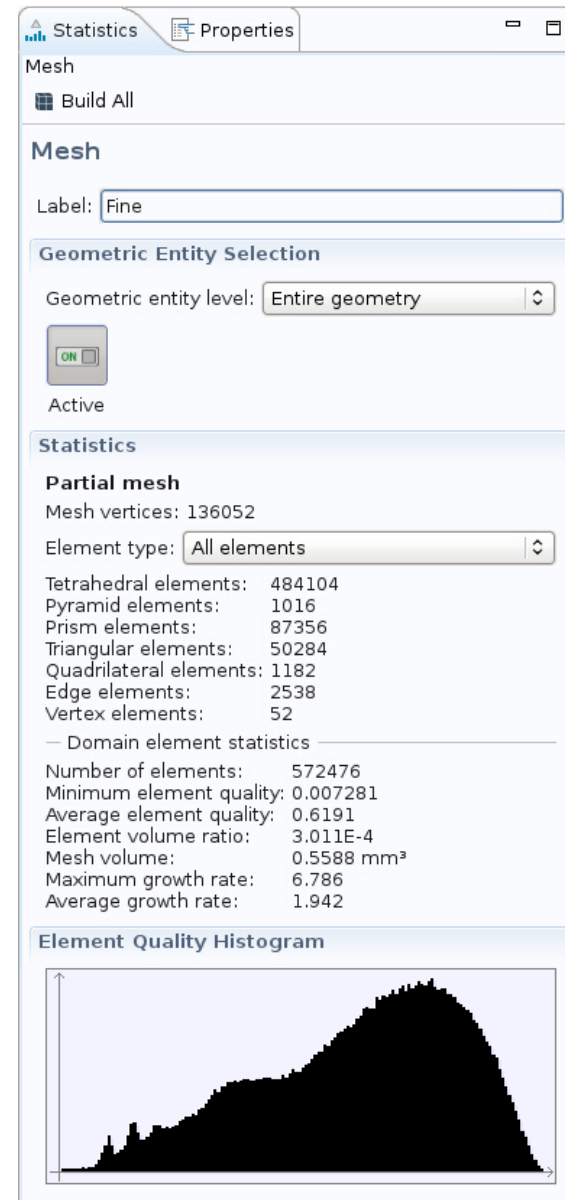


Figure 60: Fine Mesh Statistics

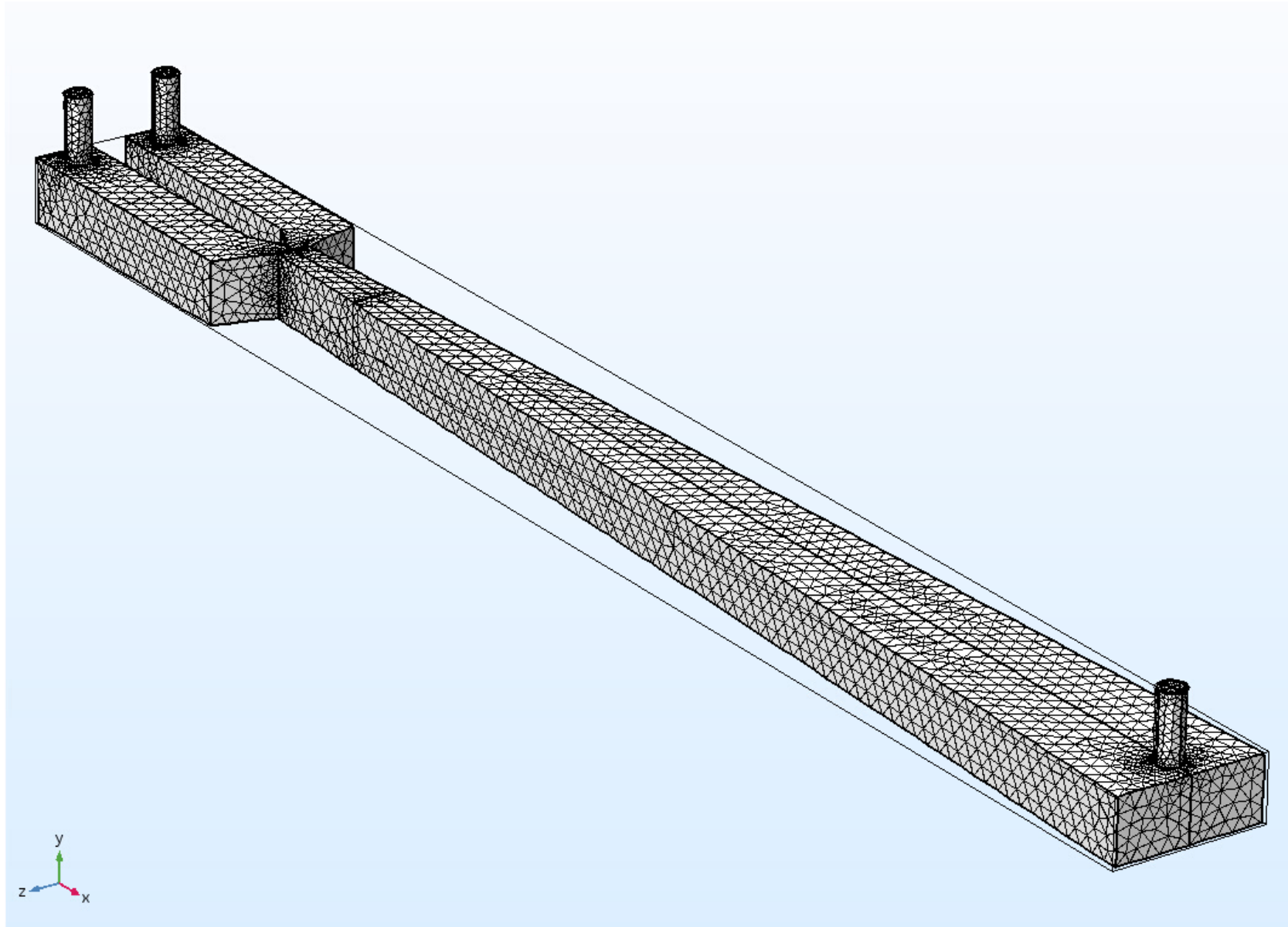


Figure 61: Coarser Mesh

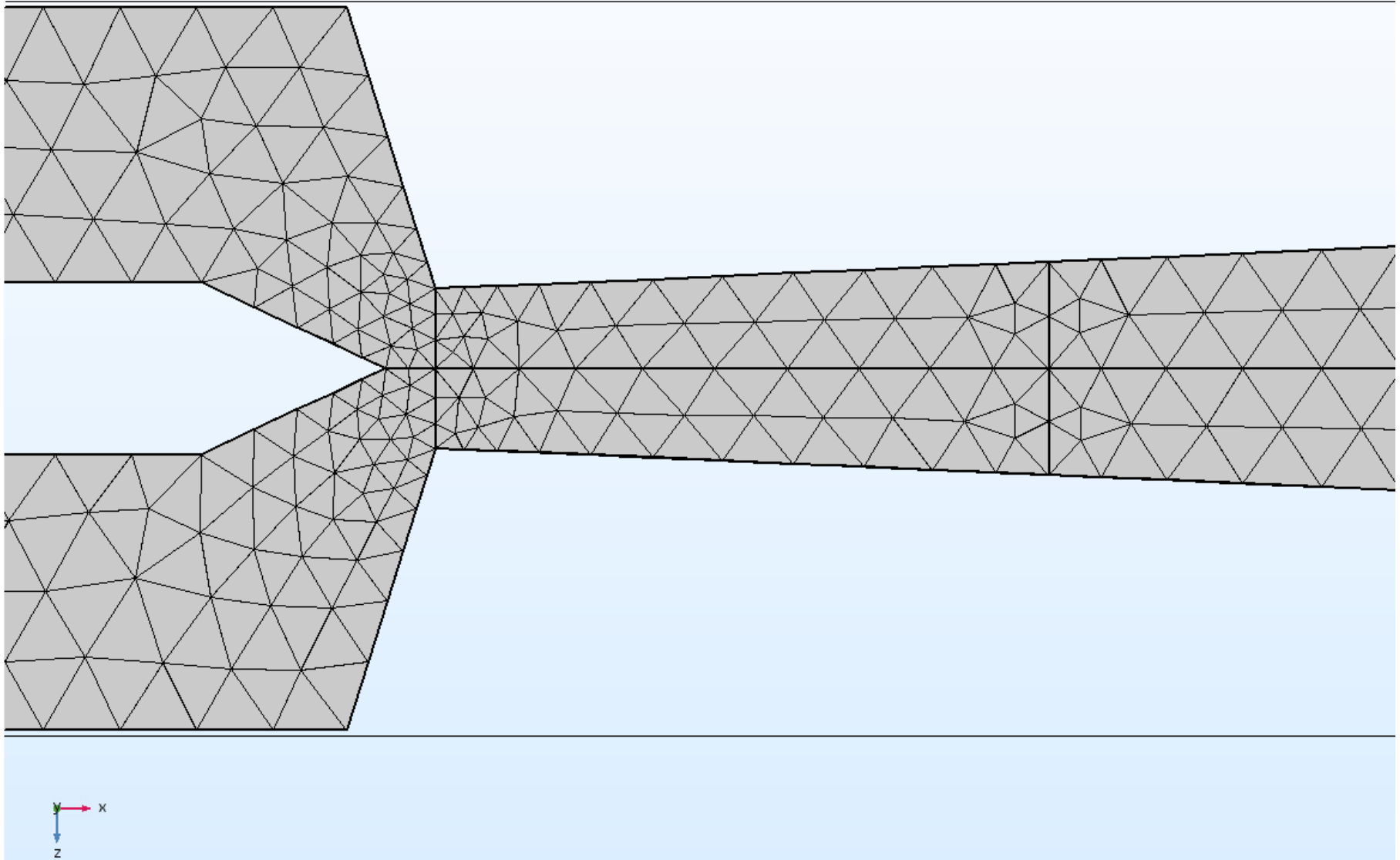


Figure 62: Coarser Mesh (in channel)

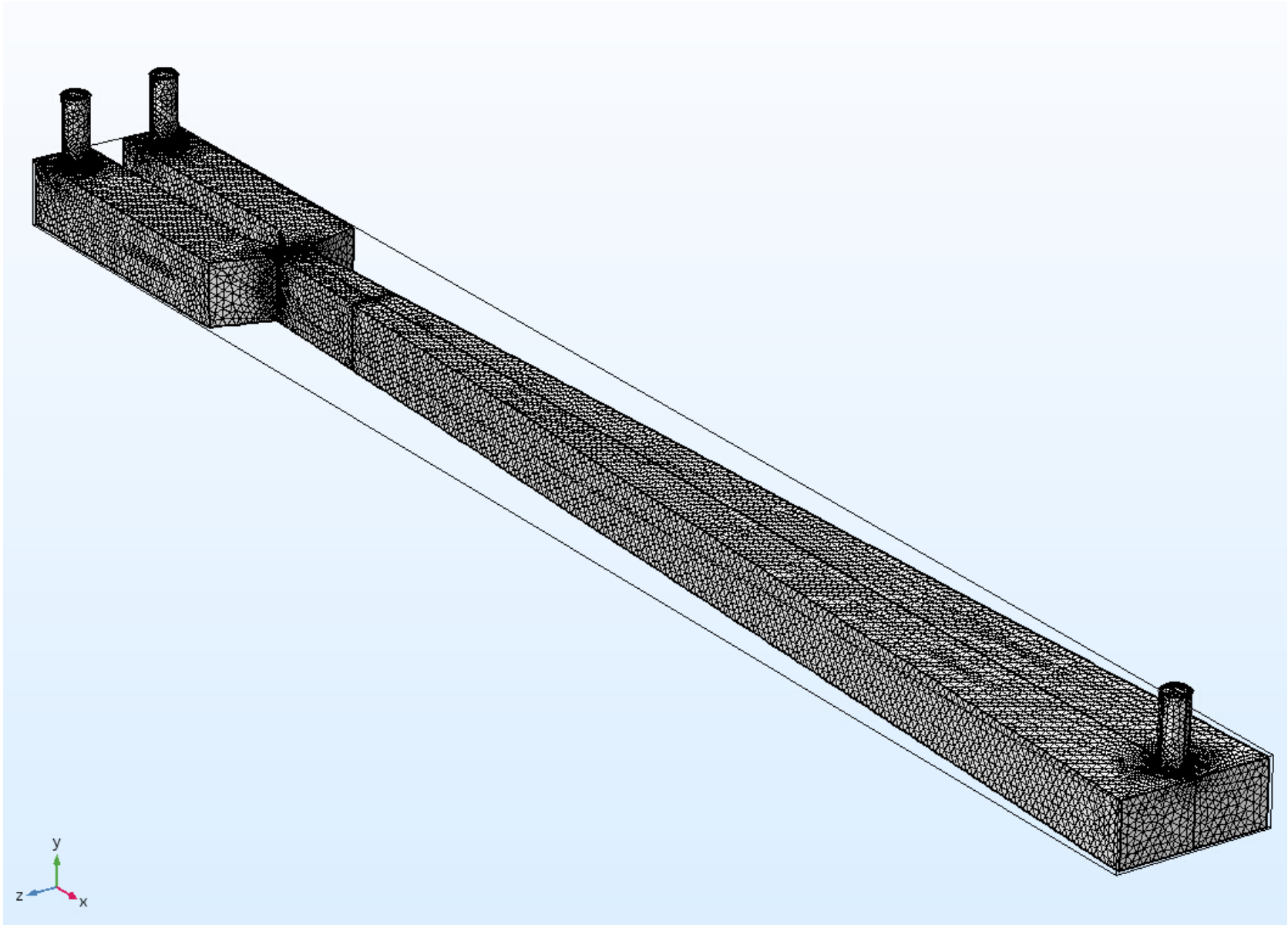


Figure 63: Normal Mesh

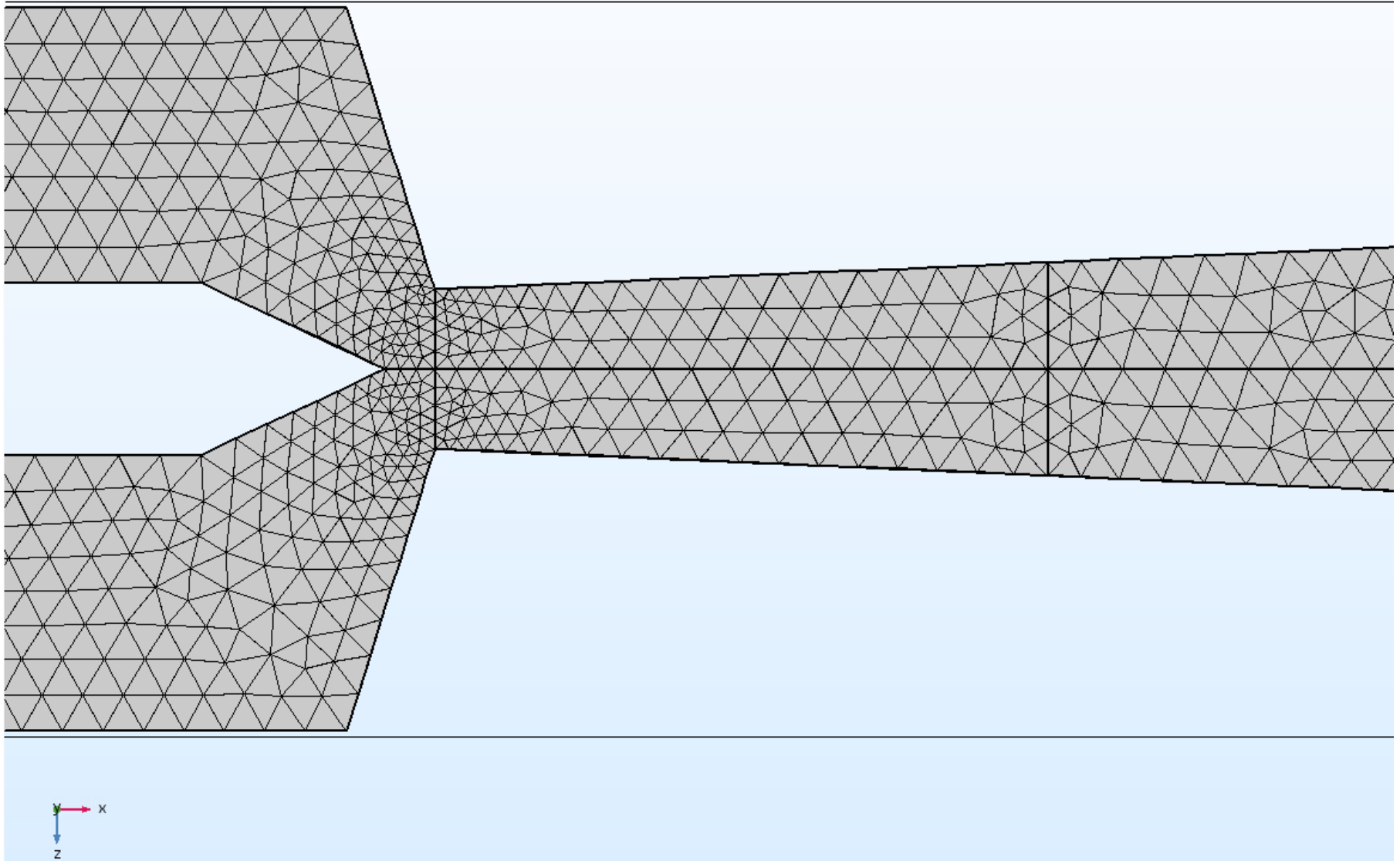


Figure 64: Normal Mesh (in channel)

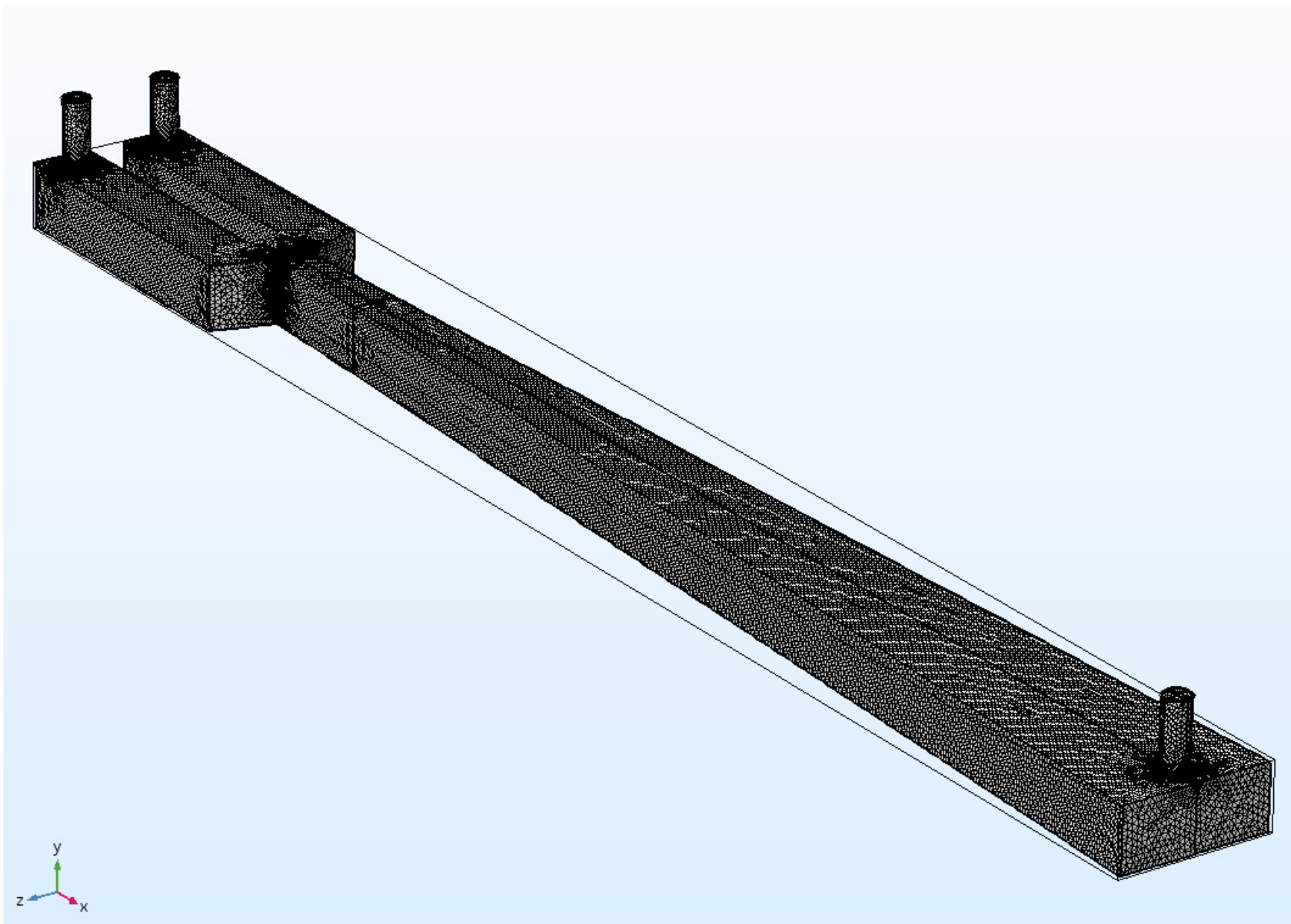


Figure 65: Fine Mesh

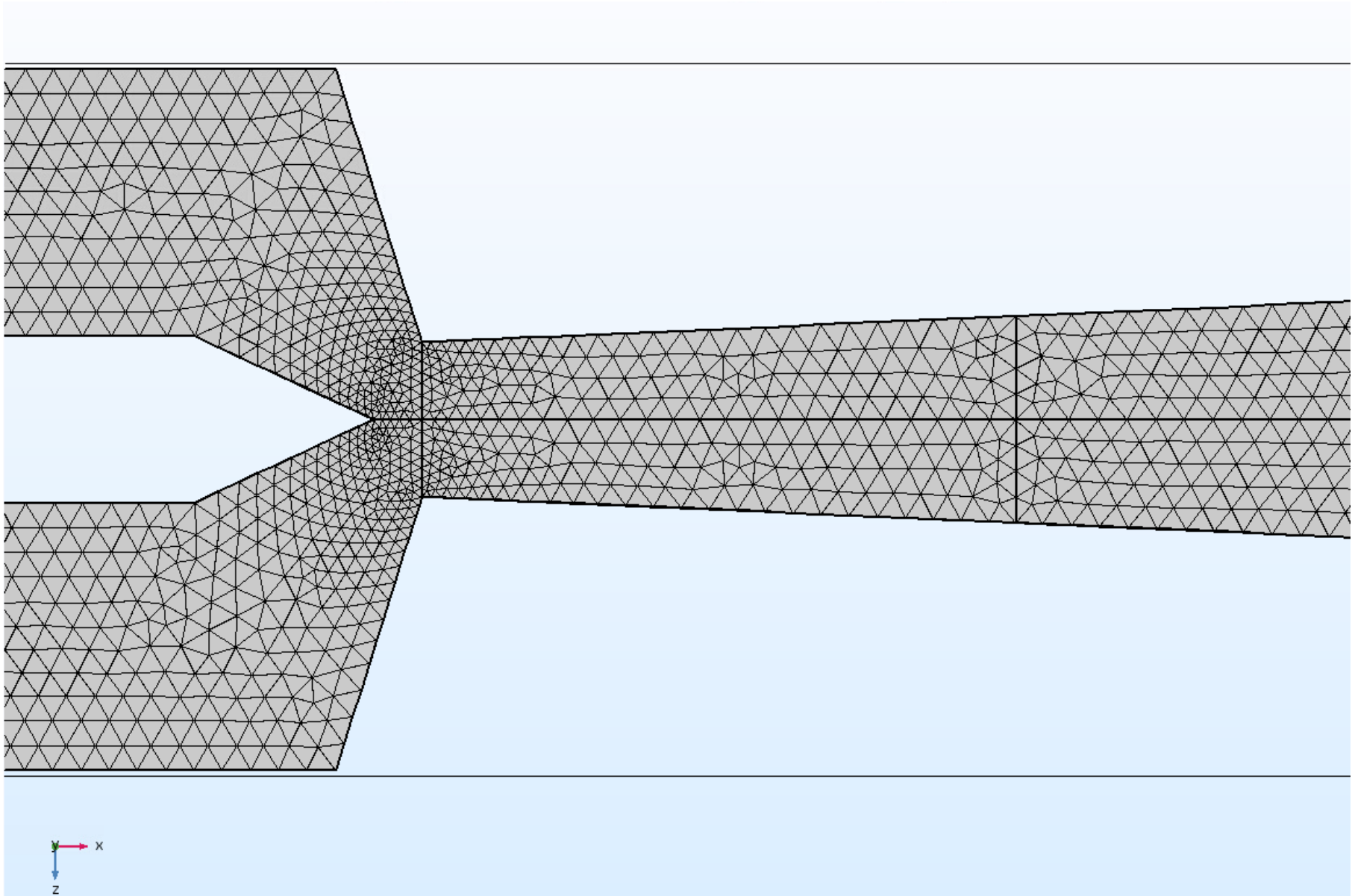


Figure 66: Fine Mesh (in channel)